

University of Windsor

Scholarship at UWindor

Electronic Theses and Dissertations

Theses, Dissertations, and Major Papers

2011

TWO CIRCULAR CYLINDERS IN TURBULENT CROSS FLOW

Bitamotameni

University of Windsor

Follow this and additional works at: <https://scholar.uwindsor.ca/etd>

Recommended Citation

Motameni, Bitamotameni, "TWO CIRCULAR CYLINDERS IN TURBULENT CROSS FLOW" (2011). *Electronic Theses and Dissertations*. 201.

<https://scholar.uwindsor.ca/etd/201>

This online database contains the full-text of PhD dissertations and Masters' theses of University of Windsor students from 1954 forward. These documents are made available for personal study and research purposes only, in accordance with the Canadian Copyright Act and the Creative Commons license—CC BY-NC-ND (Attribution, Non-Commercial, No Derivative Works). Under this license, works must always be attributed to the copyright holder (original author), cannot be used for any commercial purposes, and may not be altered. Any other use would require the permission of the copyright holder. Students may inquire about withdrawing their dissertation and/or thesis from this database. For additional inquiries, please contact the repository administrator via email (scholarship@uwindsor.ca) or by telephone at 519-253-3000ext. 3208.

TWO CIRCULAR CYLINDERS IN TURBULENT CROSS FLOW

by

Bitam Motameni

A Thesis
Submitted to the Faculty of Graduate Studies
through Mechanical, Automotive, and Materials Engineering
in Partial Fulfillment of the Requirements for
the Degree of Master of Applied Science at the
University of Windsor

Windsor, Ontario, Canada

2011

© 2011 Bitam Motameni

TWO CIRCULAR CYLINDERS IN TURBULENT CROSS FLOW

by

Bitam Motameni

APPROVED BY:

Dr. Rupp Carriveau, Outside Department Reader
Department of Civil and Environmental Engineering

Dr. Gary Rankin, Department Reader
Department of Mechanical, Automotive and Materials Engineering

Dr. David Ting, Advisor
Department of Mechanical, Automotive and Materials Engineering

Dr. Bruce Minaker, Chair of Defense
Department of Mechanical, Automotive and Materials Engineering

April 28, 2011

DECLARATION OF ORIGINALITY

I hereby certify that I am the sole author of this thesis and that no part of this thesis has been published or submitted for publication.

I certify that, to the best of my knowledge, my thesis does not infringe upon anyone's copyright nor violate any proprietary rights and that any ideas, techniques, quotations, or any other material from the work of other people included in my thesis, published or otherwise, are fully acknowledged in accordance with the standard referencing practices. Furthermore, to the extent that I have included copyrighted material that surpasses the bounds of fair dealing within the meaning of the Canada Copyright Act, I certify that I have obtained a written permission from the copyright owner(s) to include such material(s) in my thesis and have included copies of such copyright clearances to my appendix.

I declare that this is a true copy of my thesis, including any final revisions, as approved by my thesis committee and the Graduate Studies office, and that this thesis has not been submitted for a higher degree to any other University or Institution.

ABSTRACT

The effects of turbulence intensity ($Tu = 0.5\%$ to 10%), normalized integral length scale ($\Lambda/D = 0.56$ to 1.28 , where D is the diameter of the cylinder), and Reynolds number ($6.7 \times 10^3 \lesssim Re \lesssim 1.2 \times 10^4$) on the drag and lift force coefficients, C_D and C_L , of two staggered circular cylinders were experimentally investigated. The longitudinal and transverse spacing between the centres of two identical cylinders, L/D and T/D , were kept constant at 4 and 1, respectively.

At $Tu = 4\%$, increasing Λ/D dramatically changes C_D . However, the difference diminished when $Tu \gtrsim 7\%$. $\Lambda/D = 0.56$ has an insignificant effect on C_L . Increasing Re has a negligible effect on the force coefficients. When $\Lambda/D \lesssim 1$, with increasing Tu from 4% to 7% , the C_D increases and remains constant beyond 7% . When $\Lambda/D = 1.28$, with increasing Tu from 4% to 7% , the C_D decreases and remains constant beyond 7% .

DEDICATION

*To Ali,
who has been, is, and always will be the love of my life.*

ACKNOWLEDGEMENTS

I would like to express my sincere gratitude to Dr. D. S-K. Ting for his excellent guidance and support during this study. The invaluable comments and assistance from the committee members, Dr. G. Rankin and Dr. R. Carriveau, are gratefully acknowledged. Technical assistance from the staff of the University of Windsor is appreciated. Gratitude goes especially to Mr. A. Jenner and Mr. P. Seguin.

The financial support from the Natural Sciences and Engineering Research Council of Canada in the form of Research Assistantship and an Equipment Grant are gratefully acknowledged. The financial support from the Department of Mechanical, Automotive and Materials Engineering in the form of a Graduate Assistantship is acknowledged.

Last but not the least, I would like to express my sincere appreciation to my parents for their encouragement and unconditional support.

TABLE OF CONTENTS

DECLARATION OF ORIGINALITY	iii
ABSTRACT.....	iv
DEDICATION.....	v
ACKNOWLEDGEMENTS.....	vi
LIST OF FIGURES	ix
NOMENCLATURE	xvii
I. INTRODUCTION	
1.1. Objective	2
1.2. Scope of study	2
II. LITERATURE REVIEW	
2.1. Flow around a single circular cylinder	4
2.1.1. Smooth flow past a single circular cylinder.....	5
2.2. Turbulence flow past a single circular cylinder	9
2.3. Flow around two circular cylinders.....	11
2.3.1. Basic interference flow regimes	13
2.4. Turbulence flow past two circular cylinders	19
III. DESIGN AND METHODOLOGY	
3.1. Wind tunnel setup	23
3.2. Cylinder models.....	24
3.2.1. Drag and lift forces measurements.....	26
3.2.2. Pressure distribution measurements	29
3.3. Perforated plates	31
3.4. Hot-wire anemometer	32
3.4.1. Hot-wire calibration.....	34
3.5. Traversing mechanism	36
IV. DATA ANALYSIS	
4.1. Hot-wire data analysis	37
4.2. Decay of turbulence intensity downstream of the perforated plate	39
4.3. Integral length scale	39

v.	RESULT AND DISCUSSION	
	5.1. Circular cylinders in smooth flow	43
	5.2. Comprehensive view of the effect of the turbulence on two staggered cylinders.....	60
	5.3. Effect of integral length on two staggered cylinder	73
	5.4. Comments on the effect of Re on PSD.....	77
	5.5. Practical implications.....	79
vi.	CONCLUSIONS AND RECOMMENDATIONS	
	6.1. Conclusions	81
	6.2. Recommendations	83
	REFERENCES	85
	APPENDIX A: Surface roughness measurement	90
	APPENDIX B: Selecting sample size and sample rate in the load cell	92
	APPENDIX C: Selecting sample size and sample rate in the hot-wire	95
	APPENDIX D: Uncertainty analysis	97
	APPENDIX E: Force measurement results	110
	APPENDIX F: Effect of turbulence on velocity, turbulence intensity, and root mean square of velocity profiles	115
	APPENDIX G: Effect of Reynolds number on the pressure distributions around the upstream and downstream cylinders	120
	VITA AUCTORIS	125

LIST OF FIGURES

Fig. 1	Regions of disturbed flow around a circular cylinder, after Zdravkovich [2].....	5
Fig. 2	Flow pattern for a circular cylinder in laminar cross flow	8
Fig. 3	Turbulence intensity and Λ/D effects on $C_D - Re$ relationship	10
Fig. 4	Two circular cylinders arrangements in cross flow (a) in tandem, (b) side- by- side, and (c) staggered	11
Fig. 5	Shear layer and vortex formation for two staggered circular cylinders in cross flow, after Sumner [18]	12
Fig. 6	Wake and proximity interference boundaries for two identical staggered circular cylinders, based on Zdravkovich [20].....	13
Fig. 7	Static force coefficient map for a downstream cylinder in the subcritical Re , 4×10^4 $\lesssim Re \lesssim 2 \times 10^5$ (a) lift coefficient, and (b) drag coefficient, after Zdravkovich [20]	14
Fig. 8	Flow pattern around two staggered circular cylinders in cross flow (a) the interference of wake, (b) the interference of shear layer, and (c) the interference of neighbourhood, $Re = 2.2 \times 10^5$ and 3.3×10^5 , after Gu and Sun [21].....	15
Fig. 9	Flow patterns for two identical staggered circular cylinders in cross flow (a) closely spaced, (b) moderately spaced, and (c) widely spaced, $850 \leq Re \leq 1900$, based on Sumner et al. [22].....	16
Fig. 10	Variation of C_D with L/D for two staggered cylinders ($\alpha = 11^\circ$) at $Re = 4.2 \times 10^4$ in smooth and turbulence flow, after Liu [27]	20
Fig. 11	Variation of C_D with Re for the upstream cylinder of two staggered cylinders in turbulence flow, $1.7 \times 10^4 \lesssim Re \lesssim 8 \times 10^4$, after Price [29].	21

Fig. 12 Constant C_D and constant C_L lines for downstream cylinder at $Re = 6.5 \times 10^5$ and $Tu = 10\%$ (a) drag coefficient, and (b) lift coefficient, ● signifies the measurement points, after Gu et al. [30].	22
Fig. 13 An overall view of the closed-loop wind tunnel utilized in this study	23
Fig. 14 Two cylinders in cross flow (a) two cylinders in the wind tunnel looking upstream, (b) two staggered cylinders set-up, and (c) actual setup with dummy ends looking upstream	25
Fig. 15 Actual set-up of the load cell (a) load cell connection to the wind tunnel, (b) load cell connection to a 49 mm dummy end and cylinder	26
Fig. 16 Load cell calibration check set-up	27
Fig. 17 Force (N) versus mass (kg)	28
Fig. 18 Detail of the pressure measurement set-up (a) manometer connection to the cylinder outside the wind tunnel looking upstream, (b) pressure tab connection to the wind tunnel looking upstream, (c) azimuth angle (θ), and (d) pressure tubes inside the cylinders	30
Fig. 19 The orificed perforated plates	31
Fig. 20 Schematic of the perforated plates (a) $d = 25.1$ mm, (b) $d = 38.1$ mm, (c) $d = 50.8$ mm, and (d) cross section of the plate	32
Fig. 21 Experimental set-up in the wind tunnel	33
Fig. 22 Hot-wire calibration system (a) calibration unit, and (b) air supplier	35
Fig. 23 The light-duty 2D traversing mechanism	36
Fig. 24 Integral time scale for $d38.1$ plate at $50x/d$ and $U_0 = 8.2$ m/s	38

Fig. 25 Turbulence intensity downstream of: (a) d25.4 plate, (b) d38.1 plate, and (c) d50.4 plate.....	40
Fig. 26 Integral length scale downstream of: (a) d25.4 plate, (b) d38.1 plate, and (c) d50.4 plate.....	41
Fig. 27 Single cylinder in smooth flow (a) drag and lift coefficients, and (b) pressure distributions around a cylinder, ■ signifies force measurement, ■ denotes pressure measurement, error bars are based on the force measurement technique.....	45
Fig. 28 Stream-wise mean velocity, turbulent intensity, and root mean square of velocity profiles for a single cylinder in smooth flow (a) mean velocity, (b) turbulence intensity, and (c) root mean square of velocity.....	46
Fig. 29 Flow pattern and turbulence intensity profile for a single cylinder in smooth flow, “S” signifies the separation point, and “P” denotes the stagnation point	48
Fig. 30 PSD at different vertical locations across the wake of a single cylinder in smooth flow ($Tu \lesssim 0.5\%$) (a) $Re = 6700$, (b) $Re = 9200$, and (c) $Re = 12000$, the vertical scale is arbitrary, but the same scale is used for all spectra.....	49
Fig. 31 Drag and lift coefficients of two staggered cylinders in smooth flow (a) upstream cylinder, and (b) downstream cylinder, FM signifies the force measurement, PM denotes pressure measurement, error bars are based on the force measurement technique.....	52
Fig. 32 Force coefficient map for the downstream cylinder of two staggered cylinders in smooth flow in subcritical Re (a) drag coefficient, and (b) lift coefficient, ■ signifies the current study, after Zdravkovich [20].	52

Fig. 33 Pressure distribution of two staggered cylinders in smooth flow (a) around the upstream cylinder, and (b) around the downstream cylinder.....	55
Fig. 34 Stream-wise mean velocity, turbulent intensity, and root mean square of velocity profiles for two cylinders in smooth flow (a) mean velocity, (b) turbulence intensity, and (c) root mean square of velocity.....	56
Fig. 35 Flow pattern and turbulence intensity profile for two cylinders in smooth flow, “S” signifies the separation point, and “P” denotes the stagnation point.	58
Fig. 36 PSD at different vertical locations across the wake for two cylinders in smooth flow ($Tu \lesssim 0.5\%$) (a) $Re = 6700$, (b) $Re = 9200$, (c) $Re = 12000$, the vertical scale is arbitrary, but the same scale is used for all spectra.....	59
Fig. 37 Tu effects on the upstream cylinder (a) $Re = 6700$, (b) $Re = 9200$, and (c) $Re = 12000$, pressure measurement technique.	64
Fig. 38 Tu effects on the downstream cylinder (a) $Re = 6700$, (b) $Re = 9200$, and (c) $Re = 12000$, pressure measurement technique.	65
Fig. 39 Pressure distribution at $Re = 6700$ and $\Lambda/D = 0.56$ around (a) upstream cylinder, and (b) downstream cylinder.	66
Fig. 40 Pressure distribution at $Re = 6700$ and $\Lambda/D = 1.28$ around (a) upstream cylinder, and (b) downstream cylinder.	66
Fig. 41 Stream-wise mean velocity, turbulent intensity, and root mean square of velocity profiles at $Re = 6700$ and $\Lambda/D = 0.56$ (a) mean velocity, (b) turbulence intensity, and (c) root mean square of velocity.....	67
Fig. 42 Flow pattern and turbulence intensity profile for two cylinders in turbulence flow, “S” signifies the separation point, and “P” denotes the stagnation point.	70

Fig. 43 PSD at different vertical locations across the wake th $Re = 6700$, and $\Lambda/D = 0.56$ (a) smooth flow, (b) $Tu = 4\%$, (c) $Tu = 7\%$, (d) $Tu = 10\%$, the vertical scale is arbitrary, but the same scale is used for all spectra.....	72
Fig. 44 Λ/D effects on the upstream cylinder (a) $Tu = 4\%$, (b) $Tu = 7\%$, and (c) $Tu =$ 10% , pressure measurement technique.	75
Fig. 45 Λ/D effects on the downstream cylinder (a) $Tu = 4\%$, (b) $Tu = 7\%$, and (c) $Tu =$ 10% , pressure measurement technique.	76
Fig. 46 PSD at different vertical locations across the wake at $Tu = 4\%$ and $\Lambda/D = 0.56$: (a) $Re = 6700$, (b) $Re = 9200$, and (c) $Re = 12000$. The vertical scale is arbitrary, but the same scale is used for all spectra.	78
Fig. 47 The roughness of the cylinder: (a) first location, and (b) second location	91
Fig. 48 Sample rate check for the load cells reading (a) C_D , and (b) C_L versus the sample rate, 25.4 mm cylinder, $Tu = 4\%$, $U_o = 4.5$ m/s.....	93
Fig. 49 Sample size check for load cell reading: (a) C_D , and (b) C_L versus sample size at sample rate 2 kHz, 25.4 mm cylinder, $Tu = 7\%$, $U_o = 6.2$ m/s.....	94
Fig. 50 Sample size check for d38.1 plate located at $10 x/d$ and $U_o = 4.3$ m/s (a) U_{mean} , (b) U_{rms} , (c) $Tu\%$, and (d) integral length scale.	96
Fig. 51 Tu effects on the upstream cylinder (a) $Re = 6700$, (b) $Re = 9200$, and (c) $Re =$ 12000 , force measurement technique.	111
Fig. 52 Tu effects on the downstream cylinder (a) $Re = 6700$, (b) $Re = 9200$, and (c) $Re =$ 12000 , force measurement technique.	112
Fig. 53 Λ/D effects on the upstream cylinder (a) $Tu = 4\%$, (b) $Tu = 7\%$, and (c) $Tu =$ 10% , force measurement technique.	113

Fig. 54 Λ/D effects on the upstream cylinder (a) $Tu = 4\%$, (b) $Tu = 7\%$, and (c) $Tu = 10\%$, force measurement technique.....	114
Fig. 55 Stream-wise mean velocity, turbulent intensity, and root mean square of velocity profiles at $Re = 6700$ and $\Lambda/D = 0.56$ (a) mean velocity, (b) turbulence intensity, and (c) root mean square of velocity.....	115
Fig. 56 Stream-wise mean velocity, turbulent intensity, and root mean square of velocity profiles at $Re = 6700$ and $\Lambda/D = 0.96$ (a) mean velocity, (b) turbulence intensity, and (c) root mean square of velocity.....	116
Fig. 57 Stream-wise mean velocity, turbulent intensity, and root mean square of velocity profiles at $Re = 6700$ and $\Lambda/D = 1.28$ (a) mean velocity, (b) turbulence intensity, and (c) root mean square of velocity.....	116
Fig. 58 Stream-wise mean velocity, turbulent intensity, and root mean square of velocity profiles at $Re = 9200$ and $\Lambda/D = 0.56$ (a) mean velocity, (b) turbulence intensity, and (c) root mean square of velocity.....	117
Fig. 59 Stream-wise mean velocity, turbulent intensity, and root mean square of velocity profiles at $Re = 9200$ and $\Lambda/D = 0.96$ (a) mean velocity, (b) turbulence intensity, and (c) root mean square of velocity.....	117
Fig. 60 Stream-wise mean velocity, turbulent intensity, and root mean square of velocity profiles at $Re = 9200$ and $\Lambda/D = 1.28$ (a) mean velocity, (b) turbulence intensity, and (c) root mean square of velocity.....	118
Fig. 61 Stream-wise mean velocity, turbulence intensity, and root mean square of velocity profiles at $Re = 12000$ and $\Lambda/D = 0.56$ (a) mean velocity, (b) turbulence intensity, and (c) root mean square of velocity.....	118

Fig. 62 Stream-wise mean velocity, turbulent intensity, and root mean square of velocity profiles at $Re = 12000$ and $\Lambda/D = 0.96$ (a) mean velocity, (b) turbulence intensity, and (c) root mean square of velocity.....	119
Fig. 63 Stream-wise mean velocity, turbulent intensity, and root mean square of velocity profiles at $Re = 12000$ and $\Lambda/D = 1.28$ (a) mean velocity, (b) turbulence intensity, and (c) root mean square of velocity.....	119
Fig. 64 Pressure distribution at $Tu = 4\%$, and $\Lambda/D = 0.56$ around (a) upstream cylinder, and (b) downstream cylinder.	120
Fig. 65 Pressure distribution at $Tu = 7\%$, and $\Lambda/D = 0.56$ around (a) upstream cylinder, and (b) downstream cylinder.	120
Fig. 66 Pressure distribution at $Tu = 10\%$, and $\Lambda/D = 0.56$ around (a) upstream cylinder, and (b) downstream cylinder.	121
Fig. 67 Pressure distribution at $Tu = 4\%$, and $\Lambda/D = 0.96$ around: (a) upstream cylinder, and (b) downstream cylinder.	121
Fig. 68 Pressure distribution at $Tu = 7\%$, and $\Lambda/D = 0.96$ around (a) upstream cylinder, and (b) downstream cylinder.	122
Fig. 69 Pressure distribution at $Tu = 10\%$, and $\Lambda/D = 0.96$ around (a) upstream cylinder, and (b) downstream cylinder.	122
Fig. 70 Pressure distribution at $Tu = 4\%$, and $\Lambda/D = 1.28$ around (a) upstream cylinder, and (b) downstream cylinder.	123
Fig. 71 Pressure distribution at $Tu = 7\%$, and $\Lambda/D = 1.28$ around (a) upstream cylinder, and (b) downstream cylinder.	123

Fig. 72 Pressure distribution at $Tu = 10\%$, and $\Lambda/D = 1.28$ around (a) upstream cylinder,
and (b) downstream cylinder. 124

NOMENCLATURE

A	Cylinder frontal area, $A = l \times D$ (m^2)
AR	Aspect ratio, l/D
C_0, C_1, C_2, C_3, C_4	Hot-wire calibration coefficients
C_D	Drag coefficient
C_L	Lift coefficient
C_P	Pressure coefficient
D	Cylinder diameter (mm)
d	Perforated plate holes diameter (mm)
E	Voltage of the probe (mV)
F_D	Drag force (N)
F_L	Lift force (N)
f	Vortex shedding frequency (Hz)
$f(\tau)$	Auto-correlation function of time
L	Longitudinal spacing between the centres of two cylinders (mm)
l	Cylinder length (mm)
m	Values varies from 0 to N-1
N	Sample size
n	Number of pressure taps
P	Gap between two cylinders (mm)
$P(\theta)$	Pressure on the surface of cylinder (Pa)
P_∞	Static pressure (Pa)

Re	Reynolds number, $Re = \frac{\rho U_0 D}{\mu}$
r	Static pressure port diameter (mm)
St	Strouhal number, $St = fD/U_0$
T	Transverse spacing between the centres of two cylinders (mm)
Tu	Turbulence intensity $\frac{u_{rms}}{\bar{U}}$ (%)
t	Time (s)
U	Local velocity (m/s)
U_0	Free-stream velocity (m/s)
\bar{U}	Time-averaged local velocity (m/s)
U_i	Instantaneous velocity (m/s)
U_{eff}	Effective velocity (m/s)
u	Instantaneous fluctuating velocity (m/s)
u_{rms}	Root mean square of velocity (m/s)
X	Streamwise spacing between the Hot-wire and the centre of the downstream cylinder (mm)
x	Wind tunnel stream-wise direction
y	Wind tunnel transverse direction
z	Wind tunnel longitudinal direction

Greek Symbols

α	Angle between the centre connection line of the cylinders and the wind direction
θ	Azimuth angle measured from wind direction
Λ	Integral length scale (mm)
μ	Dynamic viscosity ($\frac{\text{kg}}{\text{m}\cdot\text{s}}$)
ρ	Air density ($\frac{\text{kg}}{\text{m}^3}$)
τ_Λ	Integral time scale (s)

CHAPTER I

INTRODUCTION

Cylindrical structures in turbulence flows are far more common than laminar flows, both in nature and in engineering applications. Cylindrical bodies can be found both alone and in a group such as tube banks in heat exchangers, cooling systems for nuclear reactors, tall buildings, chimneys, power transmission lines, and pipe rack structures in petrochemical facilities. The periodic vortex shedding from these structures can lead to vibrations. When the vibration frequency approaches the natural frequency of the cylinder and its supporting system, resonance may occur, which can often lead to structural failure.

A pair of cylinders can be chosen as the simplest case of a group of structures. When two circular cylinders are subjected to a steady flow, the resulting forces and flow pattern in the wake may be very different from those found on a single cylinder at the same Reynolds number. A thorough understanding of characteristics of forces and flow pattern in the wake of such a simple case may be crucial to understand the characteristics of forces and flow pattern in the wake of more complex and larger-scale structures.

Since most practical applications occurring in different degrees of turbulence, it is imperative to have a proper knowledge of the free-stream turbulence effects on circular cylinders. To evaluate the effects of turbulence, at least two parameters should be used to characterize the turbulence, defined as: turbulence intensity, Tu , which represents the level of velocity fluctuation and turbulence length scale, Λ , which is a measure of the size of energy-containing eddies. The length scale is usually evaluated with a relative ratio to the cylinder diameter, Λ/D (normalized integral length scale).

1.1. Objective

This thesis describes a study at the University of Windsor having an ultimate goal of elucidating the effect of free-stream turbulence on the aerodynamic forces of two staggered circular cylinders of equal diameters in cross flow. The wake and force measurement results provide a detailed understanding of the unsteady flow, including Strouhal number, at the wake of the downstream cylinder in different flow regimes. Ting et al. [1] first conducted wind tunnel tests on two staggered circular cylinders of equal diameter subjected to laminar air cross flow. One of the cylinders was forced to oscillate transversely to the flow direction, while the other cylinder was stationary. The current study extends that work by including effects of flow turbulence on two stationary circular cylinders.

The aim of this study is to examine the independent effects of Reynolds number, turbulence intensity, Tu , and normalized integral length scale, Λ/D , on the force coefficients (C_D and C_L) of the upstream and downstream cylinders in cross flow. Also, the influence of turbulence intensity, Tu , and normalized integral length scale, Λ/D , on the wake structure of the downstream cylinder and Strouhal number is explained.

1.2. Scope of study

Within the limitations of our experimental facility, the Reynolds number based on free-stream velocity and cylinder diameter was varied from 6700 to 12000. Pairs of aluminum circular cylinders of equal diameters ($D = 22.2, 25.4, \text{ and } 38.1\text{mm}$) were used. Three aluminum orificed perforated plates ($d = 25.4, 38.1, \text{ and } 50.8 \text{ mm}$) were employed to generate a quasi-isotropic turbulent flow. The turbulence intensity, Tu , generated by

the empty wind tunnel and the available orificed perforated plates was fixed at 0.5%, 4%, 7%, and 10%. The relative integral length scale, Λ/D , was varied from 0.56 to 1.28.

The underlying mechanisms governing the drag and lift forces are explored with the help of the pressure and dynamic force measurement results on two staggered circular cylinders of equal diameter. The lift and drag coefficients, C_D and C_L , were deduced from pressure distributions around the cylinder. The pressure distribution around the cylinders, and pressure coefficient, C_p , of the upstream and downstream cylinders were measured by using a Dwyer series 475 mark III manometer connected to a pressure tap via 6.3 mm aluminum tubing. Also, the dynamic drag and lift coefficients, C_D and C_L , of the upstream and downstream cylinders were measured by using two ATI Gamma type load cells supporting upstream or downstream cylinder. To better understand the mechanism the wake structure of the downstream cylinder was surveyed using a single normal hot-wire of DISA type 55P11.

CHAPTER II

LITERATURE REVIEW

In this section, to better understand the fluid behaviour around two circular cylinders, the fluid behaviour around a single circular cylinder is discussed first. Then, the effect of turbulence flow on a single cylinder is reviewed, followed by a review of two circular cylinders in smooth and turbulence flows.

2.1. Flow around a single circular cylinder

When a flow passes a circular cylinder, a region of disturbed flow is formed around the cylinder. As shown in Fig. 1, Zdravkovich [2] classified the disturbed flow field around a circular cylinder into four regions:

- (i) The narrow retarded flow region. In which the local time-averaged velocity is less than the free-stream velocity.
- (ii) Two boundary layers attached to the surface of the cylinder. These boundary layers around the cylinder develop under the influence of a favourable pressure gradient followed by a small region of adverse pressure gradient just before separation.
- (iii) Two sidewise regions of displaced and accelerated flow. The expansion of displaced regions is strongly depending on the blockage effect.
- (iv) One wide downstream region of separated flow called the wake. The form of the wake is affected by the state of the flow which may be laminar or turbulent.

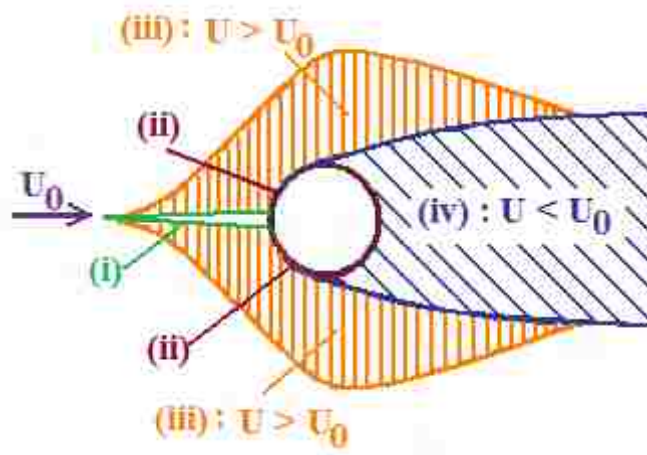


Fig. 1 Regions of disturbed flow around a circular cylinder, after Zdravkovich [2]

2.1.1. Smooth flow past a single circular cylinder

The flow past a circular cylinder displays a series of flow regions when going from small to large Reynolds numbers. The Reynolds number is defined using the free-stream velocity, U_0 , and the cylinder diameter, D ,

$$Re = \frac{\rho U_0 D}{\mu} \quad (1)$$

where ρ is the density and μ is the dynamic viscosity of the air. The wake behind a circular cylinder is shown in Fig. 2 for different values of Re [2, 3].

2.1.1.1. Creeping flow ($Re \lesssim 5$)

For $Re \lesssim 5$, streamlines do not detach from the cylinder surface, so the fluid follows the cylinder contours with no visible wake in this non-separated regime.

2.1.1.2. Steady, closed near-wake regime ($5 \lesssim Re \lesssim 45$)

For $5 \lesssim Re \lesssim 45$, the flow separates from the back of the cylinder and the closed near wake is characterized by a steady and symmetric pair of vortices. Coutanceau

and Bouard [4] investigated the un-detached vortices pattern behind a circular cylinder for $5 < Re < 40$. The experiments showed that the length of the wake, enclosing the two vortices, increases linearly with increasing Re .

2.1.1.3. Laminar vortex street ($45 \lesssim Re \lesssim 190$)

When $Re \gtrsim 45$, the separated region elongates in the stream-wise direction and when the “bubble length” is about two diameters [5], the wake becomes unstable and it starts to “wobble” in a sinusoidal manner. A laminar periodic wake is given by two staggered vortices of opposite sign. Huerre and Monkewits [6] showed that when Re exceeds 45 the wake becomes unstable and the vortices shed alternately from the cylinder sides. Bloor [7] found that over the $50 \lesssim Re \lesssim 200$ range, with increasing Re , disturbances in the vicinity of the vortex formation region appear.

2.1.1.4. Transition in shear layer ($190 \lesssim Re \lesssim 3 \times 10^5$)

Roshko [8] observed that at a Reynolds number of approximately 180, the two dimensional periodic Strouhal vortex wake undergoes a transition to three-dimensionality and the laminar periodic wake becomes unstable. Karniadakis and Triantafyllou [9] confirmed that at Reynolds number of approximately 200 the wake becomes three-dimensional, as a result of a secondary instability of the two-dimensional vortex street. In the range of $300 \lesssim Re \lesssim 1.5 \times 10^5$ (subcritical) the vortex shedding is strong and periodic.

2.1.1.5. Critical regime ($3 \times 10^5 \lesssim Re \lesssim 3 \times 10^6$)

In the critical regime $3 \times 10^5 \lesssim Re \lesssim 3 \times 10^6$, the cylinder boundary layer becomes turbulent and the wake is narrow and disorganized. Bearman [10] observed a narrow band of vortex shedding of a circular cylinder by using a hot-wire probe in the wake region for $10^5 \lesssim Re \lesssim 7.5 \times 10^5$. According to this study, in the $2 \times 10^5 \lesssim Re \lesssim 4 \times 10^5$ range, as Re increases, the mean drag coefficient drops from 1.14 to 0.23, due to the transition from laminar to turbulent separation of the boundary layer.

2.1.1.6. Postcritical (transcritical) regime ($Re \gtrsim 3 \times 10^6$)

In the postcritical Reynolds number range ($Re \gtrsim 3 \times 10^6$), regular vortex shedding is re-established with a turbulent cylinder boundary layer. In this regime, the turbulent flow separation point moves forward the rear of the cylinder. Roshko [11] conducted an experimental investigation of a single cylinder for $10^6 \lesssim Re \lesssim 10^7$ in a pressurized wind tunnel. He found that a definite vortex shedding occur at Re more than 3.5×10^6 . Also, it was determined that turbulent boundary layers endured more pressure rises causing a shift in the separation to the rear of the cylinder.

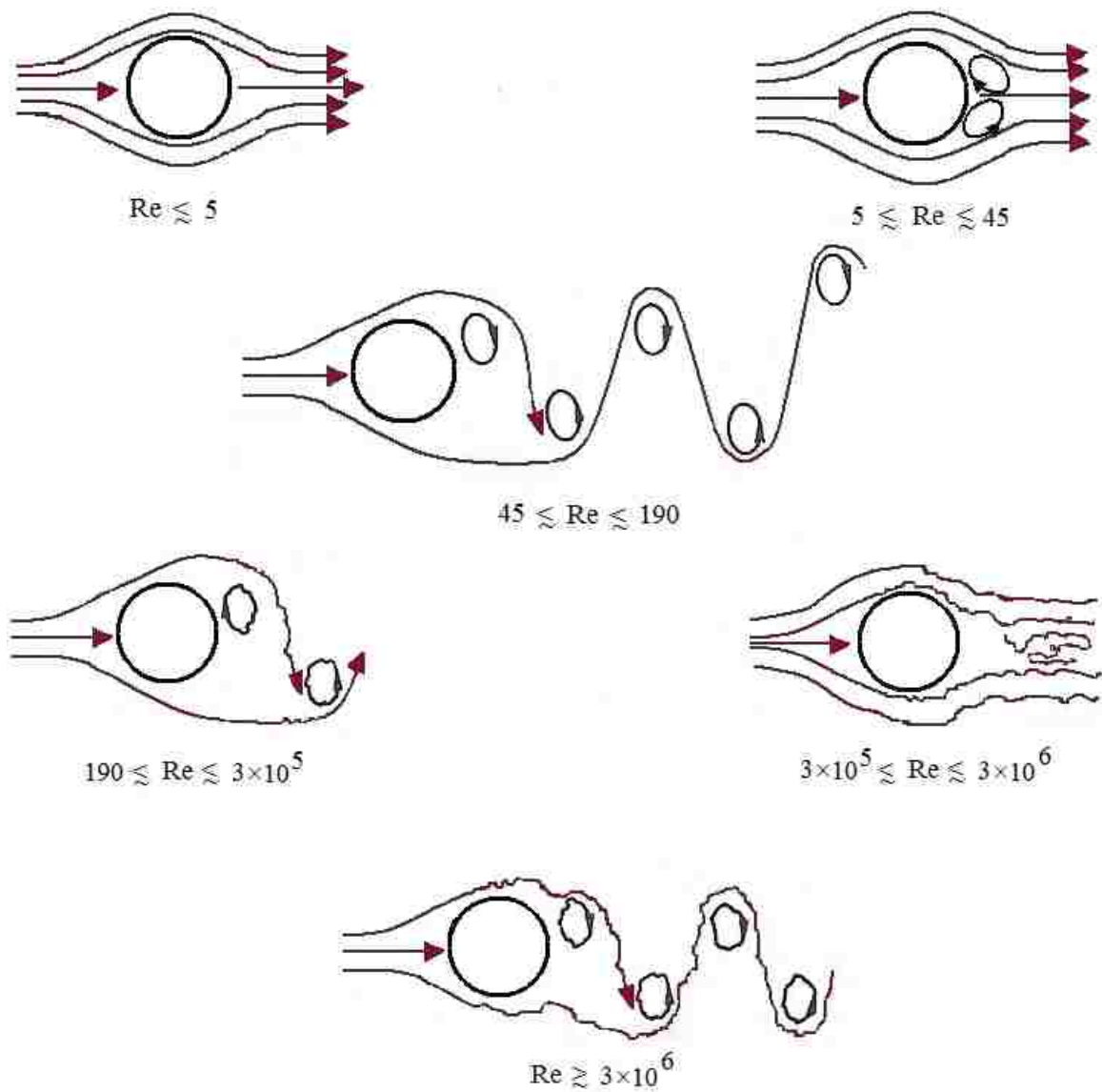


Fig. 2 Flow pattern for a circular cylinder in laminar cross flow

2.2. Turbulence flow past a single circular cylinder

Since most practical applications occur in different degrees of flow turbulence, it is imperative to have a proper knowledge of the free-stream turbulence effects on a circular cylinder. A majority of the wind tunnel tests were conducted in smooth flow. Some previous researches (e.g. 12-14) have shown strong influence of free-stream turbulence existed on the flow around a circular cylinder.

Surry [15] conducted a series of experiments in a low-speed closed-circuit wind tunnel at Re values of 3.38×10^4 , 3.62×10^4 , 3.62×10^4 , and 4.42×10^4 . He studied the effect of high turbulence intensity (greater than 10%) and scale (ranging from 0.35 to 4.3) on the flow over a circular cylinder as shown in Fig. 3. The mean drag measurements and Strouhal frequency indicate that the large scale turbulence was qualitatively equivalent to an increase in the effective Re number. He concluded that the mean drag coefficients measured in the turbulent flow were consistent with an equivalent increase in Re compared to the smooth flow. Also, he showed that when $Tu = 10\%$, by increasing Λ/D from 0.35 to 4.3 the drag coefficient value increased by 25%.

Younis [12] studied experimentally the influence of free-stream turbulence intensity ($Tu = 0.5\%$, 5% , 7% , and 9%) and the integral length scale ($\Lambda/D = 0.35$ to 1.05) on the drag coefficient of a circular cylinder in cross flow, over a Re range from 6.4×10^3 to 1.8×10^4 . This study has confirmed the trend of decreasing drag coefficient as the value of Tu increases as shown in Fig. 3. Also, with decreasing the value of Λ/D the drag coefficient decreases too.

Blackburn and Melbourne [16] showed experimentally the effect of turbulence on the forces of a circular cylinder for a Re range of 1×10^5 to 5×10^5 , high turbulence

intensities (up to 18%) with small scale ($\Lambda/D = 0.5$). They confirmed that increasing the turbulence intensity promoted early transition to a supercritical flow.

Cheung and Melbourne [17] observed that at critical and supercritical Reynolds numbers up to 10^6 , increasing turbulence intensity from 0.4% to 9.1% causes the drag coefficient to decrease in the subcritical regime and opposite influence occurs in the supercritical regime, as shown in Fig. 3. The integral length scale was fixed at $\Lambda/D = 1.8$. Their experiment results showed an earlier transition to the percritical regime at the higher turbulence intensity compared with the smooth flow case (standard curve band).

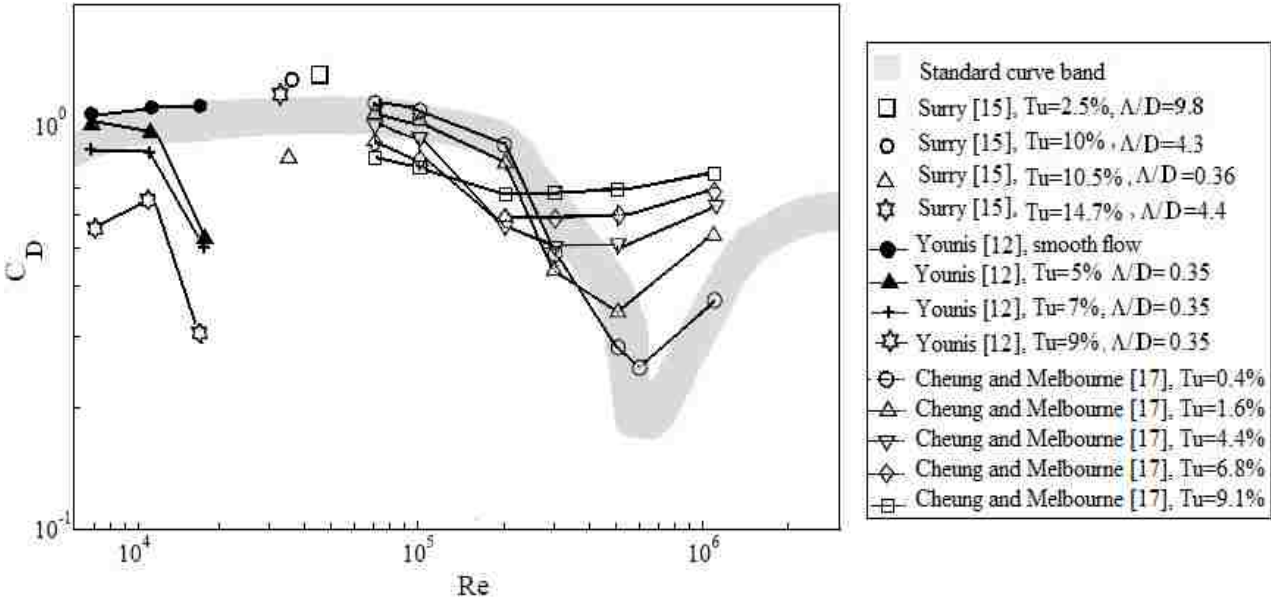


Fig. 3 Turbulence intensity and Λ/D effects on $C_D - Re$ relationship

2.3. Flow around two circular cylinders

When two circular cylinders are subjected to a steady flow, the resulting forces and flow pattern in the wake may be very different from those found on a single cylinder at the same Reynolds number. The fluid flow behaviour around two circular cylinders depends on the spacing between the cylinders, the orientation of the cylinders relative to the oncoming flow, Reynolds number, surface roughness, and free-stream turbulence. Two circular cylinders of equal diameter, D , can be classified in three basic categories of possible arrangements based on the angle between the centre connection line of the cylinders and the wind direction: (a) in tandem ($\alpha = 0^\circ$), (b) side-by-side ($\alpha = 90^\circ$), and (c) staggered ($0^\circ < \alpha < 90^\circ$) as shown in Fig. 4.

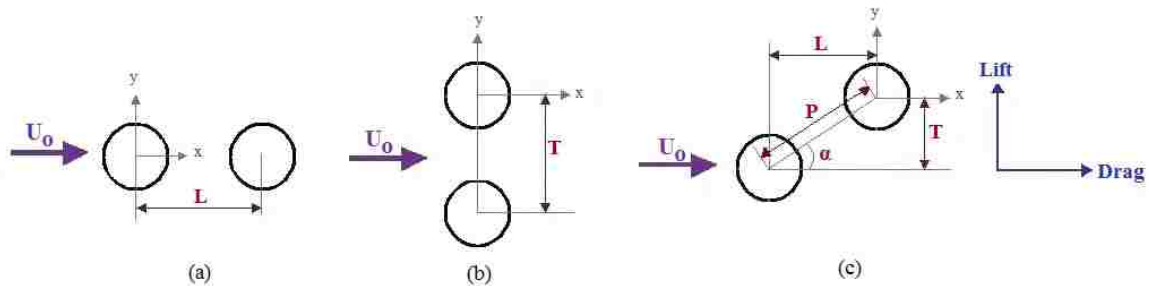


Fig. 4 Two circular cylinders arrangements in cross flow (a) in tandem, (b) side- by- side, and (c) staggered

Much work has been done on two circular cylinders in tandem and in side-by-side arrangement, shown in Fig. 4(a, b), where the geometry is set by L (the longitudinal spacing between the centres of the two cylinders), and T (the traverse spacing between the centres of the two cylinders). The spacing is typically expressed as dimensionless longitudinal and transverse pitch ratios, L/D and T/D , respectively.

The most general geometry of two circular cylinders of equal diameter, D , is known as the staggered arrangement, shown in Fig. 4(c). The geometry of the staggered cylinders is usually described by non-dimensional form, L/D and T/D . Alternatively, the geometry of a pair of cylinders may be defined by the centre-to-centre pitch between the cylinders, P , (or by the dimensionless centre-to-centre pitch ratio, P/D) and the angle of incidence, α , as shown in Fig. 4(c).

When two cylinders are placed in close proximity to each other, the flow field around them in cross flow is very complex. According to Sumner [18] this complexity of the flow arises from the interaction of four free shear layers, two Karman vortex streets formation and interaction between them and shedding processes (see Fig. 5).

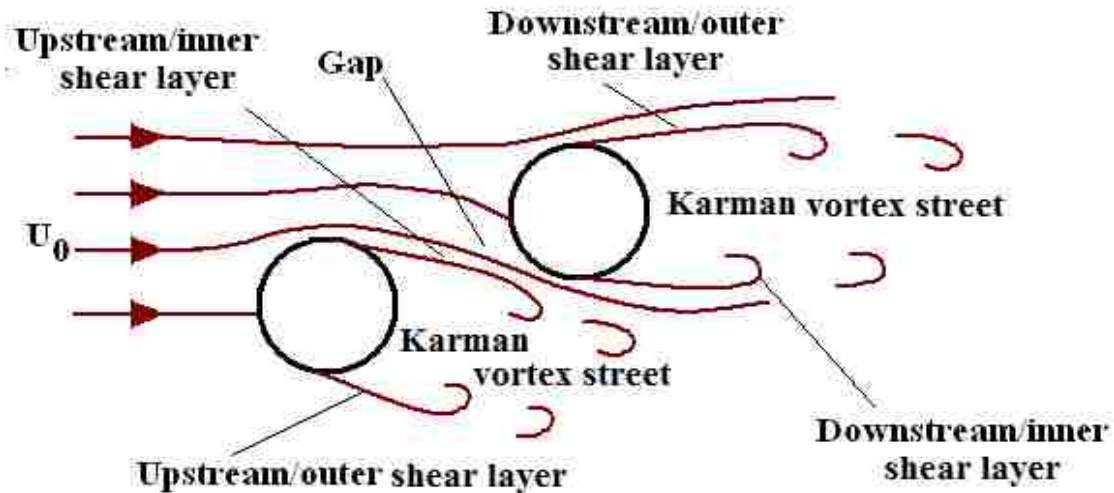


Fig. 5 Shear layer and vortex formation for two staggered circular cylinders in cross flow, after Sumner [18]

Hori [19] carried out the first systematic measurements of surface pressure distribution around one of the two cylinders in staggered arrangement at a Reynolds number $Re = 8 \times 10^3$. The gap between the cylinders was set at $P/D = 1.2, 2.0$ and 3.0 . He

calculated the lift and drag coefficients by integrating the pressure distributions. He stated that the lift component may be towards or away from the upstream cylinder wake depending on the arrangements of the cylinders.

2.3.1. Basic interference flow regimes

Zdravkovich [20] shows that there are two basic kinds of interference between two circular cylinders in cross flow, based on the location of the downstream cylinder with respect to the upstream one (as shown in Fig. 6): (i) Wake interference, when one cylinder is near to or completely submerged in the wake of the other, and (ii) proximity interference, when the two cylinders are close to each other, but neither is submerged in the wake of the other. The no-interference region is where interference is negligible and each cylinder behaves like a single circular cylinder.

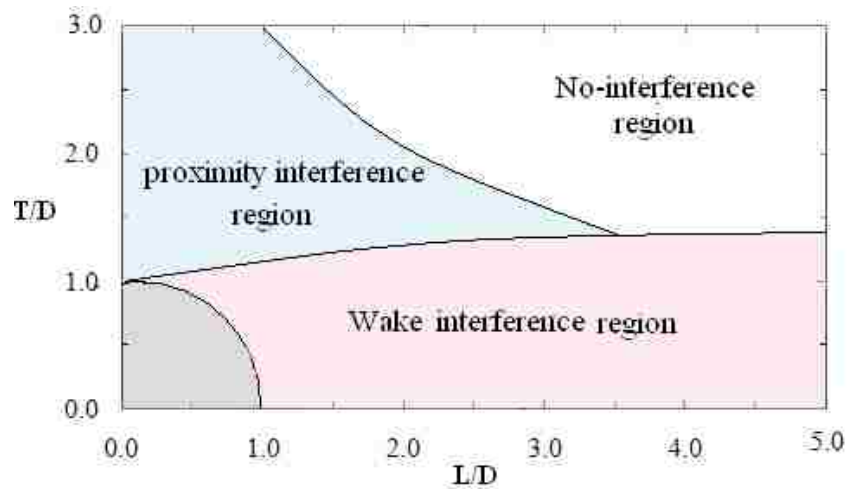


Fig. 6 Wake and proximity interference boundaries for two identical staggered circular cylinders, based on Zdravkovich [20]

A map of the lift and drag coefficients for the downstream cylinders of two circular cylinders in the subcritical Re range, as furnished by Zdravkovich [20], is regenerated here as Fig. 7(a, b). Zdravkovich [20] observed two different flow regions in the wake interference region for two staggered cylinders. First, he found that when $L/D > 2.8$ and $T/D > 0.4$ (wake displacement region, see Fig. 7(a)), the displacement of the fully formed wake of the upstream cylinder by the flow around the downstream cylinder produces the “outer” lift force. Figure 7(a) also explains that the outer lift force reaches the maximum value near the edge of the wake boundary when $T/D > 0.4$. Second, he observed that when $1.1 < L/D < 3.5$ and $T/D = 0.2$ (gap flow region, see Fig. 7(b)), an “inner” lift force is induced by the strong gap flow between the cylinders.



Fig. 7 Static force coefficient map for a downstream cylinder in the subcritical Re , $4 \times 10^4 \lesssim Re \lesssim 2 \times 10^5$ (a) lift coefficient, and (b) drag coefficient, after Zdravkovich [20]

Gu and Sun [21] extended Zdravkovich's [20] classification to three types. The three types of flow interference suggested by Gu and Sun [21] are (a) wake interference, where the inner shear layer separated from the upstream cylinder touches (no reattachment) the downstream cylinder and there is no stagnation point on the downstream cylinder (at $\theta = 0^\circ$, $C_p \neq 1$), (b) shear layer interference, where the inner shear layer separated from the upstream cylinder reattaches onto the downstream cylinder. In this kind of interference, there is a stagnation point at $\theta = 0^\circ$ and the C_p value is 1.0, and (c) neighbourhood interference, where each cylinder has its own wake region and only the wake shapes of two cylinders are distorted. Their study was limited to staggered configurations in the high subcritical regime ($Re = 2.2 \times 10^5$ and 3.3×10^5).

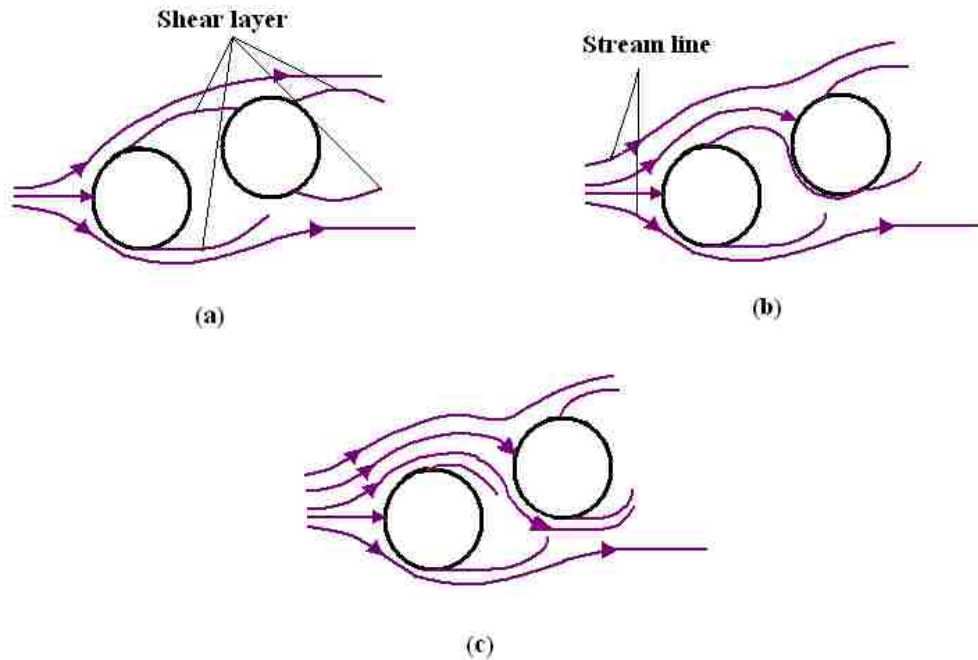


Fig. 8 Flow pattern around two staggered circular cylinders in cross flow (a) the interference of wake, (b) the interference of shear layer, and (c) the interference of neighbourhood, $Re = 2.2 \times 10^5$ and 3.3×10^5 , after Gu and Sun [21].

Based on the flow visualization experiments, nine different flow patterns around two circular cylinders in staggered arrangement ($P/D = 1$ to 5 and $\alpha = 0^\circ$ to 90°) were identified by Sumner et al. [22], as shown in Fig. 9. Experiments were conducted within the low subcritical Reynolds number regime ($Re = 850$ to 1900). The processes of shear layer reattachment, induced separation, vortex pairing and synchronization, and vortex impingement, were observed. From the behaviour of the experimental data by Sumner et al. [22], the nine flow patterns can be broadly classified by the pitch ratio as (a) closely spaced ($P/D < 1.5$), (b) moderately spaced ($1.5 \lesssim P/D \lesssim 2.5$), and (c) widely spaced ($P/D > 2.5$), as shown in Fig. 9.

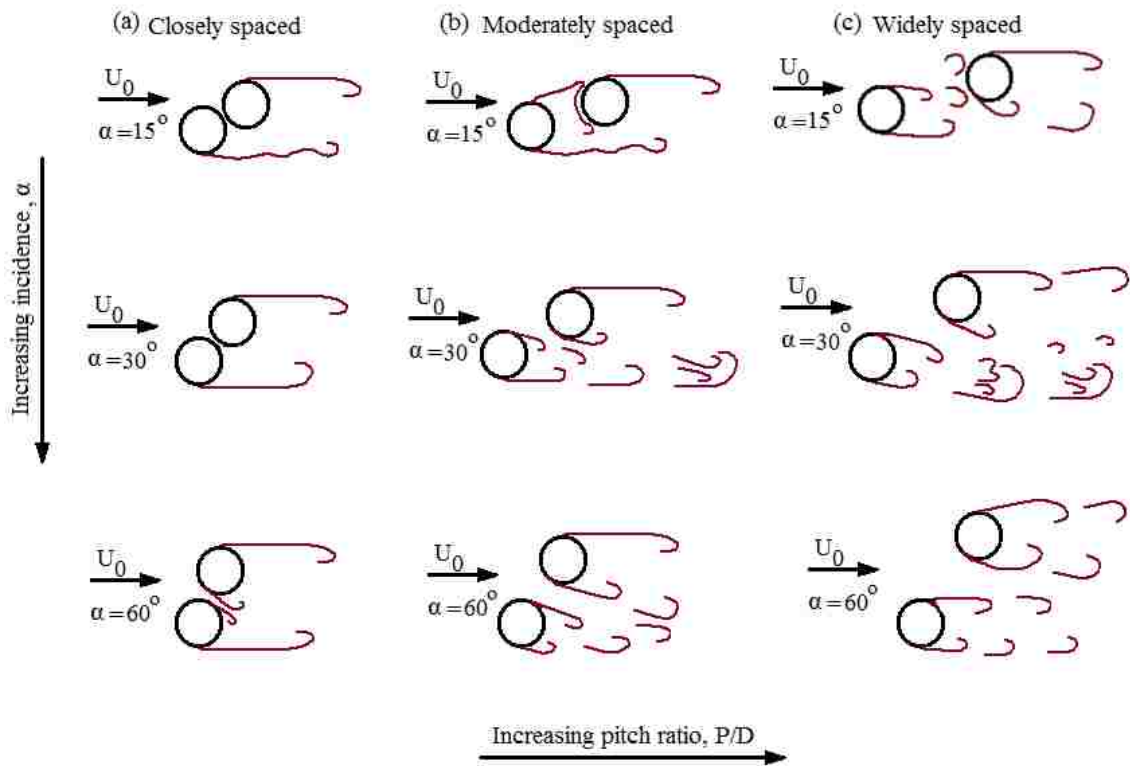


Fig. 9 Flow patterns for two identical staggered circular cylinders in cross flow (a) closely spaced, (b) moderately spaced, and (c) widely spaced, $850 \leq Re \leq 1900$, based on

Sumner et al. [22]

Both Zdravkovich [20] and Sumner et al. [22] showed that when two staggered cylinders are closely spaced (Fig. 9(a)), two cylinders behave as a single cylinder for nearly the entire range of α , and a single vortex street is found in the combined wake of the cylinders. As shown in Fig. 9(a), when the incident angle is very small ($\alpha = 15^\circ$) the single cylinder flow pattern is characterized by instabilities in the outer shear layer from the upstream cylinder. As well as for $\alpha = 30^\circ$, the outer shear layers of both cylinders are of similar length. At high incident angle ($\alpha = 60^\circ$), the gap flow between the cylinders enters the wake region. This gap flow may be redirected towards either upstream or downstream cylinder based on the value of the incident angle. Sumner and Akosile [23] reported that when two staggered cylinders are closely spaced, $P/D < 1.5$, the mean drag coefficient for the upstream cylinder may be up to 30% higher or up to 25% lower than the value for a single cylinder, depending on the incidence angle, α . It is important to note that for $\alpha < 30^\circ$, the upstream cylinder attained negative lift force, meaning that the upstream cylinder is pulled towards the downstream cylinder. For $\alpha > 30^\circ$, the lift force on the upstream cylinder is positive (outward-directed), indicating that the upstream cylinder tends to be repelled away from the downstream cylinder. Similar to the upstream cylinder, at lower incidence angles, the lift coefficient for the downstream cylinder is negative but becomes positive at higher incidence angles. The mean drag coefficient of the downstream cylinder remains close to the drag coefficient value for a single cylinder.

As shown in Fig. 9(b) for moderately spaced staggered cylinders when the incident angle is very small ($\alpha = 15^\circ$), the inner shear layer separated from the upstream cylinder reattaches onto the outer side of the downstream cylinder. As the incident angle increase ($\alpha = 30^\circ$ and 60°) two distinct vortex street processes occur from both cylinders rather

than a single vortex process from the cylinders as a whole. Sumner et al. [24] mentioned when a pair of staggered cylinders are moderately spaced (Fig. 9(b)), the mean drag coefficient of the upstream cylinder may be up to 30% higher or up to 30% lower than the value for the single cylinder over nearly the entire range of α . For small incidence angles, $\alpha < 30^\circ$, the upstream cylinder experienced either a very small negative value or is zero. For $\alpha > 30^\circ$, the lift force on the upstream cylinder is positive. For moderately spaced staggered cylinders, $1.5 \lesssim P/D \lesssim 2.5$, the behaviour of the force coefficients on the downstream cylinder is similar to the behaviour of the force coefficients for the closely spaced staggered cylinders.

Sumner et al. [22] indicated that for widely spaced staggered arrangement (Fig. 9(c)), $P/D > 2.5$, vortex shedding occurs from both cylinders because of the large spacing between the cylinders, and shear layer reattachment will generally not occur. At smaller incidence angles ($\alpha = 15^\circ$, as shown in Fig. 9(c)) for the widely spaced staggered cylinders, the inner shear layer from the upstream cylinder begins to periodically roll up into Karman vortices, and the shear layer reattachment is no longer observed. Also, the wake of the cylinder is characterized by a single vortex street. At an incidence angle around 30° , the inner shear layer of the upstream cylinder is deflected through the gap between the cylinders. At higher incidence angles, $\alpha = 60^\circ$, vortex shedding occurs from both cylinders because the cylinders are spaced sufficiently far apart from each other. For the upstream cylinder, the forces are mostly unchanged from that of a single cylinder. It means that the mean lift coefficient is nearly zero at all incidence angles. In widely spaced staggered configuration, the drag coefficient for the downstream cylinder is

positive at all incidence angles, and it approaches the single cylinder value as α is increased.

2.4. Turbulence flow past two circular cylinders

The group of two cylinders in turbulence flow is likely to occur most often in engineering practices, even though it is the least studied care. Liu et al. [25] tested groups of two, three, and four circular cylinders arranged in-line (in tandem), in smooth and turbulence flow ($Tu = 5.6\%$) over a Re range of 2.7×10^4 to 8.6×10^4 . The integral length scale, Λ/D , was varied from 0.67 to 1.01. For two identical circular cylinders arranged in-line, it was found that the drag coefficient, C_D , for the upstream cylinder to be less affected by the downstream cylinder (the upstream cylinder behaved like a single cylinder) and depends more on the Reynolds number compared to the smooth flow case. The drag coefficient for downstream cylinder varied with spacing between two cylinders. For downstream cylinder in smooth flow, when $L/D \lesssim 3.5$, the value of the drag coefficient became much smaller (became negative value) compared with the value in turbulence flow. When $L/D > 3.5$, the value of the drag coefficient in smooth flow is still smaller than the one in the turbulence flow but the value is positive. Also, it was observed that the mean lift coefficient, C_L , was near zero for each cylinder either in turbulence or smooth flow.

The effect of free-stream turbulence and P/D on the flow behaviour around two cylinders in tandem arrangement was investigated by Ljungkrona et al. [26]. The two cylinders were arranged at pitch ratios from $P/D = 1.25$ to 5 at $Re = 2.0 \times 10^4$. The experimental results showed that the turbulence has an influence on the flow patterns

around the cylinders when $P/D \lesssim 2$. At $2 \lesssim P/D \lesssim 5$, no clear influence of the turbulence was seen when the turbulence intensity was varied.

The drag and lift coefficients on both upstream and downstream cylinders in staggered arrangement ($\alpha = 11^\circ$), in the turbulence and smooth flow was reported by Liu [27] at $Re = 4.2 \times 10^4$ in $Tu = 5.6\%$, and $1 \lesssim \Lambda/D \lesssim 1.36$. As shown in Fig. 10, the flow turbulence shows very little effect on the C_D of the upstream cylinder over the range of $1.0 \lesssim L/D \lesssim 3.5$. It can be observed that, C_D of upstream cylinder in smooth flow is less than that in turbulence flow except at $L/D = 1.5$. It was shown that in the smooth flow case, at $L/D = 1.5$ (critical spacing), the drag coefficient abruptly increased to 1.2~1.25 and had a slow increase with increasing spacing beyond that. At the same spacing where the upstream drag coefficient increased, the downstream cylinder showed a sharp decrease. Zdravkovich [28] explained this behaviour was the result of a bi-stable flow pattern between the two cylinders at the critical spacing. For the downstream cylinder, the sharp increase of C_D at the critical spacing is much less apparent in the turbulence flow case than the smooth flow case.

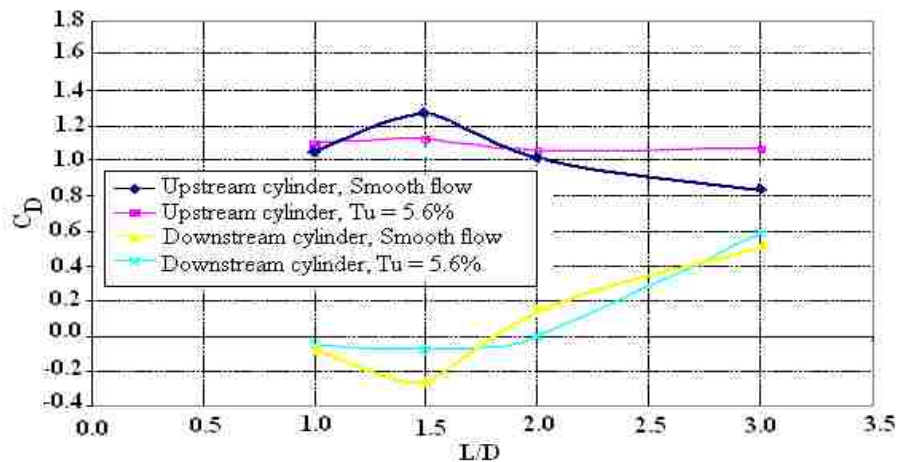


Fig. 10 Variation of C_D with L/D for two staggered cylinders ($\alpha = 11^\circ$) at $Re = 4.2 \times 10^4$ in smooth and turbulence flow, after Liu [27]

Price [29] showed the effect of turbulence intensity and surface roughness on the characteristics of the force coefficients for two circular cylinders in a staggered arrangement, $P/D = 2.2$, in the range of $1.7 \times 10^4 \lesssim Re \lesssim 8 \times 10^4$ in turbulence flow ($Tu \lesssim 11\%$). It was shown that for low turbulence intensities, $Tu \lesssim 2\%$, the Reynolds number has no effect on drag coefficients of the upstream cylinders. Raising the turbulence intensity to 11% causes the drag coefficient of the upstream cylinder to begin to decrease at $Re = 1.7 \times 10^4$ and then it falls to 1.0 at $Re = 3.5 \times 10^4$, see Fig. 11.

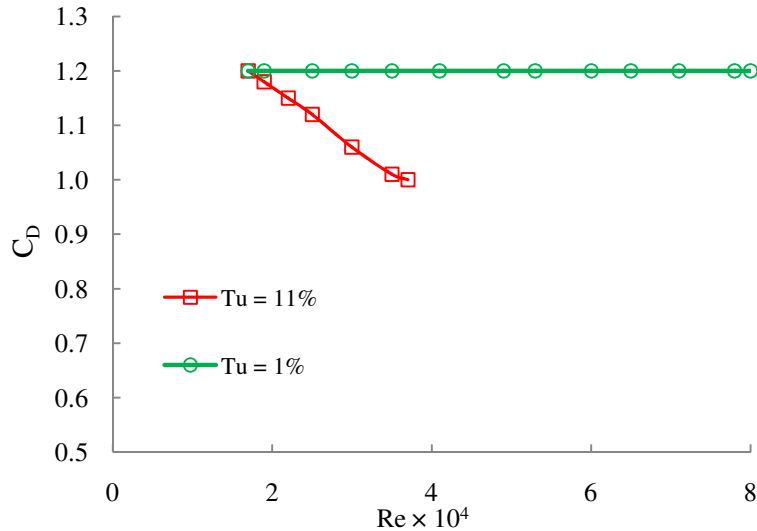


Fig. 11 Variation of C_D with Re for the upstream cylinder of two staggered cylinders in turbulence flow, $1.7 \times 10^4 \lesssim Re \lesssim 8 \times 10^4$, after Price [29].

Gu et al. [30] tested two circular cylinders in tandem, side-by-side, and staggered arrangement at $Re = 6.5 \times 10^5$ (supercritical Reynolds number) in turbulence flow ($Tu = 10\%$). The integral length scale, Λ/D , was fixed at 0.7. It was shown that the vortex shedding frequency peak was absent behind a single cylinder for $Tu = 0.12\%$ and present for $Tu=10\%$ ($St = 0.26$). The pressure distributions, and drag and lift coefficients on two circular cylinders in various arrangements were presented. It was shown that for the staggered arrangement in turbulence flow ($Tu = 10\%$), the interference effect of the downstream cylinder on the upstream cylinder is larger than that of the upstream cylinder on the downstream cylinder. Figure 12(a, b) shows C_D and C_L maps for downstream cylinder at $Re = 6.5 \times 10^5$, and $Tu = 10\%$. These plots are remarkably different from the force coefficient map by Zdravkovich [20] as shown in Fig. 7(a, b). Figure 12(a, b) shows that the $Tu= 10\%$ demolished both the gap flow and wake displacement flow regions. Their experiments showed that C_D on the downstream cylinder is always less than that for a single cylinder.



Fig. 12 Constant C_D and constant C_L lines for downstream cylinder at $Re = 6.5 \times 10^5$ and $Tu = 10\%$ (a) drag coefficient, and (b) lift coefficient, ● signifies the measurement points,

after Gu et al. [30].

CHAPTER III

DESIGN AND METHODOLOGY

3.1. Wind tunnel setup

This work was conducted in a closed loop wind tunnel with a working length of 4.0 m as shown in Fig. 13. The test section of the tunnel is 0.762 m high and 0.762 m wide at the inlet. To maintain the same velocity within the x-direction in the wind tunnel, the height of the test section increases gradually to 0.800 m at the cylinders locations. A preliminary test indicated that the turbulence intensity of the flow in the empty wind tunnel was less than 0.5% and it will be referred to as smooth flow. In this study, the wind tunnel is capable of generating free-stream velocity up to 20 m/s when the test section is empty. In the presence of a perforated plate, the maximum attainable free-stream velocity is around 11 m/s.



Fig. 13 An overall view of the closed-loop wind tunnel utilized in this study

The free-stream velocity is in the +x-direction, which is also the positive drag direction, while positive lift is in the +y direction. The free-stream velocity was measured with a pitot - static tube connected to a digital manometer (Dwyer series 475 mark III, the hysteresis is $\pm 0.1\%$ of the full scale (0 – 0.249 kPa) and the accuracy is $\pm 0.5\%$ of the full scale (0 – 0.249 kPa)). The pitot - static tube was placed at the centre of the test section. Prior to any experiment, the pitot - static tube was removed from the wind tunnel, after checking the free- stream velocity, to prevent any interference with the flow. In order to have a stable wind speed, a period of 15 minutes is needed to warm up the wind tunnel before taking any measurement.

3.2. Cylinder models

Two circular cylinders of equal diameter were mounted horizontally in staggered configuration as shown in Fig. 14. The model circular cylinders were aluminum tubes. All the cylinders were sanded, polished, and painted in dark green. The cylinder's surfaces were buffered by using NOVUS plastic polishes No. 2 and subsequently No. 1 to improve their smoothness. The surface roughness was tested in the laboratory of the University of Windsor and the average value of the roughness was 5.81×10^{-7} m. The relative roughness (surface roughness / smallest cylinder diameter) was less than 0.00002, see Appendix A. This value, together with the Re range, indicate that our cylinders can be considered as smooth cylinders according to the Moody chart. Three cylinder sizes were used in this study, with outside diameters of $D = 22.2, 25.4,$ and 38.1 mm and a length $l = 657$ mm, giving aspect ratios (cylinder length to diameter ratio) of $AR = l/D = 29.6, 25.9,$ and 17.2 for $D = 22.2, 25.4,$ and 38.1 mm, respectively. A dummy end (49 mm) with the same corresponding cylinder size was fitted to the cylinder and the

gap between the end cap and the dummy end was 3 mm, so that the cylinder was located outside the boundary layers developing on the side walls of the wind tunnel [12], see Fig. 14(c). A solid blockage ratio was kept at less than 5% per cylinder for all tests. No correction was applied to blockage ratio since, for two cylinders with interfering wakes, the blockage was small and no well-tested method was found. The upstream cylinder was located horizontally across the centre line of the wind tunnel. It was located 0.381 m above the floor of the wind tunnel and 3.33 m downstream of the test section start. In this study, the ratio of the longitudinal spacing between the centres of two cylinders over the diameter of the cylinder (L/D) and the ratio of transverse spacing between the centres of the two cylinders over the diameter of the cylinder (T/D) were kept constant at 4 and 1, respectively.

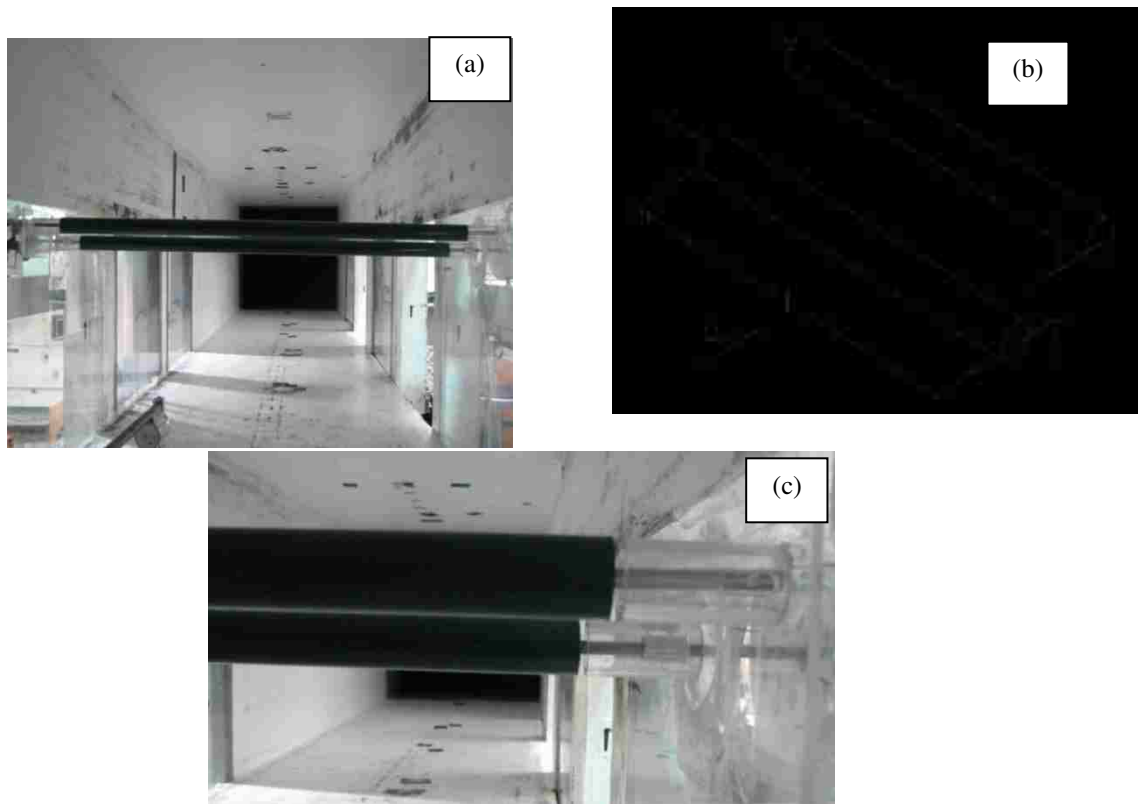


Fig. 14 Two cylinders in cross flow (a) two cylinders in the wind tunnel looking upstream, (b) two staggered cylinders set-up, and (c) actual setup with dummy ends looking upstream

3.2.1. Drag and lift forces measurements

The dynamic force measuring system consisted of two load cells supporting upstream or downstream cylinder in each test. The instrumented cylinder was supported with two load cells through rods that were inserted into the cylinder and secured by setscrews. Two ATI Gamma type six-component strain force/torque transducers were connected to the two ends of the instrumented cylinder. The load cells are fixed to the wind tunnel by two aluminum angles mounted to the outside of the wind tunnel, as shown in Fig. 15.

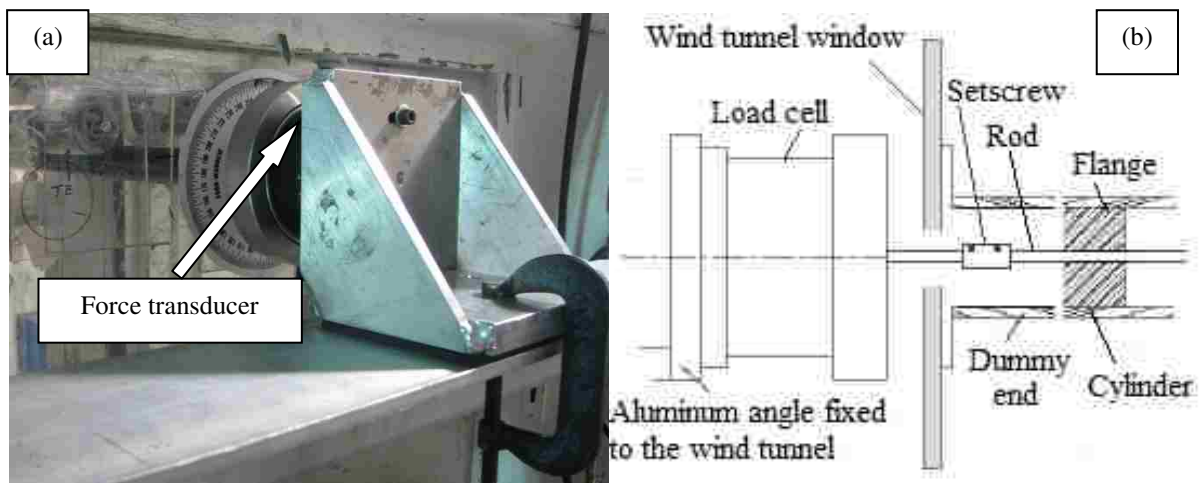


Fig. 15 Actual set-up of the load cell (a) load cell connection to the wind tunnel, (b) load cell connection to a 49 mm dummy end and cylinder

The load cell with ± 65 N range and a resolution of $1/80$ N was mounted on the right-side of the wind tunnel when looking downstream, while the other load cell with ± 32 N range and a resolution of $1/160$ N was mounted at the left-side of the wind tunnel when looking downstream. The sampling frequency was set at 2 kHz, and 150000

samples (in 75 seconds) were taken at each test. Appendix B includes the procedure of the selection of the sample number and sample frequency.

The manufacturer calibrations of transducers were carefully checked using different weights before the experiments. The x-axis was parallel to the direction of the flow, while the positive y-axis was pointing up perpendicularly (within $\pm 1^\circ$). Three different weights (20g, 50g, and 100g) via string were connected to the centre of the cylinder as shown in Fig. 16. The drag and lift forces were computed as the summation of the force in x-direction and y-direction from two load cells, respectively; see Fig. 17. The results were consistent with the manufacturer calibration report and theoretical force ($F = mg$, where F is the force, m is the mass, and $g = 9.81 \text{ m/s}^2$ is the gravity).

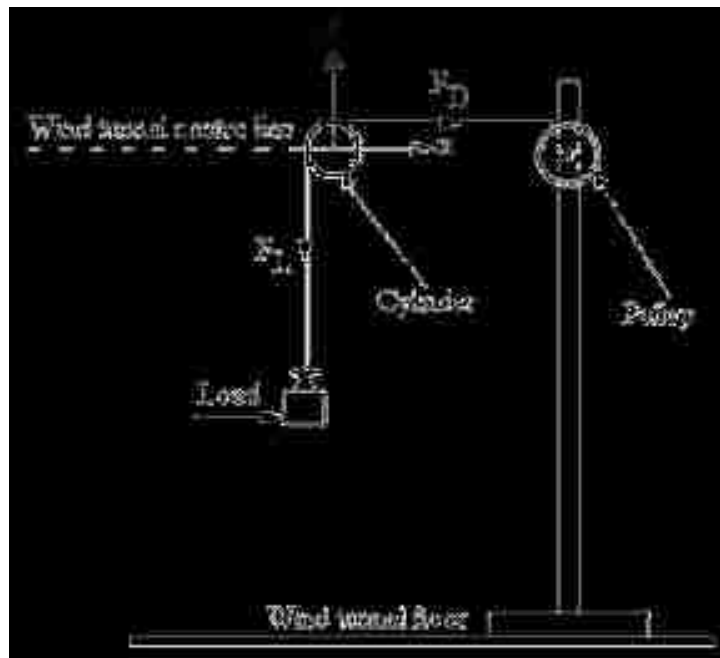


Fig. 16 Load cell calibration check set-up

In each test, one of the two cylinders was instrumented with two load cells, while the other cylinder was fixed to the wind tunnel through supporting rods that were inserted into the cylinder and the window of the wind tunnel (Fig. 14).

In this study, the drag and lift coefficients, C_D and C_L , are defined, respectively, as follows:

$$C_D = \frac{F_D}{\frac{1}{2}\rho U_0^2 D l} \quad (2)$$

$$C_L = \frac{F_L}{\frac{1}{2}\rho U_0^2 D l} \quad (3)$$

where, F_D and F_L are drag and lift forces, respectively, ρ , is the density of air, U_0 is a free-stream velocity, D is the diameter of the cylinder, and l is the length of the cylinder.

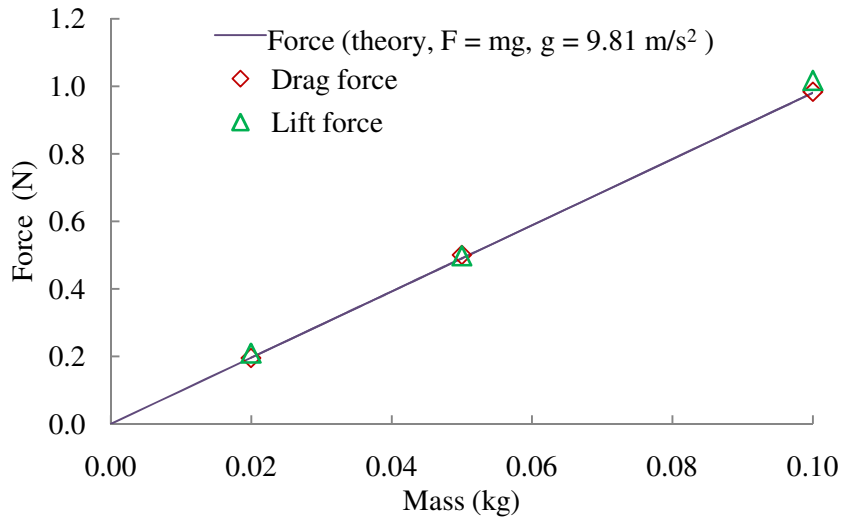


Fig. 17 Force (N) versus mass (kg)

3.2.2. Pressure distribution measurements

For all pressure-based tests, the cylinders were fitted with only one pressure tap ($r = 1$ mm, where r is the static pressure port diameter) due to limited space inside the cylinders. The instrumented cylinder was rotated in 22.5° increments, until a complete pressure distribution around the cylinder was obtained. The instrumented cylinder was rotated manually by using an adhesive back protractor mounted on the right end of the cylinder (when looking upstream) fixed to the wind tunnel, as shown in Fig. 18 (a, b). The pressure at each angular location was measured using a digital manometer (Dwyer series 475 mark III). One port of the manometer was connected via a 6.3 mm diameter tubing to a 1 mm diameter pressure tap, located at the mid-span position of the instrumented cylinder. The second manometer port was connected via a 6.3 mm diameter tubing to a flush-mounted hole ($r = 1$ mm, where r is the static pressure port diameter) at the floor of the wind tunnel, located at 3D upstream of the upstream cylinder. For each case, the two cylinders were first aligned (within $\pm 1^\circ$) so that they were parallel to each other and perpendicular to the x -axis of the wind tunnel.

In this study, the mean pressure coefficient, $C_p(\theta)$, is defined as:

$$C_p(\theta) = \frac{P(\theta) - P_\infty}{\frac{1}{2}\rho U_0^2} \quad (4)$$

where θ is the azimuth angle measured from wind direction, positive anticlockwise, see Fig. 18(c). $P(\theta)$ is the pressure measured on the surface of cylinder, ρ is the density, and U_0 is the free-stream velocity of flow.

The drag and lift coefficients, C_D and C_L , are obtained by integrating the pressure distributions around the cylinder as follows:

$$C_D = -\frac{\pi}{n} \sum_{i=1}^n C_p \cdot \cos \theta_i \quad (5)$$

$$C_L = -\frac{\pi}{n} \sum_{i=1}^n C_p \cdot \sin \theta_i \quad (6)$$

where $n = 16$ is the number of pressure readings around the cylinder.

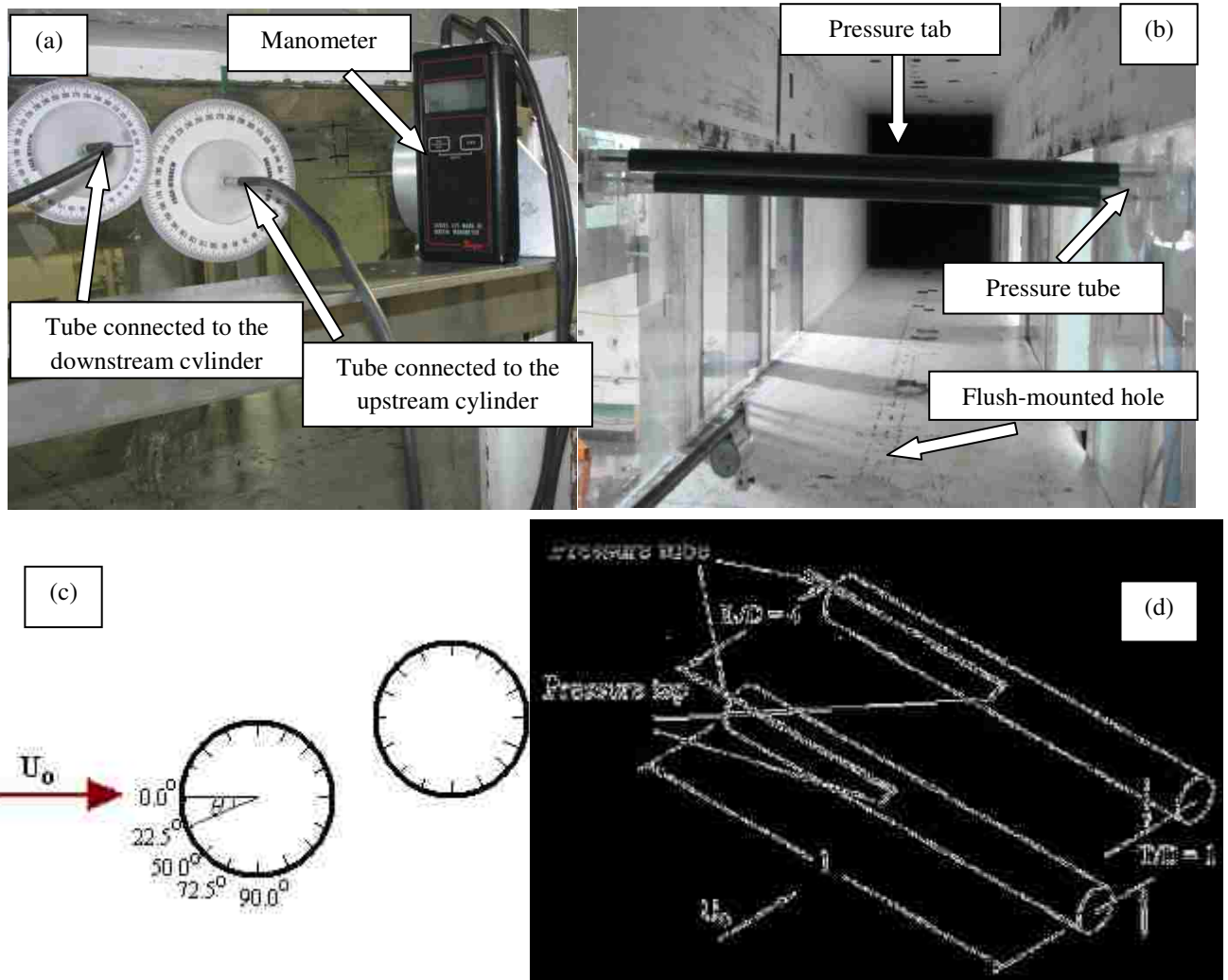


Fig. 18 Detail of the pressure measurement set-up (a) manometer connection to the cylinder outside the wind tunnel looking upstream, (b) pressure tab connection to the wind tunnel looking upstream, (c) azimuth angle (θ), and (d) pressure tubes inside the cylinders.

3.3. Perforated plates

In the present study, a perforated plate was installed just upstream of the test section to generate simple turbulence of the desire intensity and integral length scale. Three perforated plates with different size of hole diameters were used. These are 6 mm thick aluminum plates which contain hole diameters of $d = 25.4$ mm, 38.1 mm, and 50.8 mm as illustrated in Fig. 19 and Fig. 20. All three plates have the same external dimensions of 750 mm by 750 mm. The solidity ratio of the plate was kept at 43% for all three perforated plates. It is important to note that to obtain quasi-isotropic turbulence the turbulence producing grids should have a solidity ratio of less than 60% [31]. In this study a perforated plate with a thickness of 6 mm, and solidity ratio of 43% was chosen based on specific design requirements in order to generate quasi-isotropic and approximated homogeneous turbulence flow [32]. Also, to minimize the influence of the plate thickness on the turbulence flow field an orifice angle of 41° was selected.

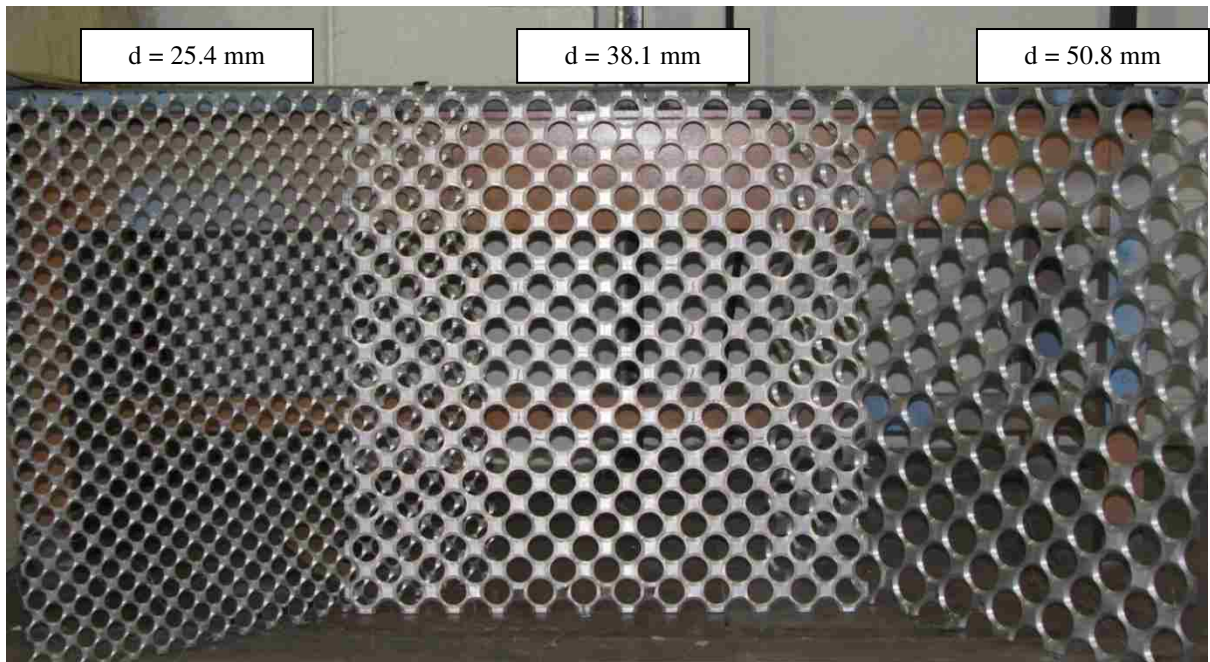


Fig. 19 The orificed perforated plates

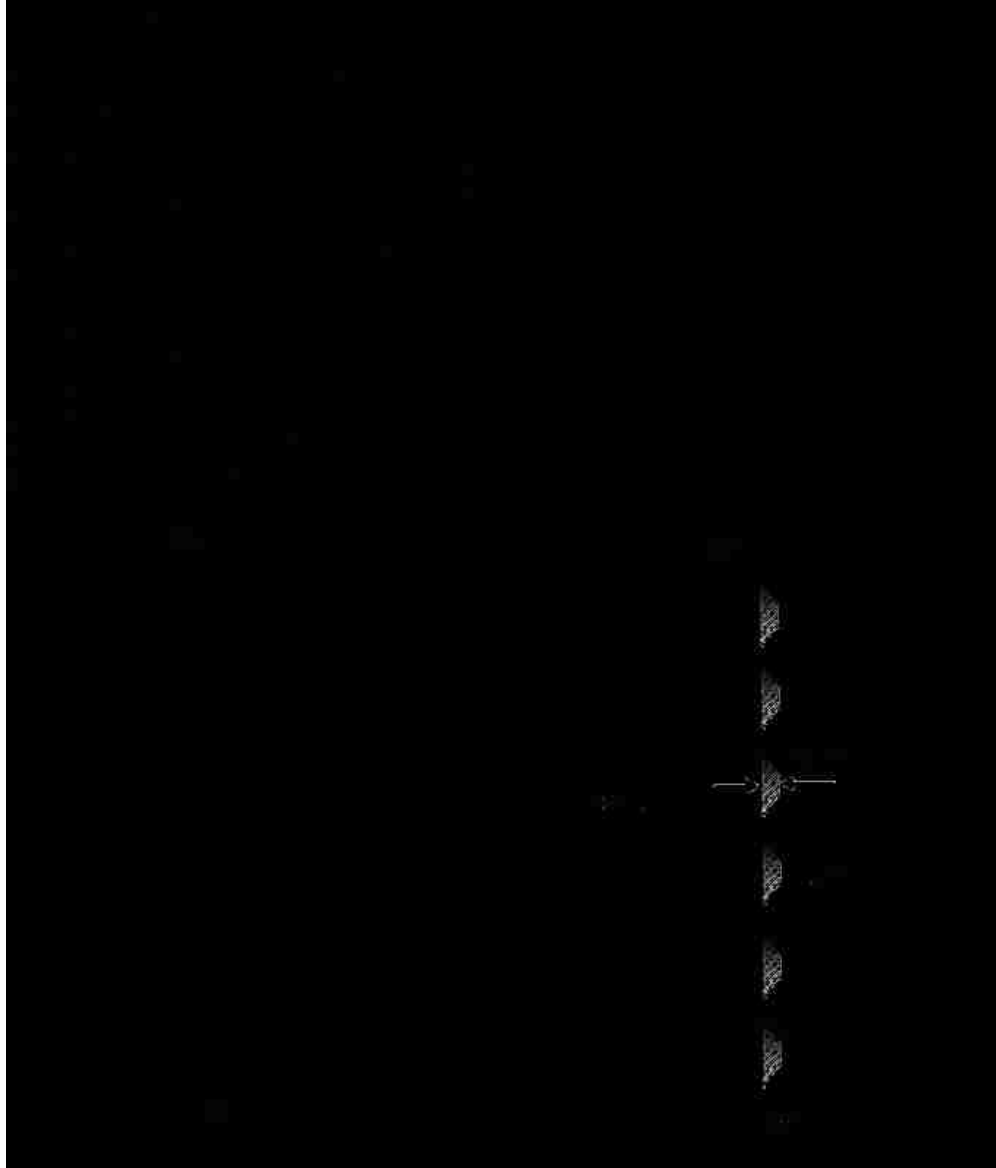


Fig. 20 Schematic of the perforated plates (a) $d = 25.1$ mm, (b) $d = 38.1$ mm, (c) $d = 50.8$ mm, and (d) cross section of the plate

3.4. Hot-wire anemometer

The free-stream velocity and the wake of the cylinders were measured by a 1D hot-wire probe of DISA type 55p11 with a Dantec streamline 55C90 constant-temperature anemometer (CTA) module installed within a Dantec 90N10 frame. The

velocity measurement was conducted at the desired location ($10D$ to $50D$) downstream of the perforated plate. For the wake survey, the hot-wire probe was located $X/D = 2$ behind the downstream cylinder. If the hot-wire probe is very near to the cylinder ($X/D < 2$), the prominent wake structure may be not captured. Too far behind the cylinder ($X/D > 2$), the wake became very wide and not very feasible. The hot-wire probe traversed in the vertical mid-span plane, see Fig. 21. The stream-wise mean velocity, turbulence intensity, and root mean square of velocity profiles are measured by traversing a hot-wire probe using a 2D traverse system over the range $-4 \lesssim y/D \lesssim 4$ with an interval of $\Delta y = 2.5 \times 10^{-3}$ m.

The sample frequency is determined by the highest frequency presented in the analog signal. In this study, the collected analog data were first low-pass filtered at 30 kHz. Thus, the hot-wire signals were sampled at 80 kHz (which is more than twice the Nyquist frequency to avoid aliasing problems) over the sampling time of 25 s, resulting in 2,000,000 samples, with a PC through a 12-bit A/D converter. Appendix C explains the procedure of selecting the sample frequency and sample number for the velocity measurement and wake survey experiments.

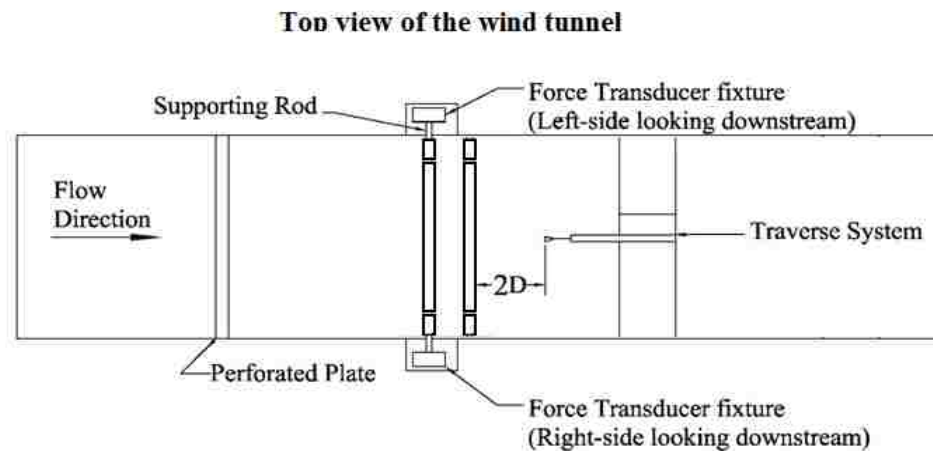


Fig. 21 Experimental set-up in the wind tunnel

3.4.1. Hot-wire calibration

For velocity calibration of probes, the Streamline automatic probe calibration system was used to establish the relationship between the voltage output from the hot-wire anemometer and the flow velocity. A calibration system plays an important role for the accuracy and the speed, with which an experiment can be accomplished. The calibration unit (Dantec 90H10) consists of a calibration module, which is simply plugged into the frame, and a flow section. The flow unit connects to compressed air supplier (6 to 8 bars) and creates a highly stable free jet of low turbulence (less than 0.2%). The air supplier is connected to an external filter which removes dust particles and oil from compressed air before it enters the flow unit (see Fig. 22(b)). To calibrate the hot-wire probe, the probe was mounted near the exit and the centre of the jet. Also, the temperature probe was connected to the frame of the hot-wire probe. The velocity calibration was performed by exposing the probe to a set of known velocities (10 different velocities in this study), U , and record the voltages, E . Then, a polynomial curve relates the voltage value and the corresponding velocity can be plotted. The system gives five coefficients, C_0 , C_1 , C_2 , C_3 , and C_4 to find correct velocity values with an error less than 1%.

$$U = C_0 + C_1E^1 + C_2E^2 + C_3E^3 + C_4E^4 \quad (7)$$

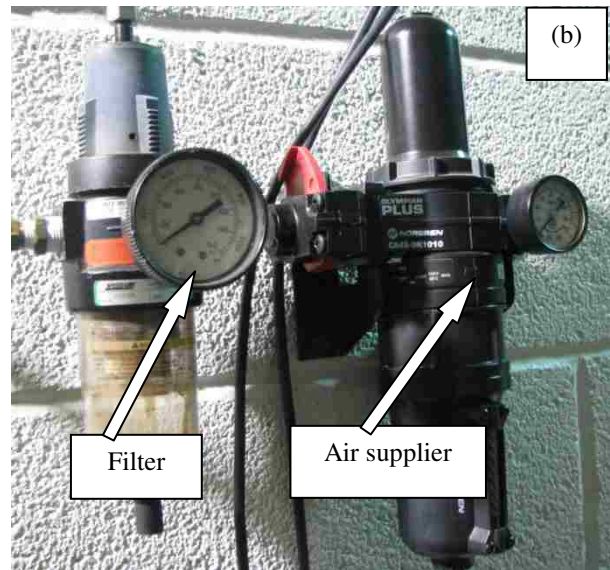


Fig. 22 Hot-wire calibration system (a) calibration unit, and (b) air supplier

3.5. Traversing mechanism

A light-duty 2D traversing system was located at the desired location downstream of the orificed perforated plate for supporting the 1D hot-wire probe and the temperature probe as shown in Fig. 23. The traversing system was supported by an aluminum frame. The horizontal and vertical traverse lengths were 558 mm and 520 mm, respectively. A computer program and two servomotors were used to control the traverse system movement in y and z directions in the wind tunnel.

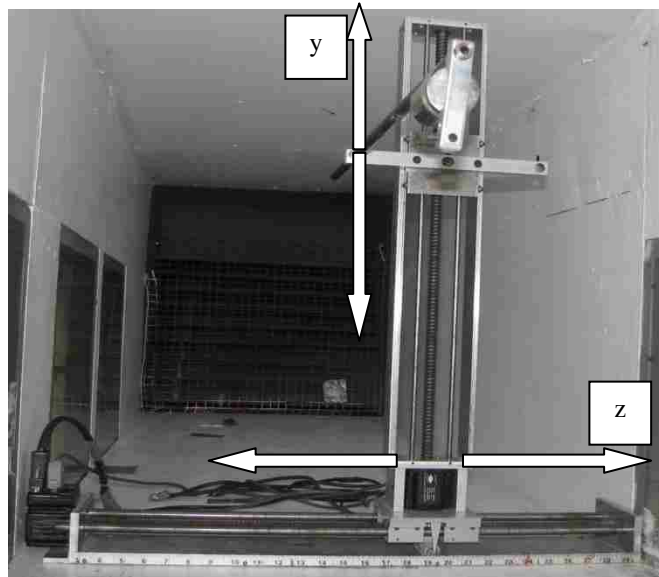


Fig. 23 The light-duty 2D traversing mechanism

CHAPTER IV

DATA ANALYSIS

4.1. Hot-wire data analysis

The time-averaged velocity (\bar{U}) is calculated via

$$\bar{U} = \sum_{i=1}^N \frac{U_i}{N} \quad (8)$$

where, U_i is the instantaneous velocity, N is the sample size. In this study, to characterize the turbulence flow along the wind tunnel, the sample size is fixed at $N = 10^7$. However, the sample size is set at $N = 2 \times 10^6$ for the wake survey.

The difference between the instantaneous velocity (U_i), and the time-averaged velocity (\bar{U}) is the instantaneous fluctuating (u). The root mean square of value for the velocity is calculated as

$$u_{\text{rms}} = \sqrt{\sum_{i=1}^N \frac{(U_i - \bar{U})^2}{N-1}} \quad (9)$$

The relative turbulence intensity (Tu) is simply

$$Tu\% = \frac{u_{\text{rms}}}{\bar{U}} \times 100 \quad (10)$$

The integral length scale is a length scale which represents a measure of the size of energy-containing eddies. According to Belmabrouk and Michard [33], by using the Taylor's frozen hypothesis (the Taylor's frozen hypothesis is practical when $u_{\text{rms}}/U_o \ll 1$ and the turbulence is close to isotropic, which are satisfied in this study) the integral length scale is estimated as

$$\Lambda = \bar{U} \times \tau_{\Lambda} \quad (11)$$

where, \bar{U} is the time-averaged velocity, and τ_{Λ} , is the integral time scale calculated

$$\tau_{\Lambda} = \int f(\tau) d\tau \quad (12)$$

Where, $f(\tau)$ is the auto-correlation function of time, calculated as

$$f(\tau) = \frac{1}{u_{rms}^2} \int u(t) - u(t - \tau) dt \quad (13)$$

The auto-correlation function $f(\tau)$ for discrete samples may be deduced as

$$f(m\Delta t) = \frac{\frac{1}{N-m} \sum_{i=1}^{N-m} (u_i u_{i+m})}{\frac{1}{N} \sum_{i=1}^N u_i^2} \quad (14)$$

where, N is the sample size, and m varies from 0 to $N-1$. The integral time scale is calculated as,

$$\tau_{\Lambda} = (\sum_{i=0}^m f(i)) \Delta t \quad (15)$$

A sample auto-correlation function versus time is plotted for the perforated plate ($d = 38.1$ mm) located at $x/d = 50$ (x is the distance between the hot-wire probe and the perforated plate) when $U_0 = 8.2$ m/s in Fig. 24. The integral time scale value represents the area under the auto-correlation function.

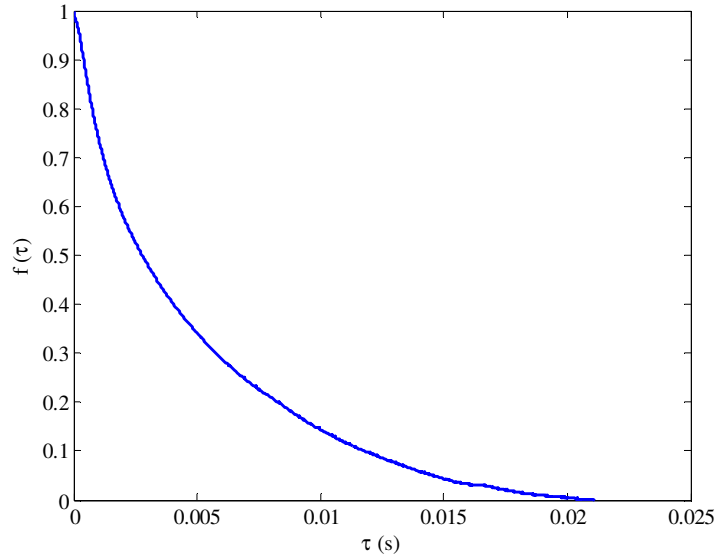


Fig. 24 Integral time scale for d38.1 plate at 50x/d and $U_0 = 8.2$ m/s

4.2. Decay of turbulence intensity downstream of the perforated plate

The free-stream velocity and integral length scale were produced by employing different perforated plates (different hole sizes) at different locations in the test section downstream of the perforated plate in the absence of any cylinders. Liu et al. [32] revealed that at downstream of the perforated plate turbulence decays in a power law method, as shown in Fig. 25. It is interesting to note that the turbulence intensity slightly depends on the free-stream velocity. However, it is a strong function of the location of the perforated plate. The turbulence intensity uncertainty was estimated to be $\pm 0.5\%$ (absolute). The Re uncertainty was calculated to be ± 800 for $Re = 6700$ and ± 170 for $Re = 12000$, see Appendix D.

4.3. Integral length scale

There are many length scales used to characterize turbulence flow, e.g. integral length scale, Taylor micro-scale, and Kolmogorov micro-scale (in decreasing order of size). The integral length scale, Λ , represents the mean size of the energy-containing eddies. In other words, the bulk of the energy is contained in the large eddies in the energy-containing range. The integral length scale is a measure of the large scale eddies within this energy-containing range. In the energy-containing range, the eddies have more inertia force. The magnitude of the integral length scale is strongly dependent on the perforated plate holes size and the spacing between them. Fig. 26 shows the integral length scale at five locations downstream of the perforated plates. The linear curve fitting was used for each velocity. Fig. 26 shows that the integral length scale is a weak function of the free-stream velocity and it is a strong function of the location of the perforated plate.

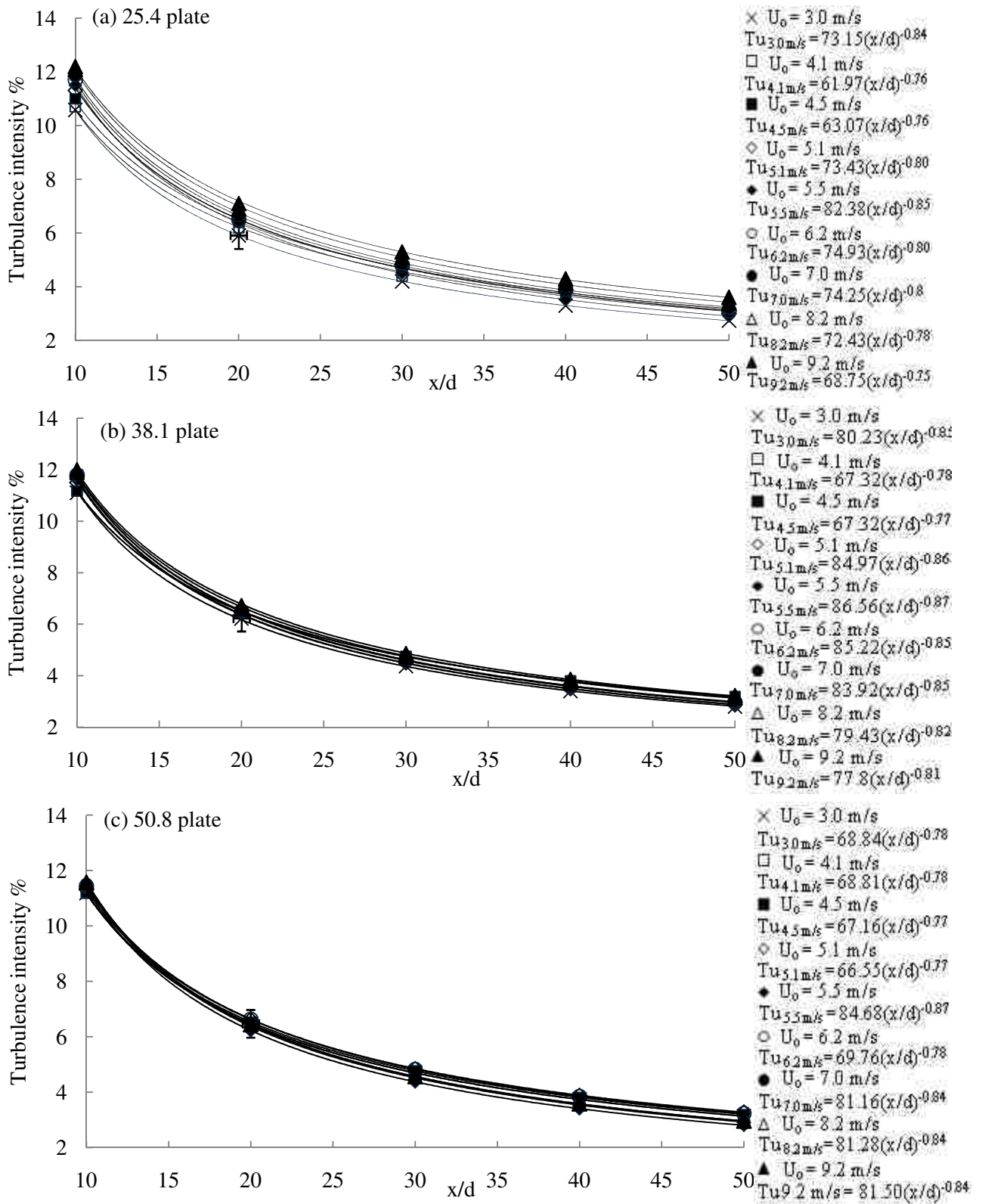


Fig. 25 Turbulence intensity downstream of: (a) d25.4 plate, (b) d38.1 plate, and (c) d50.4 plate

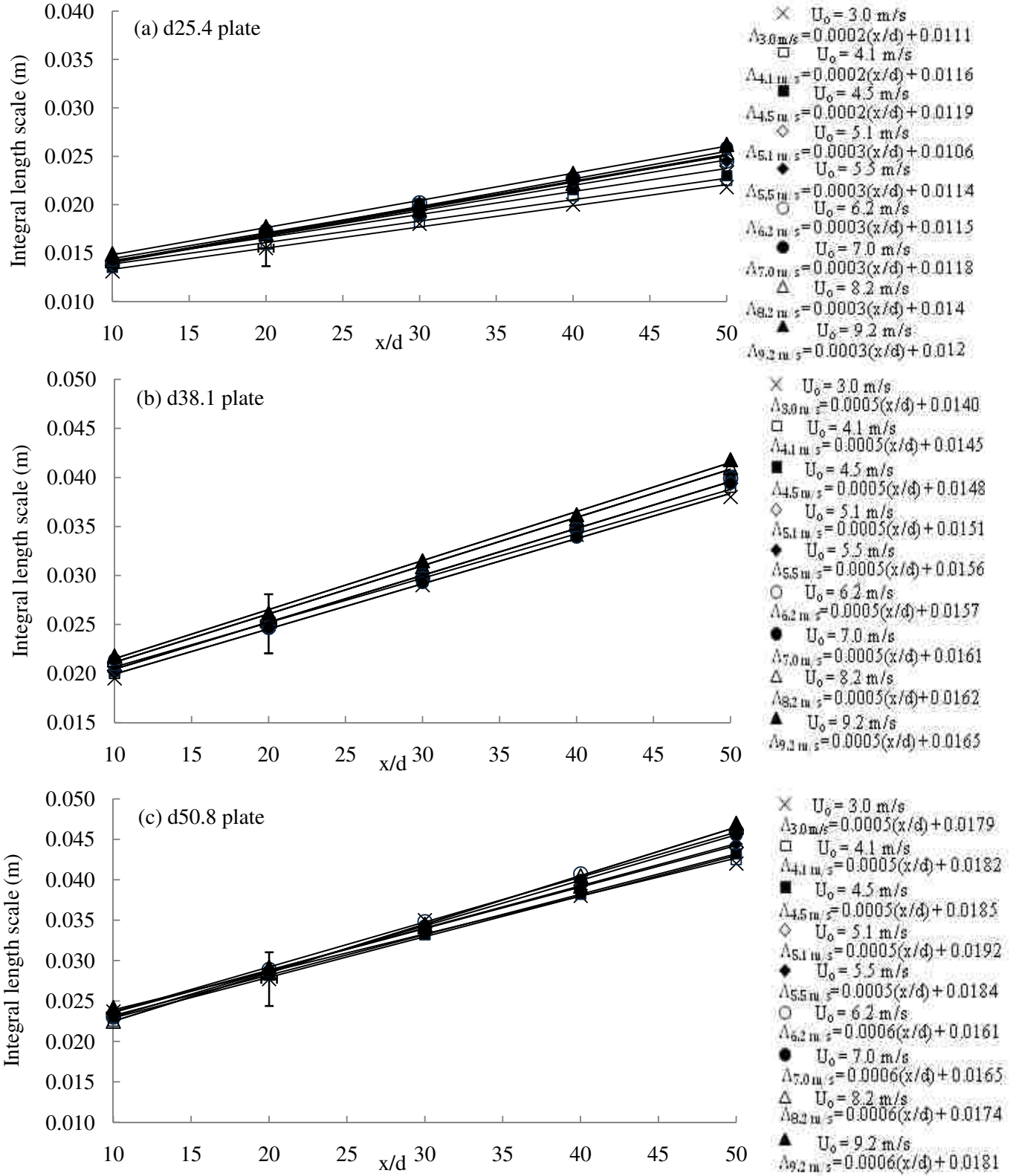


Fig. 26 Integral length scale downstream of: (a) d25.4 plate, (b) d38.1 plate, and (c) d50.4 plate

CHAPTER V

RESULT AND DISCUSSION

The pressure distribution around a single and two staggered circular cylinders were measured by using a manometer (Dwyer series 475 mark III) in smooth flow. Then, the lift and drag coefficients, C_D and C_L , were obtained by integrating the pressure distributions around the cylinder. Also, the dynamic drag and lift coefficients, C_D and C_L , of a single cylinder and two staggered cylinders were measured by using two load cells (ATI Gamma type) supporting upstream or downstream cylinder in each test. Then, the time-averaged results were compared with the pressure measurement results in smooth flow. Also, the stream-wise velocity, turbulence intensity, and root mean square of velocity profiles at the wake of a single and the downstream cylinder of two staggered cylinders were measured in smooth flow ($Tu \lesssim 0.5\%$), as the basis of comparison and discussion for Reynolds number, turbulence intensity, and integral length scale effects in turbulent flow. The power spectra density (PSD) in the wake of a single cylinder and the downstream cylinder in staggered arrangement were surveyed in smooth flow at $6.7 \times 10^3 \lesssim Re \lesssim 1.2 \times 10^4$. The main reason for performing tests in the smooth flow is to compare the results obtained here with those in the literature. This comparison shows how the wind tunnel and the test model perform. And, together with other studies, it gives an indication of the validity of the whole set of obtained experimental results. In other words, the experimental results in smooth flow serve as a base for experimental results in turbulence flow.

5.1. Circular cylinders in smooth flow

In the present investigation, a single and two staggered circular cylinders ($L/D = 4$, and $T/D = 1$) of equal diameter ($D = 25.4$ mm) have been tested in smooth flow ($Tu \lesssim 0.5\%$). Drag and lift coefficients of a single cylinder and two staggered cylinders have been measured for $6.7 \times 10^3 \lesssim Re \lesssim 1.2 \times 10^4$ using the pressure and dynamic force measurement techniques. For each cylinder, the blockage ratio is less than 5%.

For a single cylinder, the mean drag coefficients, using pressure and dynamic force measurement techniques, are approximately 1.0 for $6.7 \times 10^3 \lesssim Re \lesssim 1.2 \times 10^4$, as shown in Fig. 27(a). This value of drag coefficient is in a good agreement with Lee et al [34] who investigated experimentally the flow over a smooth and v-grooved circular cylinders in cross flow in the range of $2.5 \times 10^3 \lesssim Re \lesssim 3.8 \times 10^4$. However, their C_D values for the smooth cylinder were 1.1 to 1.2. This value of the drag coefficient for a single cylinder is within the values in the literature ($\cong 1.0 - 1.3$), though somewhat lower than the well-accepted value of 1.2 in the subcritical Reynolds regime [2, 3, and 35]. Also, this value of drag coefficient is in agreement with Yeboah et al. [36] who found that in the range of $1.4 \times 10^3 \lesssim Re \lesssim 4.8 \times 10^4$, the C_D values were near 1.0 in smooth flow. The maximum uncertainty in the Re is estimated to be 800 and it corresponded to the lowest value of Re . Also, the maximum uncertainty in the drag coefficient occurs at the lowest velocity (lowest Re) and it is estimated to be 0.13 and 0.03 in force and pressure measurement techniques, respectively, see Appendix D. The typical error bars (based on the dynamic force measurement technique) corresponding to the lowest value of Re are included in Fig. 27(a). Since the uncertainty in force measurement is higher than the uncertainty in pressure measurement, the time-averaged drag and lift coefficients

obtained by pressure measurement are more reliable. Thus, in this study, these time-averaged drag and lift coefficients are to be mainly based on the pressure measurement method.

By using the pressure distribution around a cylinder (Fig. 27(b)) and integrating it around the circumference of the cylinder, the drag and lift coefficients were obtained. In addition, because the pressure readings were at 22.5° increments around the circumference of the cylinder, to have more accurate drag and lift coefficients, the Spline interpolation was applied on pressure distribution curves at 5° increments in MatLab. The results show that the mean drag coefficients, C_D , are near 1.0 as shown in Fig. 27(a). As expected, mean lift coefficients, C_L , are zero for a single circular cylinder as shown in Fig. 27(a). In conclusion, the values of time-averaged drag and lift coefficients for a single cylinder obtained by the load cells corroborate those obtained from the pressure distribution. Since the uncertainty in the time-averaged C_D and C_L obtained by the load cell (0.13) is higher than the uncertainty in the pressure based measurement (0.03), the time-averaged drag and lift coefficients obtained by pressure measurement are more reliable.

The pressure distribution around a single cylinder for three different Reynolds numbers (6700, 9200, 12000) in smooth flow ($Tu \lesssim 0.5\%$) are shown in Fig. 27(b). It depicts the pressure distributions on both side of the cylinder are quite symmetrical and show typical laminar separation at about at $\theta = 80^\circ$ and 280° [2]. It was found that, the Reynolds number effect is negligible on the drag and pressure coefficients of a single cylinder in smooth flow in $6.7 \times 10^3 \lesssim Re \lesssim 1.2 \times 10^4$, as is expected. It is interesting to note that most pressure measurements around the cylinder were negative. As the flow

moves around the cylinder, it accelerates, and according to Bernoulli's principle, the pressure decreases. Thus, negative pressure was measured.

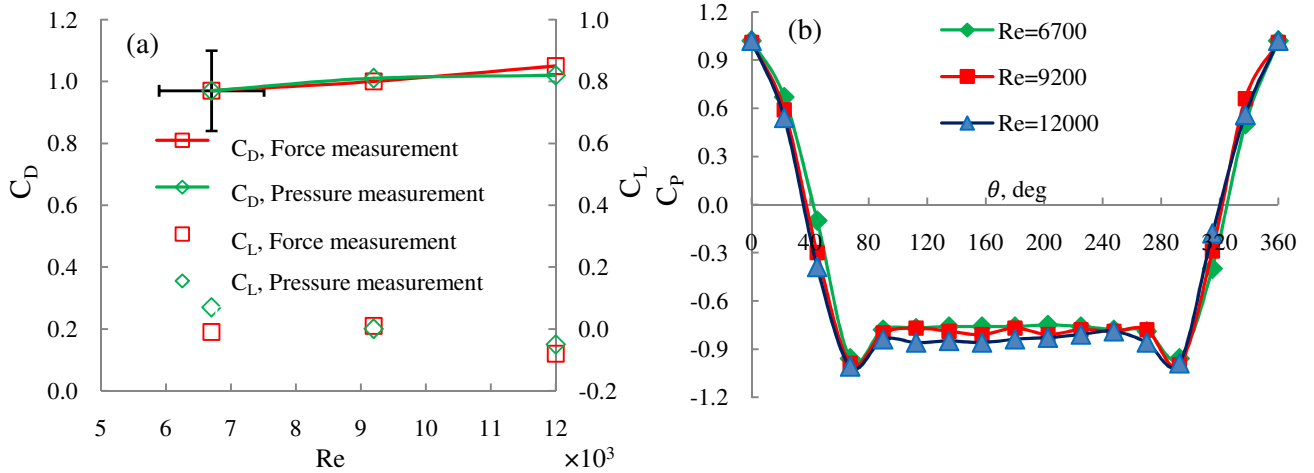


Fig. 27 Single cylinder in smooth flow (a) drag and lift coefficients, and (b) pressure distributions around a cylinder, \square signifies force measurement, \diamond denotes pressure measurement, error bars are based on the force measurement technique.

To better understand the mechanism, the wake structure of the single cylinder is surveyed using a single normal hot-wire of DISA type 55P11. For the single cylinder in smooth flow ($Tu \lesssim 0.5\%$), the wake profiles of the normalized stream-wise mean velocity (\bar{U}/U_o , where \bar{U} is the time-averaged local velocity, and U_o is the free-stream velocity), turbulence intensity (u_{rms}/\bar{U} , where u_{rms} is a root mean square of velocity, and \bar{U} is a time-averaged local velocity), and normalized root mean square of velocity (u_{rms}/U_o) are measured by traversing a hot-wire probe using 2D traverse system over the range $-3 \lesssim y/D \lesssim 3$ with an interval of $\Delta y = 2.5 \times 10^{-3}$ m for $6.7 \times 10^3 \lesssim Re \lesssim 1.2 \times 10^4$. Figure 28(a, b, c) shows the profiles of the normalized stream-wise mean velocity, the turbulence intensity, and normalized root mean square of velocity in term of y/D . The measurements

occurred across the wake at $X/D = 2$ for Re of 6700, 9200, and 12000 for a single cylinder in smooth flow ($Tu \lesssim 0.5\%$). For a single cylinder, when Re value increases from 6700 to 12000 the wake width does not significantly appear to change but the minimum velocity increases from 0.4 to 0.5. It is interesting to note that the turbulence intensity and root mean square of velocity profiles have two distinct peaks in the wake region, see Fig. 28(b, c). In general, large vortices shed from a cylinder entrain the inviscid free-stream flow into the wake region, resulting in double peaks of turbulence intensity [37], see Fig. 29. Also, two peaks are observed in root mean square of velocity profile in the outer region.

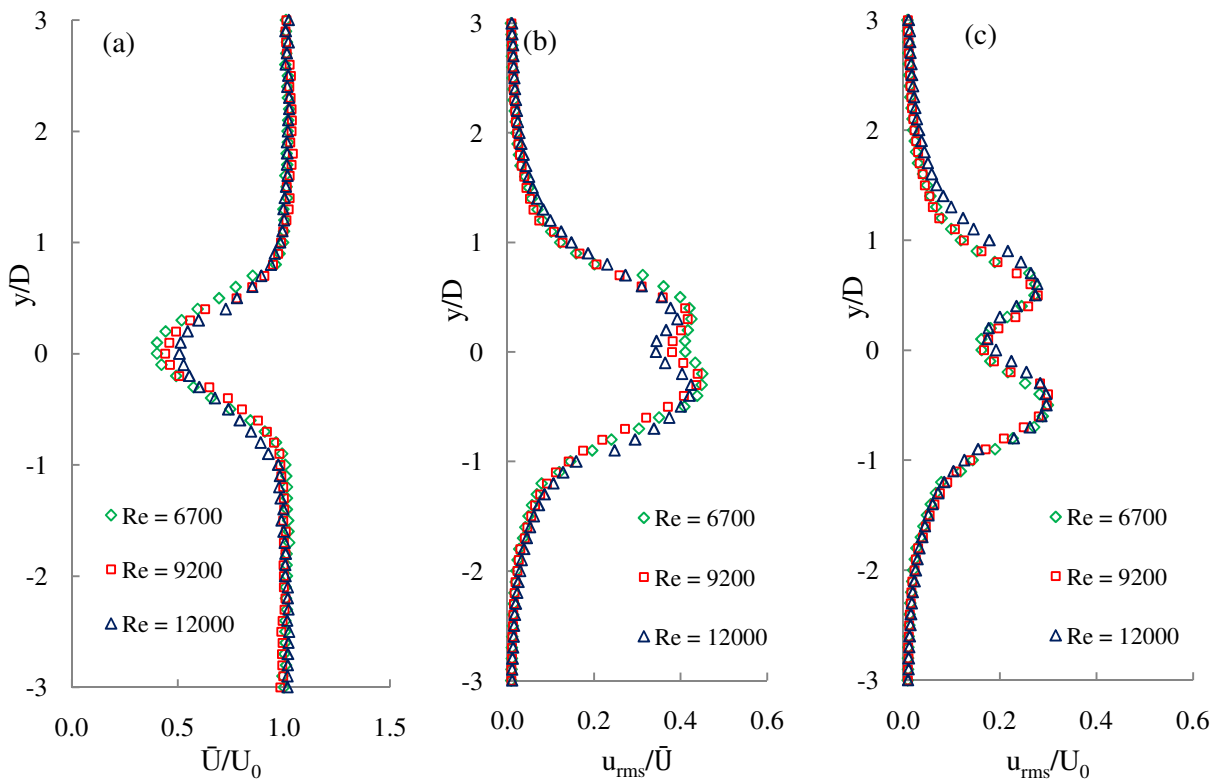


Fig. 28 Stream-wise mean velocity, turbulent intensity, and root mean square of velocity profiles for a single cylinder in smooth flow (a) mean velocity, (b) turbulence intensity, and (c) root mean square of velocity.

To better understand the flow field around a single cylinder the behaviour and appearance of the power spectra density (PSD) would be helpful. Figure 30 shows the power spectra density (PSD) using a single normal hot-wire (DISA type 55P11) for a single cylinder in smooth flow ($Tu \lesssim 0.5\%$). The power spectra density (PSD) distributions are measured at multiple vertical locations across the wake at $X/D = 2$ when $6.7 \times 10^3 \lesssim Re \lesssim 1.2 \times 10^4$. Also, the power spectra density (PSD) is plotted based on the dynamic data of the load cell attached to the cylinder. The measurements of shedding frequency are presented non-dimensionally in the form of a Strouhal number, $St = fD/U_o$ (where f is a frequency, D is the cylinder diameter, and U_o is the free-stream velocity). For a single cylinder in smooth flow ($Tu \lesssim 0.5\%$) in $6.7 \times 10^3 \lesssim Re \lesssim 1.2 \times 10^4$, the Strouhal number value remains approximately constant at 0.21. The harmonic frequencies are seen at $St = 0.42$. In this range of Re , at any vertical location across the wake, a prominent peak in PSD is observed. It means that there is regular vortex shedding from the surface of the cylinder. At the locations of the shear layers vortex shedding boundaries ($y/D = 1.5$, and -1.5 , see Fig. 29) the strongest peaks in PSD are detected, see Fig. 30. Over the Re range of $6.7 \times 10^3 \lesssim Re \lesssim 1.2 \times 10^4$, the dynamic data of the load cell shows a peak at $St = 0.21$. When $6.7 \times 10^3 \lesssim Re \lesssim 1.2 \times 10^4$, the Strouhal number remains constant at $St = 0.21$ for a single cylinder. Zdravkovich [2] indicated that the linear increase in the free-stream velocity (consequently rise in Re) causes a linear increase in the eddy shedding frequency, thus, the Strouhal number remains constant in the subcritical range of Re .

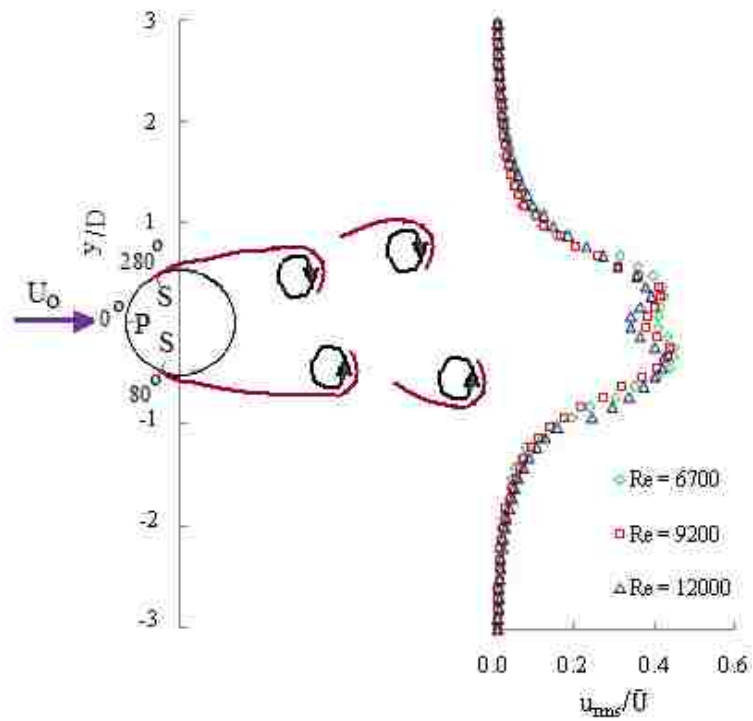
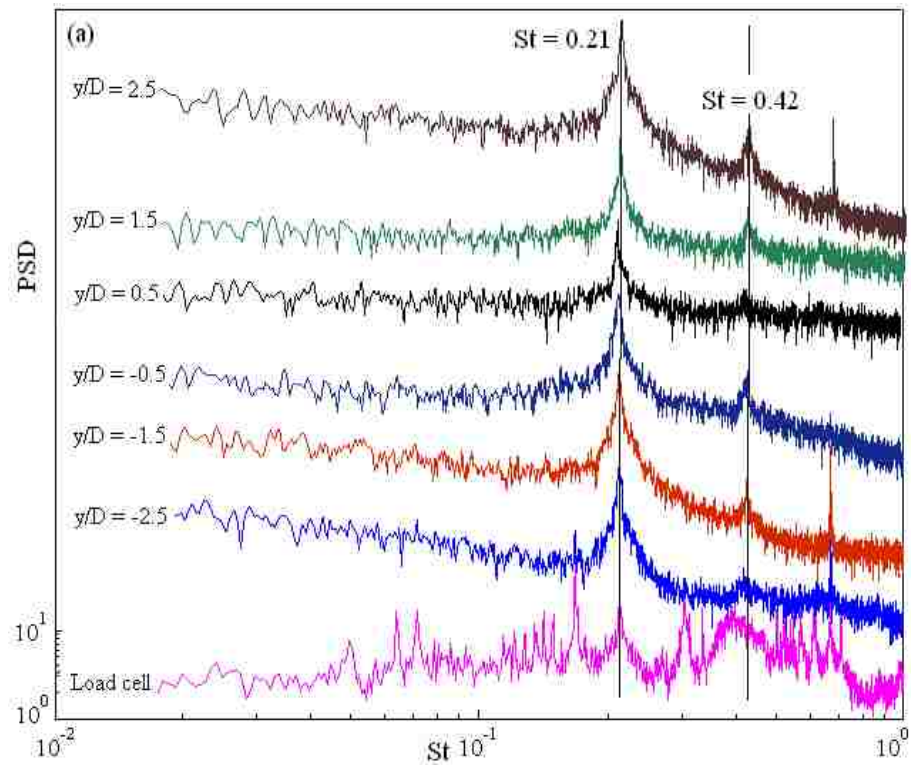


Fig. 29 Flow pattern and turbulence intensity profile for a single cylinder in smooth flow, “S” signifies the separation point, and “P” denotes the stagnation point



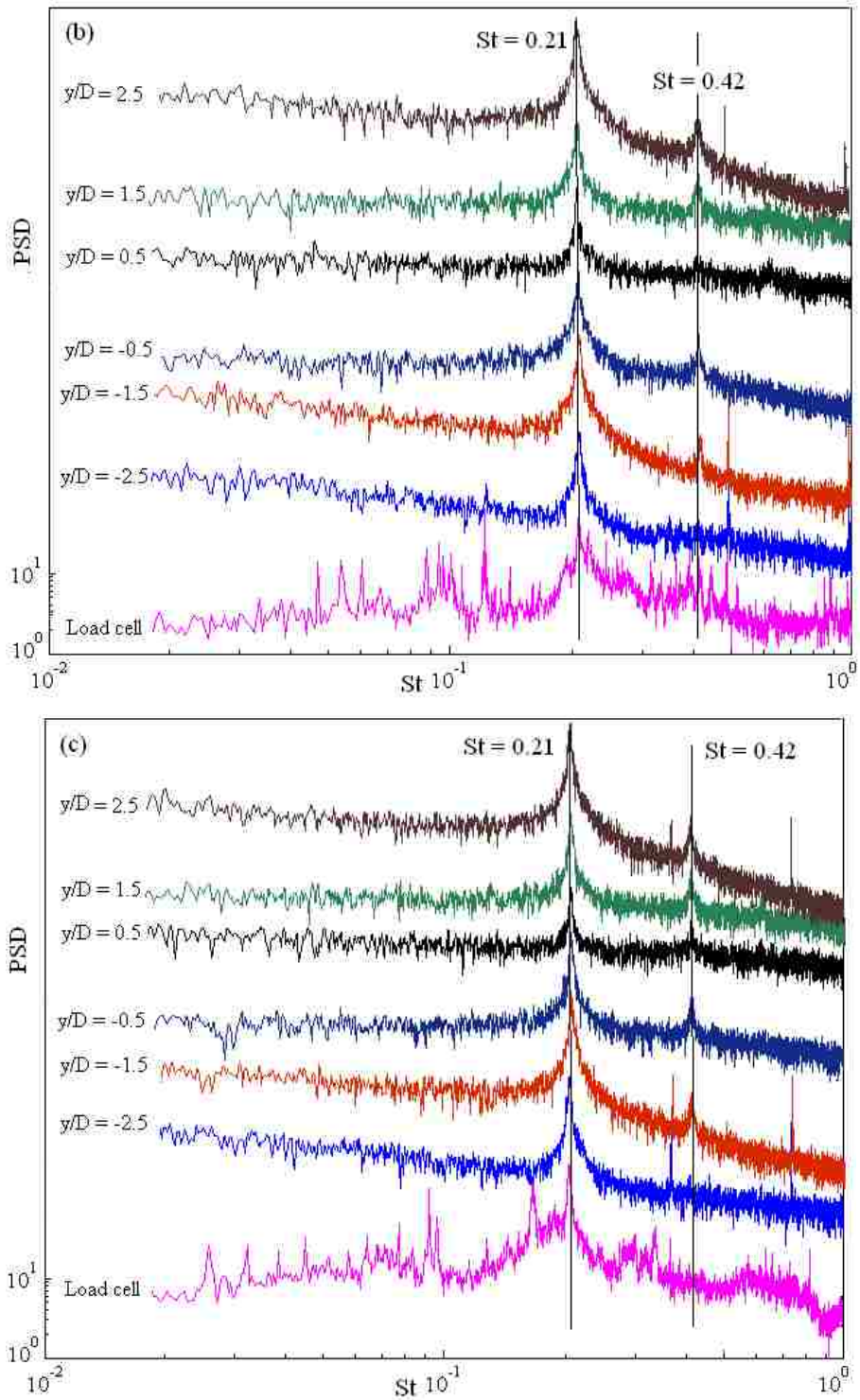


Fig. 30 PSD at different vertical locations across the wake of a single cylinder in smooth flow ($Tu \lesssim 0.5\%$) (a) $Re = 6700$, (b) $Re = 9200$, and (c) $Re = 12000$, the vertical scale is arbitrary, but the same scale is used for all spectra.

When two circular cylinders are subjected to a steady flow, the resulting forces and flow pattern in the wake may be very different from those found on a single cylinder at the same Reynolds number, due to the interactions between the shear layers, and vortices. The staggered configuration is the most general arrangement of two circular cylinders. For the upstream cylinder in staggered arrangement, the pressure and dynamic force measurement results indicate that the value of drag coefficient obtained in this study remains close to the single cylinder value when $6.7 \times 10^3 \lesssim Re \lesssim 1.2 \times 10^4$, see Fig. 31(a). The drag coefficients are marginally lower (90-95%) than the single cylinder drag coefficient value, as shown in Fig. 31(a). Accounting for the maximum possible error of 0.13 in C_D by using the dynamic force measurement technique, these values are similar to C_D values for a single cylinder. Also, considering the maximum possible error of 0.03 in C_D using pressure distribution results, these values are marginally lower than those experienced by a single cylinder. These results are in agreement with Sumner et al. [24] who confirmed that the drag coefficient for the upstream cylinder of two widely spaced staggered cylinders remains close to the single cylinder drag coefficient value. For two staggered cylinders, lift coefficients of the upstream cylinder have been measured for $6.7 \times 10^3 \lesssim Re \lesssim 1.2 \times 10^4$ using the pressure and dynamic force measurement techniques. Both techniques show the lift coefficients attain negative value, see Fig. 31(a). This behaviour of the upstream cylinder shows that this cylinder experienced a small repulsive force in the range of $6.7 \times 10^3 \lesssim Re \lesssim 1.2 \times 10^4$. However, Sumner et al. [24] indicated that the lift coefficient of the upstream cylinder is nearly zero for two widely spaced circular cylinders.

For the downstream cylinder in staggered arrangement the drag coefficient values are $0.6 < C_D < 0.8$ in smooth flow by using pressure and dynamic force measurement techniques, see Fig. 31(b). Zdravkovich [20] indicated that for the downstream cylinder in staggered arrangement ($L/D = 4$, and $T/D = 1$) the drag coefficient is $0.6 \lesssim C_D \lesssim 0.8$ for subcritical range of Re , see Fig. 32(a). Note that the drag coefficient for downstream cylinder is lower than the one for upstream cylinder because the downstream cylinder is in the vicinity of the wake of the upstream cylinder. The typical error bars (based on the dynamic force measurement technique) corresponding to the lowest value of Re are included in Fig. 31(a, b).

Also, the lift coefficients for downstream cylinder have been measured by using both pressure and dynamic force measurement techniques. These measurement results show that the lift coefficient remains constant roughly at -0.5 in the range of $6.7 \times 10^3 \lesssim Re \lesssim 1.2 \times 10^4$ in the smooth flow, see Fig. 31(b). This is in the good agreement with Zdravkovich [20] who confirmed that for the downstream cylinder in staggered arrangement ($L/D = 4$, and $T/D = 1$) the lift coefficient is $-0.6 \lesssim C_L \lesssim -0.4$ for subcritical range of Re , see Fig 32(b).

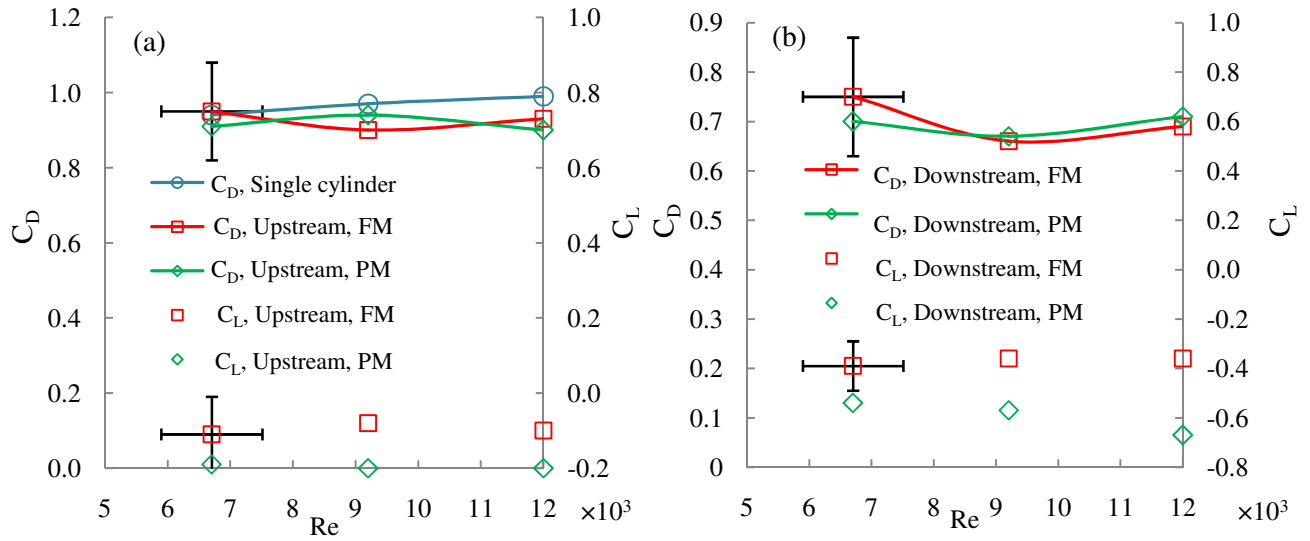


Fig. 31 Drag and lift coefficients of two staggered cylinders in smooth flow (a) upstream cylinder, and (b) downstream cylinder, FM signifies the force measurement, PM denotes pressure measurement, error bars are based on the force measurement technique.

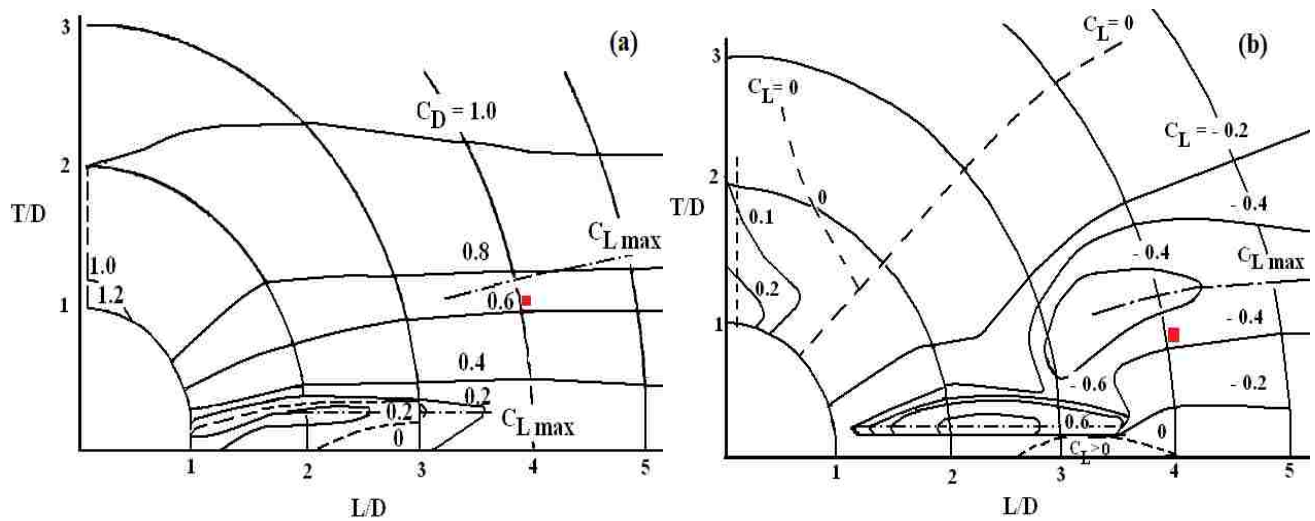


Fig. 32 Force coefficient map for the downstream cylinder of two staggered cylinders in smooth flow in subcritical Re (a) drag coefficient, and (b) lift coefficient, ■ signifies the current study, after Zdravkovich [20].

The pressure distributions around the upstream cylinder in staggered arrangement for Re 6700, 9200, and 12000 in smooth flow are shown in Fig. 33(a). The pressure distributions around the upstream cylinder in this arrangement are similar to that around a single circular cylinder, except that they are slightly shifted and not symmetric anymore. There is a breaking of a symmetric distribution around $\theta = 340^\circ$. Figure 33(a) illustrated that at Re = 6700, 9200, and 12000, the shear layer at the outer side of the upstream cylinder separated at $\theta = 80^\circ$ (the same as that of a single cylinder), while, the separation point at the inner side of the upstream cylinder occurs at $\theta = 250^\circ$. In compare with a shear layer separation angle for a single cylinder in smooth flow ($\theta = 280^\circ$), the shear layer separated from the inner side of the upstream cylinder is rather far back. As one can see in Fig. 33(a), over the range of $6.7 \times 10^3 \lesssim \text{Re} \lesssim 1.2 \times 10^4$, the pressure distribution around the upstream cylinder does not appear to be sensitive to the changes in the Reynolds number.

The pressure distributions around the downstream cylinder are shown in Fig. 33(b). At $\theta = 0^\circ$ of the downstream cylinder, the C_p values are less than 1.0 ($C_p \cong 0.6$) as shown in Fig. 33(b). When $C_p \neq 1.0$, means that there is no stagnation point at that point for the downstream cylinder. Also, it denotes that the downstream cylinder is significantly more affected by the presence of the upstream cylinder, than the upstream cylinder by the presence of the downstream cylinder. The C_p values at $\theta = 0^\circ$ for the downstream cylinder (C_p values are less than 1.0) prove that the downstream cylinder is in the wake of the upstream cylinder. This kind of flow pattern for $L/D = 4$ and $T/D = 1$ ($P/D \cong 4$) could be classified as wake interference according to Zdravkovich [20], see Fig. 6. According to Gu and Sun's [21] classification, there is a wake interference in this

study, because there is no steady stagnation point ($C_P \neq 1.0$) for the downstream cylinder at $\theta = 0^\circ$, see Fig. 8(a). Based on Sumner et al. [22], this type of flow pattern could be classified as the widely spaced category ($P/D > 2.5$, where P is the gap between two cylinders), see Fig. 9(c). At $50^\circ \lesssim \theta \lesssim 90^\circ$, C_P values are constant and have a negative value of -1.0. The locations of the separation points of the downstream cylinder are at around $\theta = 50^\circ$ and 250° . Figures 33(b), and 35 show a shift in the stagnation point ($C_P = 1.0$) in the direction away from the side of the upstream wake [38, 21]. In other words, there is a single peak at $\theta = 340^\circ$ corresponding to the stagnation point (C_P value is 1.0).

To better understand the mechanism, the wake structure of the downstream cylinder is surveyed using a single normal hot-wire of DISA type 55P11. For two staggered cylinders in smooth flow ($Tu \lesssim 0.5\%$), the profiles of the normalized stream-wise mean velocity, turbulence intensity, and root mean square of velocity are measured by traversing a hot-wire probe using 2D traverse system at $X/D = 2$ (see Fig. 21), over the range $-4 \lesssim y/D \lesssim 4$ with an interval of $\Delta y = 2.5 \times 10^{-3}$ m for $6.7 \times 10^3 \lesssim Re \lesssim 1.2 \times 10^4$, see Fig. 34(a, b, c).

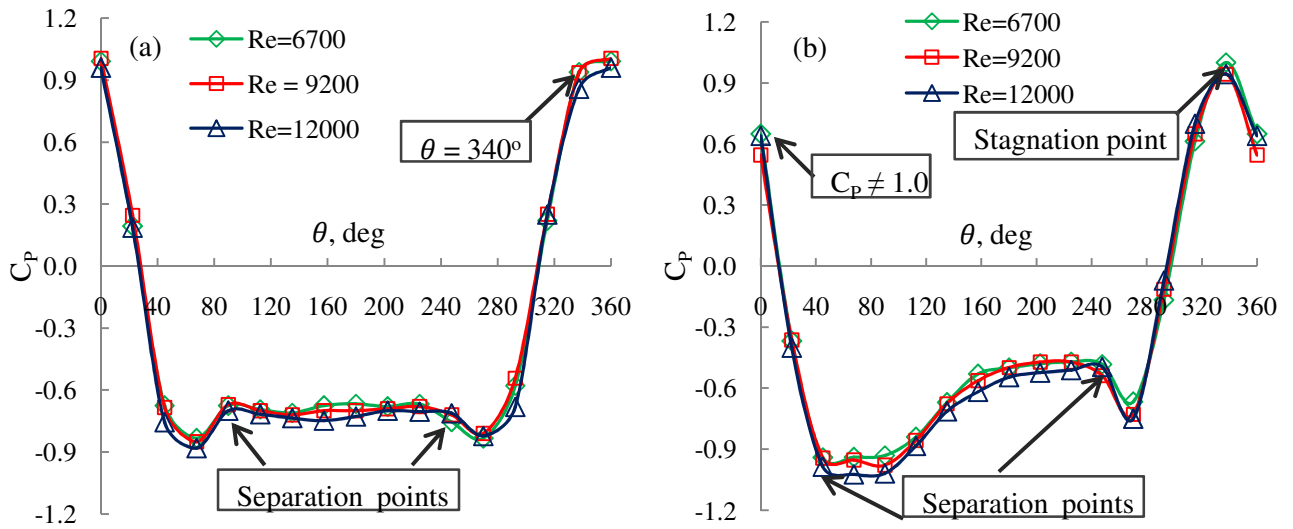


Fig. 33 Pressure distribution of two staggered cylinders in smooth flow (a) around the upstream cylinder, and (b) around the downstream cylinder.

The normalized stream-wise mean velocity profile shows a wider wake for the downstream cylinder ($-1 \lesssim y/D \lesssim 2$) compare with a single cylinder ($-1 \lesssim y/D \lesssim 1$), see Fig. 34(a). It is interesting to note that when there are two cylinders in smooth flow, the vortices are suppressed and broken into smaller eddies. Then, the free-stream is entrained into the wake region only to a small extent, so, the momentum transfer from the free-stream to the wake region is insufficient to recover the velocity deficit. Thus, the turbulence intensity profiles of two cylinders have only one peak in the wake region, see Fig. 34(b), and Fig. 35. However, the turbulence intensity profiles of a single cylinder have two peaks in the wake region (regular vortex shedding). The root mean square of velocity profiles of two circular cylinders have two distinct peaks, see Fig. 34(c). The interaction between the inner shear layer of the upstream cylinder and the outer shear

layer of the downstream cylinder causes the peak of the root mean square of velocity in the upper side of the wake is weaker than the one at the lower side of the wake.

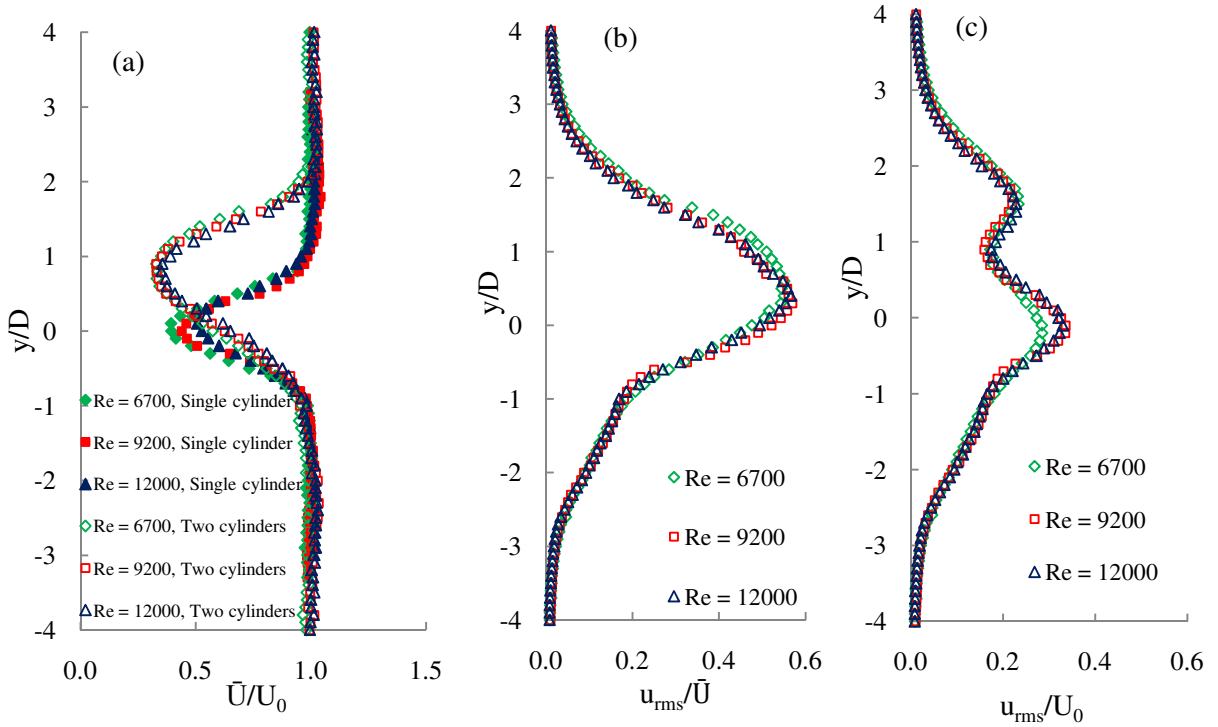


Fig. 34 Stream-wise mean velocity, turbulent intensity, and root mean square of velocity profiles for two cylinders in smooth flow (a) mean velocity, (b) turbulence intensity, and (c) root mean square of velocity.

The behaviour and appearance of the power spectra density (PSD), and the Strouhal number value would be helpful in understanding the physical relationship between the data and the flow field. Figure 36 presents that for two staggered cylinders in smooth flow ($Tu \lesssim 0.5\%$), the Strouhal number remains constant at $St = 0.19$ in $6.7 \times 10^3 \lesssim Re \lesssim 1.2 \times 10^4$. The value of Strouhal number is ($St = 0.19$) less than the $St = 0.21$ for a single cylinder, and the harmonic frequency is seen at $St = 0.38$.

At $y/D = 1.5$, the vortex shedding peak appears to be absent due to the interaction between the inner shear layer of the upstream cylinder, and the outer shear layer of the downstream cylinder, see Fig. 35. This phenomenon was previously reported by Sumner et al. [22] who explained that the weakening of the vortex shedding peak may be associated to the impingement of the vortices shed from the upstream cylinder onto the downstream cylinder and the interaction of two vortex streets.. A clear and distinct peak at PSD shows the existence of a dominant vortex structure due to regular vortex shedding. Over the Re range of $6.7 \times 10^3 \lesssim Re \lesssim 1.2 \times 10^4$, the dynamic data of the load cell shows an extremely distinct peak at $St = 0.19$. The comparison between the power spectra density at any location across the wake (using a single normal hot-wire DISA type 55P11) and the power spectra from the load cells shows that the low frequency excitation (peaks in the PSD of the load cell) is not vortex shedding. In this study, over the narrow range of Re ($6.7 \times 10^3 \lesssim Re \lesssim 1.2 \times 10^4$), the Strouhal number remains constant at $St = 0.19$ for two staggered cylinder.

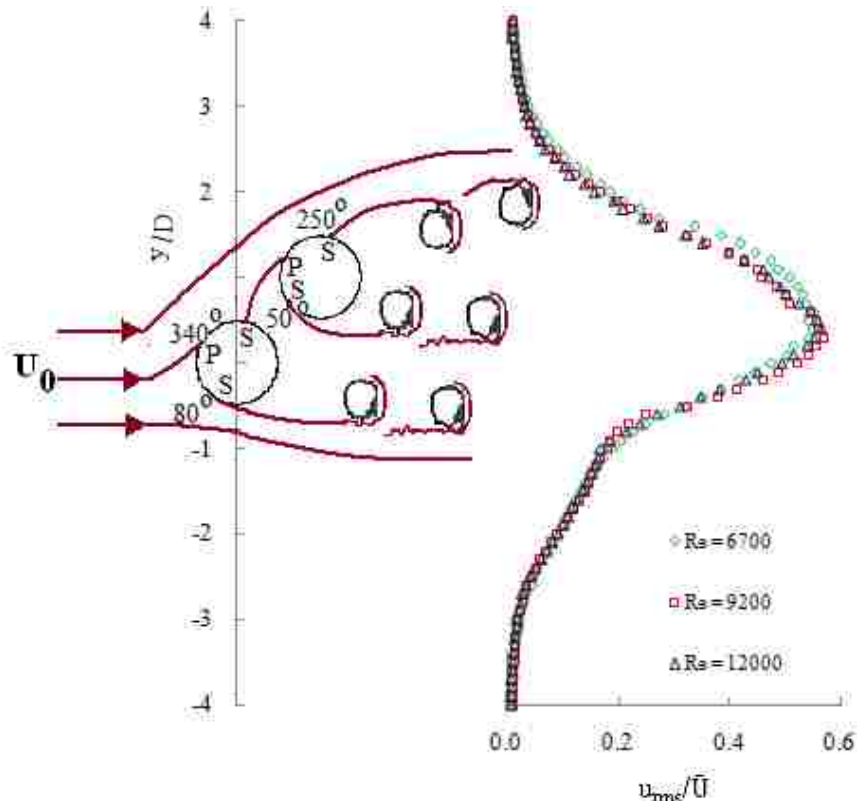
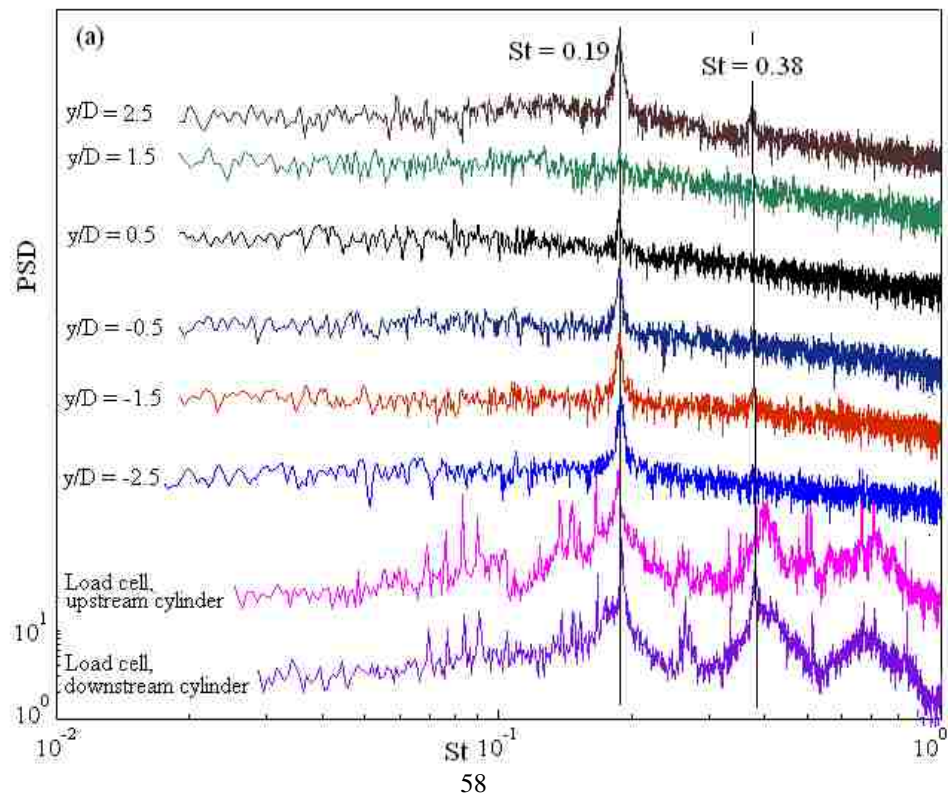


Fig. 35 Flow pattern and turbulence intensity profile for two cylinders in smooth flow,

“S” signifies the separation point, and “P” denotes the stagnation point.



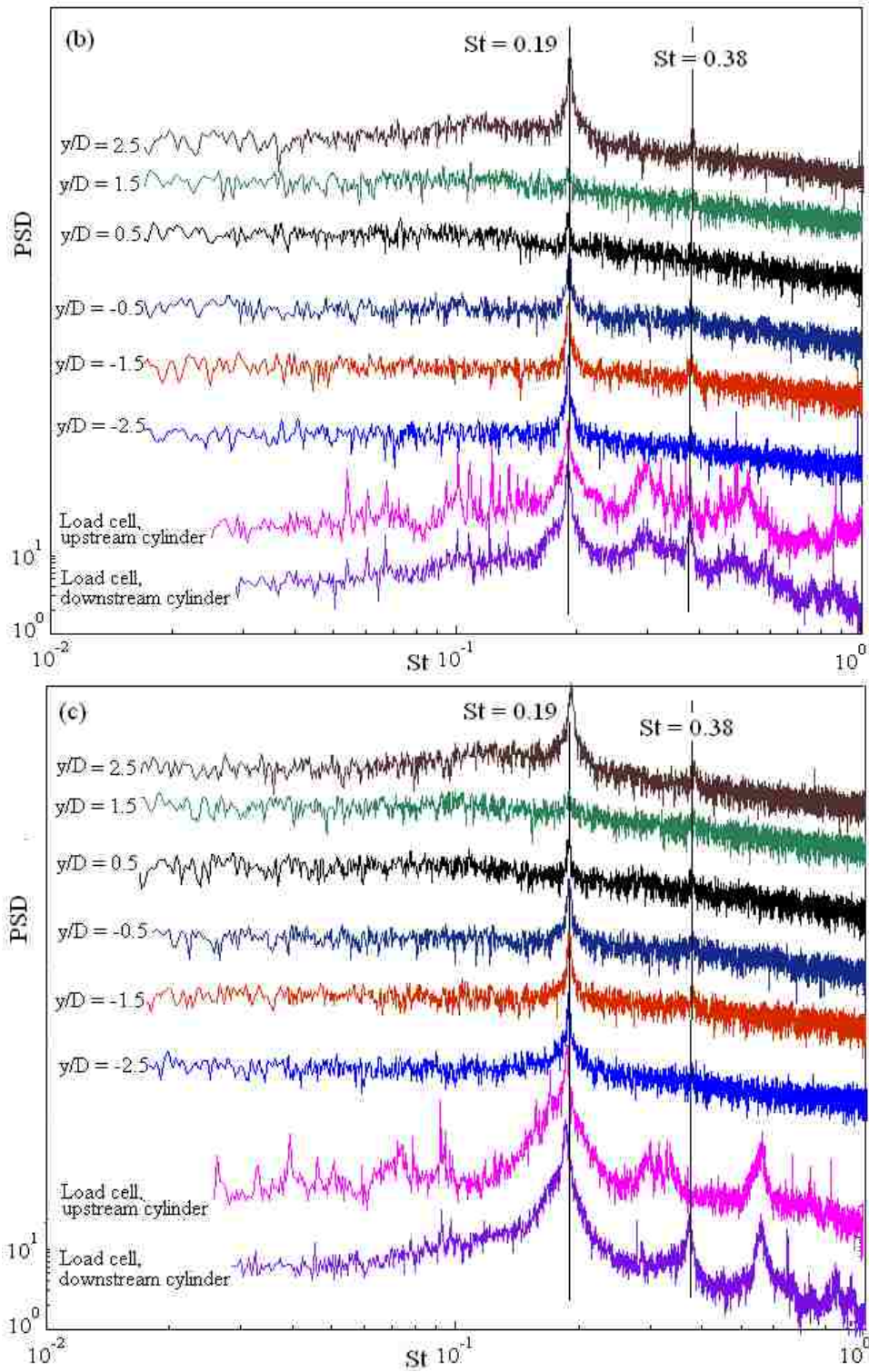


Fig. 36 PSD at different vertical locations across the wake for two cylinders in smooth flow ($Tu \lesssim 0.5\%$) (a) $Re = 6700$, (b) $Re = 9200$, (c) $Re = 12000$, the vertical scale is arbitrary, but the same scale is used for all spectra.

5.2. Comprehensive view of the effect of the turbulence on two staggered cylinders

This section will discuss the effect of turbulence intensity ($0.5 \lesssim Tu \lesssim 10\%$) on the drag and lift coefficients of the upstream and downstream cylinders when $0.56 \lesssim \Lambda/D \lesssim 1.28$ for $Re = 6700, 9200, \text{ and } 12000$. Since the uncertainty in dynamic force measurement (0.25, the maximum uncertainty for drag and lift coefficients associated with the minimum free-stream velocity, $U_o = 3.0 \text{ m/s}$, in this study) is higher than the uncertainty in pressure measurement (0.03), the drag and lift coefficients obtained by pressure measurement are considered more reliable. Thus, in this section, the results are to be mainly based on the pressure measurement method. Appendix E includes the dynamic force measurement results, which are in an agreement with the pressure measurement results. The turbulence intensity effects on the upstream and downstream can be inspected from the pressure measurement results, which can be found in Fig. 37 and Fig. 38.

For the upstream cylinder, the behaviour of the drag coefficient with turbulence intensity appears to be similar for the three Reynolds values ($Re = 6700, 9200, \text{ and } 12000$) considered, see Fig. 37. When $\Lambda/D = 0.56, \text{ and } 0.96$ ($\Lambda/D \lesssim 1$), the value of C_D at $Tu = 4\%$ is lower than that in smooth flow ($Tu = 0.5\%$), except at $Re = 12000$, the drag coefficients at smooth flow ($Tu = 0.5\%$) and $Tu = 4\%$ have the same value. When $\Lambda/D = 0.56, \text{ and } 0.96$ ($\Lambda/D \lesssim 1$), with increasing turbulence intensity from $Tu = 4\%$ (or 3%) to $Tu = 7\%$, the drag coefficient of the upstream cylinder increases, see Fig. 37. The changes in the pressure distributions associated with this increase in C_D with Tu are

illustrated in Fig. 39(a). Figure 37 shows that when $\Lambda/D = 1.28$, the value of C_D at $Tu = 4\%$ (or 3%) is higher than that in smooth flow ($Tu = 0.5\%$). This behaviour of the drag coefficient of the upstream cylinder is in a good agreement with Liu [27] who found that the C_D of the upstream cylinder in staggered arrangement ($\alpha = 11^\circ$) in smooth flow is less than that in turbulence flow at $Re = 4.2 \times 10^4$ when $Tu = 5.6\%$, and $1 \lesssim \Lambda/D \lesssim 1.36$. The large integral length scale ($\Lambda/D = 1.28$) results a higher drag coefficient comparing to the one with $\Lambda/D = 0.56$ and 0.96 ($\Lambda/D \lesssim 1$). This difference diminishes when Tu increases beyond 7% . The drag coefficients converge to the same level which centred around 1.0 , which is the value for the drag coefficient of the single cylinder in smooth flow. This behaviour of the drag coefficient of the upstream cylinder is in agreement with Price [29] and Liu et al. [25]. Price [29] showed that for two circular cylinders in a staggered arrangement, $P/D = 2.2$, the drag coefficient value of the upstream cylinder is 1.0 when $Re = 3.5 \times 10^4$ and $Tu = 11\%$. Liu et al. [25] tested groups of two, three, and four circular cylinders arranged in-line, when $Tu = 5.6\%$ over a Re range of 2.7×10^4 to 8.6×10^4 . The integral length scale, Λ/D , was varied from 0.67 to 1.01 . For two identical circular cylinders, it was found that the upstream cylinder behaved like a single cylinder. In Fig. 37(b) the drag coefficient appears to be slightly lower with $\Lambda/D = 1.28$ and this is not obvious in the Fig. 37(a, c).

For the upstream cylinder, the value of the lift coefficient is negative, meaning the upstream cylinder tends to be repelled away from the downstream cylinder. Figure 37 shows that when $\Lambda/D = 0.56$, by increasing the turbulence intensity from 4% to 10% , the lift coefficient on the upstream cylinder remains close to the lift coefficient value for the upstream cylinder in smooth flow. Also, when $\Lambda/D = 0.96$, the lift coefficient appears to

be constant at the value of the lift coefficient in smooth flow, when turbulence intensity increases. However, when $Tu = 4\%$ and $Re = 12000$, the lift coefficient has the least negative value. When $\Lambda/D = 1.28$, the lift coefficient decreases by increasing the turbulence intensity. This behaviour of the lift coefficient diminishes when Tu increases beyond 7% . The lift coefficient remains constant at the lower value of the lift coefficient (the most negative value of C_L) in smooth flow, see Fig. 37.

For the downstream cylinder, the behaviour of the drag coefficient with turbulence intensity appears to be similar for $Re = 6700, 9200$ and 12000 , see Fig. 38. The C_D of the downstream cylinder is lower than that for a single cylinder. This behaviour of the drag coefficient is in agreement with Gu et al. [30] results. Gu et al. [30] tested two circular cylinders in staggered arrangement at $Re = 6.5 \times 10^5$, when $Tu = 10\%$, and $\Lambda/D = 0.7$. Their experiments showed that C_D on the downstream cylinder is always less than that for a single cylinder when $1 \lesssim L/D \lesssim 4$, and $1 \lesssim T/D \lesssim 4$. Also, the drag coefficient for the downstream cylinder generally remains lower than the drag coefficient value for the corresponding upstream cylinder. This behaviour of the downstream cylinder indicates that the downstream cylinder is in the wake of the upstream cylinder. Figure 38 shows that the large integral length scale ($\Lambda/D = 1.28$) results a higher drag coefficient comparing to the one with $\Lambda/D = 0.56$ and 0.96 ($\Lambda/D \lesssim 1$) when turbulence intensity increases from $Tu = 4\%$ to 7% . However, when Tu increases beyond 7% the large integral length scale ($\Lambda/D = 1.28$) results a lower drag coefficient comparing to the one with $\Lambda/D = 0.56$ and 0.96 ($\Lambda/D \lesssim 1$), see Fig. 38. When $Re = 6700, 12000$ and $\Lambda/D = 0.56$, with increasing turbulence intensity from $Tu = 4\%$ to $Tu = 7\%$, the drag coefficient of the downstream cylinder increases and attains the value of the drag coefficient for the

downstream cylinder in smooth flow. However, when Tu increases beyond 7% ($Tu = 7%$ to $Tu = 10%$), the drag coefficient remains constant at the drag coefficient value of the downstream cylinder in smooth flow, as depicted in Fig. 38(a, c). When $Re = 9200$ and $\Lambda/D = 1.28$, with increasing turbulence intensity from $Tu = 4%$ to $Tu = 7%$, the mean drag coefficient of the downstream cylinder decreases and attains the drag coefficient value of the downstream cylinder in smooth flow, see Fig. 38(b).

Similar to the upstream cylinder, the downstream cylinder attains the negative lift value, see Fig. 38. When $\Lambda/D = 0.56$, Tu has a negligible effect on the lift coefficient of the downstream cylinder. Unlike C_D , the smallest variation of C_L with Λ/D is at $Tu = 4%$. The largest variation of C_L with Tu is at $\Lambda/D = 1.28$. The lift coefficient of the downstream cylinder experiences its less negative value when $Tu = 7%$ and $\Lambda/D = 1.28$.

The distribution of C_P (C_P vs. θ curves) of the upstream cylinder at $Re = 6700$ and $\Lambda/D = 0.56$ for different turbulence levels are given in Fig. 39(a). Also, Fig. 40(a) presents the C_P distribution around the upstream cylinder at $Re = 6700$ and $\Lambda/D = 1.28$ for different turbulence levels. Figures 39(b) and 40(b) present the pressure distribution around the downstream cylinder at $Re = 6700$, $\Lambda/D = 0.56$ and $\Lambda/D = 1.28$ for different turbulence levels, respectively. The stagnation point (the maximum positive C_P) is displaced away from the upstream wake axis for all the cases of turbulence, see Fig. 42. In other words, there is a peak at $\theta = 340^\circ$ corresponding to the stagnation point. Figures 39(b) and 40(b) show a significant C_{Pmin} is developed along the gap side of the downstream cylinder. This causes a lift force directed towards the upstream cylinder wake, see Appendix G.

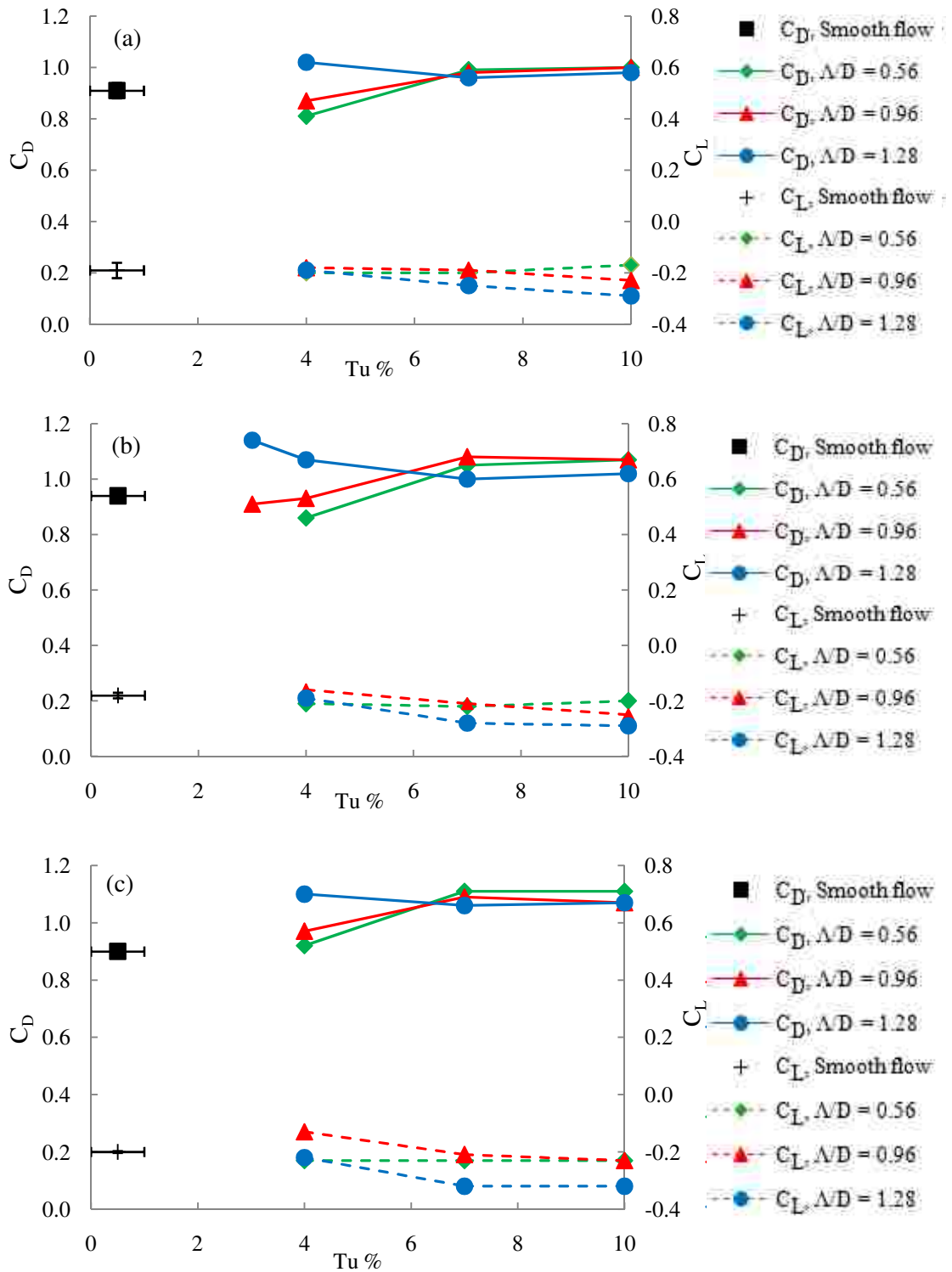


Fig. 37 Tu effects on the upstream cylinder (a) $Re = 6700$, (b) $Re = 9200$, and (c) $Re = 12000$, pressure measurement technique.

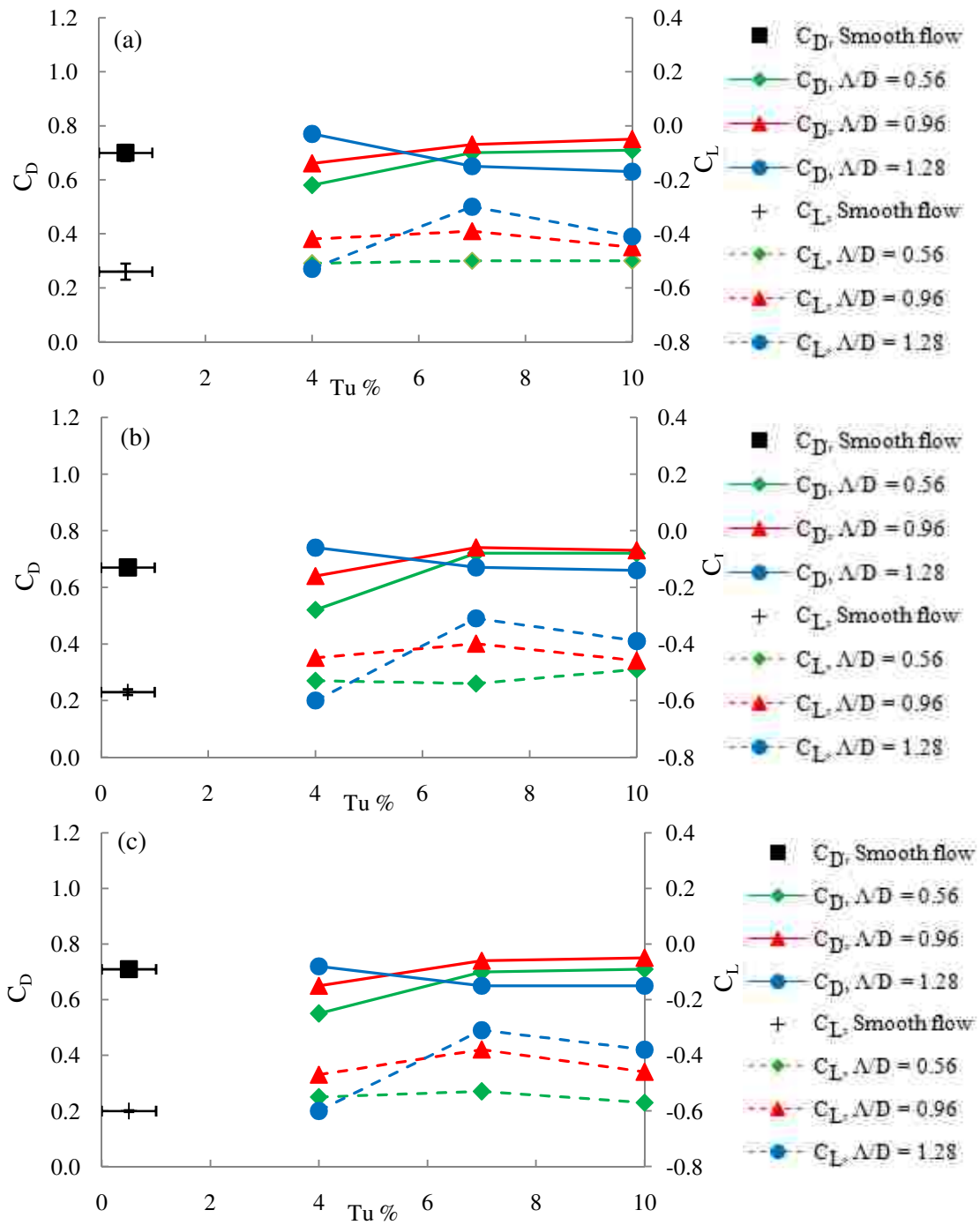


Fig. 38 Tu effects on the downstream cylinder (a) $Re = 6700$, (b) $Re = 9200$, and (c) $Re = 12000$, pressure measurement technique.

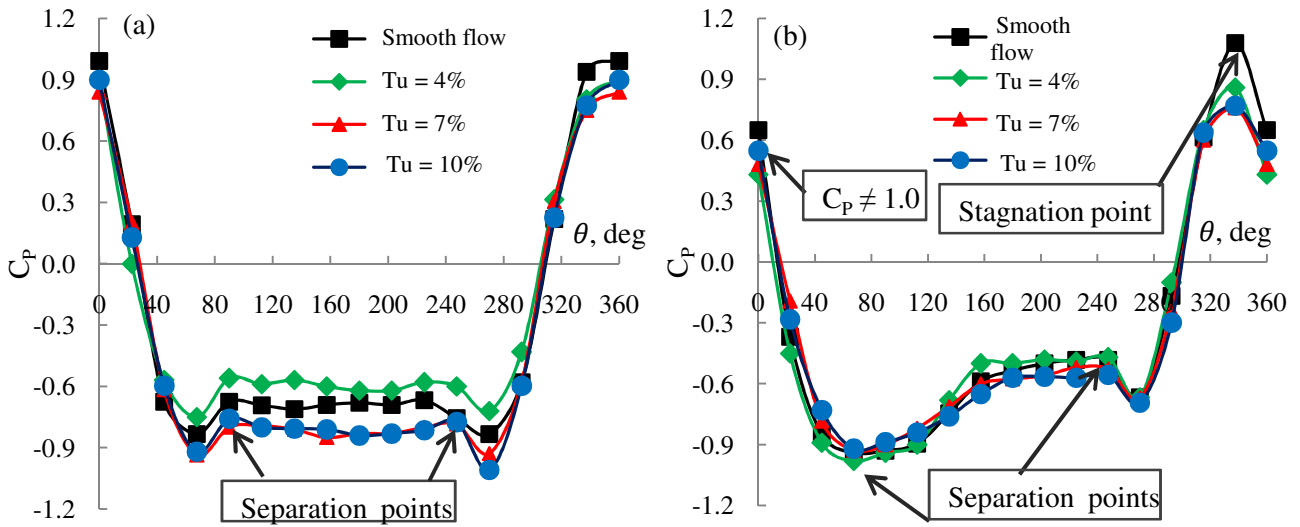


Fig. 39 Pressure distribution at $Re = 6700$ and $\Lambda/D = 0.56$ around (a) upstream cylinder, and (b) downstream cylinder.

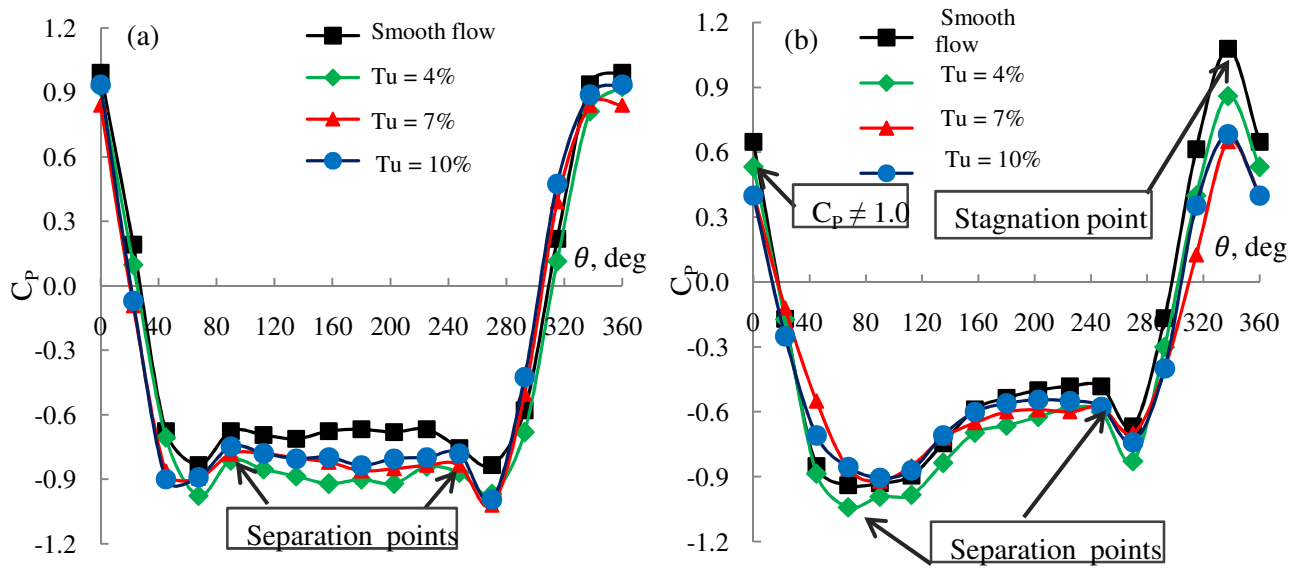


Fig. 40 Pressure distribution at $Re = 6700$ and $\Lambda/D = 1.28$ around (a) upstream cylinder, and (b) downstream cylinder.

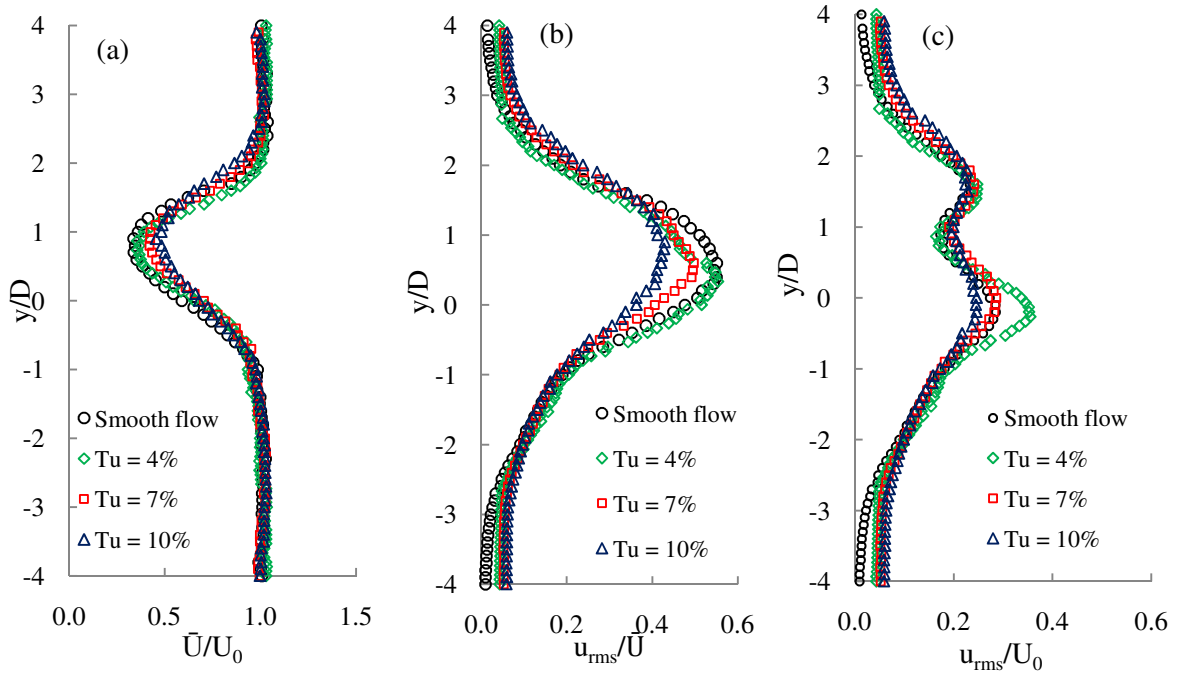


Fig. 41 Stream-wise mean velocity, turbulence intensity, and root mean square of velocity profiles at $Re = 6700$ and $\Lambda/D = 0.56$ (a) mean velocity, (b) turbulence intensity, and (c) root mean square of velocity.

The profiles of the stream-wise velocity, turbulence intensity, and root mean square of velocity for three different turbulence intensity values ($Tu = 4\%$ to 10%) with the constant normalized integral length scale ($\Lambda/D = 0.56$) are plotted in Fig. 41(a, b, c). Also, the profiles in smooth flow ($Tu \lesssim 0.5\%$) is plotted to assist analysis. These profiles are measured by traversing a hot-wire probe using 2D traverse system at $X/D = 2$ (see Fig. 21) over the range $-4 \lesssim y/D \lesssim 4$ with an interval of $\Delta y = 2.5 \times 10^{-3}$ m for $6.7 \times 10^3 \lesssim Re \lesssim 1.2 \times 10^4$.

Figure 41(a) shows that when $\Lambda/D = 0.56$ and $Tu = 10\%$, the wake is the widest and has the largest velocity (0.45) at the peak of the profile. Also, when $\Lambda/D = 0.56$ and

$Tu = 7\%$, the wake is as wide as the wake generated with $Tu = 10\%$ and the velocity at the peak is slightly less than 0.45(0.43). As a result, the velocity profiles show when $Tu \gtrsim 7\%$ and $\Lambda/D = 0.56$ the drag coefficients remain almost constant. It is a good agreement with the pressure measurement results, which indicated that when Tu increases beyond 7% the drag coefficient remains constant for both upstream and downstream cylinders. It has also been observed that when the turbulence intensity decreases to 4%, the wake becomes narrower but the drastic decrease of the velocity occurred at the peak of the velocity profile (0.35), see Figure 41(a). In Fig. 41(a), we can see that the drag coefficient obtained at $Tu = 4\%$ is smaller than the one achieved in smooth flow since the stream-wise velocity profile for $Tu = 4\%$ is narrower than the profile for the smooth flow. This result is in an agreement with the pressure measurement results, which showed that when $Re = 6700$ at $Tu = 4\%$ and $\Lambda/D = 0.56$ the drag coefficients on both upstream and downstream cylinders are smaller than the one in smooth flow, see Fig. 37(a), Fig. 38(a), and Fig. 39, see Appendix F.

The behaviour and appearance of the power spectra density (PSD), and the Strouhal number value would be helpful in understanding the physical relationship between the pressure measurement and the wake survey results. The vortex shedding frequency, f , is characterized in dimensionless form as the Strouhal number, $St (= fD/U_o)$. The power spectra density (PSD) is plotted at multiple vertical locations across the wake. Also, the power spectra density is plotted for the dynamic data of the load cell attached to the upstream or downstream cylinders when $Re = 6700$ and $\Lambda/d = 0.56$ for different turbulence intensities in Fig. 43. The PSD of the load cells show the Strouhal number measured at the upstream and downstream cylinders are nearly the same, which indicates

that a single vortex shedding process is present. When the free-stream turbulence intensity is $\lesssim 0.5\%$ (smooth flow), the Strouhal number value is 0.19, see Fig. 43(a). However, for a single cylinder in smooth flow the $St = 0.21$. The weak harmonic frequencies are identified at some locations at $St = 0.38$ and $St = 0.34$ for smooth flow and $Tu = 4\%$, respectively, see Fig. 43(a, b).

As shown in Fig. 43(b, c, d), there is a reduction in the Strouhal number from $St = 0.19$ for smooth flow to $St = 0.17$ for turbulence flow. By increasing turbulence intensity from $Tu = 4\%$ to $Tu = 10\%$, the Strouhal number value remains constant at $St = 0.17$. However, increasing turbulence intensity causes the strength of the vortex shedding to decrease, especially at $Tu = 10\%$ for the load cells.

It is seen from the power spectra in Fig. 43 that the vortex shedding peaks are obvious across the wake, and the amplitude only decreases when $y/D = 1.5$ (at the location of the outer shear layer of the downstream cylinder). This weakening of the vortex shedding peak at this location may be associated to the impingement of the vortices shed from the upstream cylinder onto the downstream cylinder and the interaction of two vortex streets, see Fig. 42. This phenomenon was previously reported by Sumner et al. [22] for laminar flow. A clear and distinct peak at PSD shows the existence of a dominant vortex structure due to regular vortex shedding.

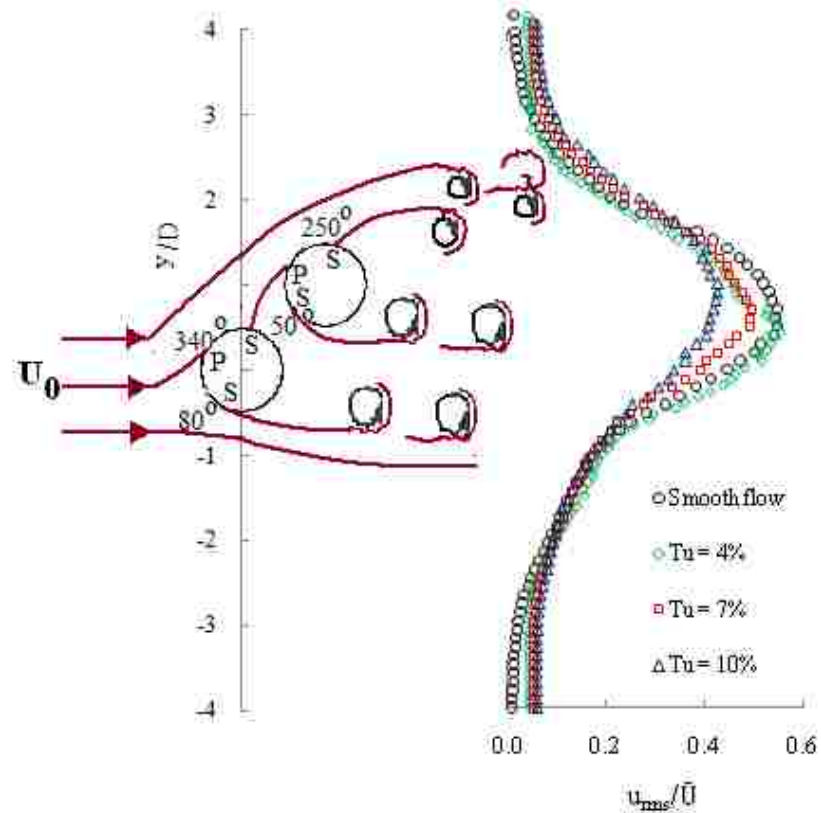
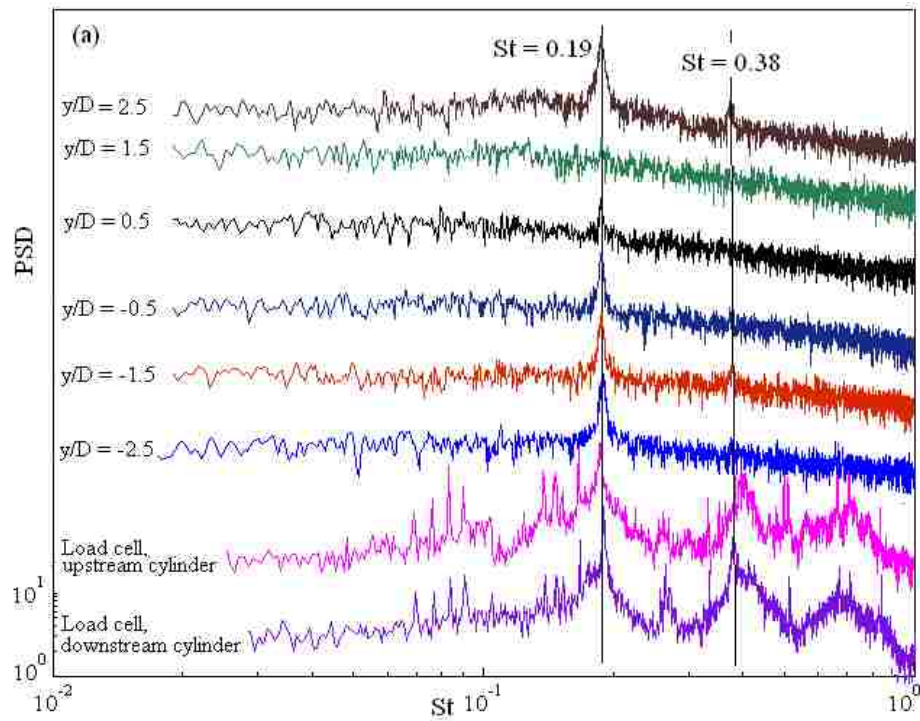
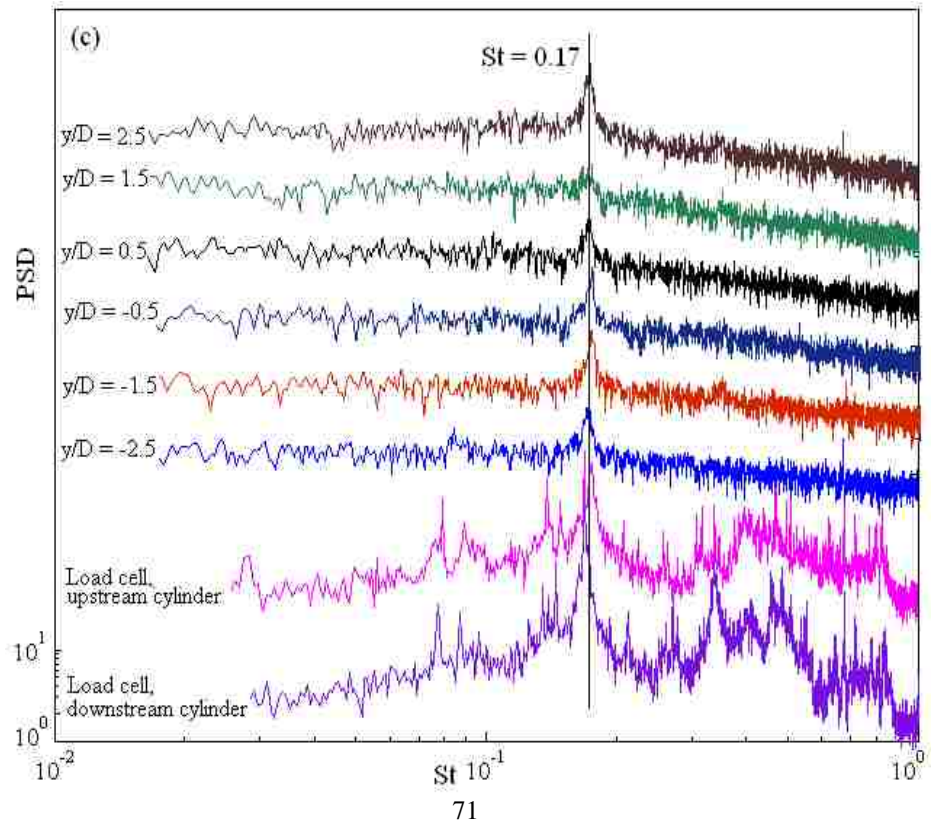
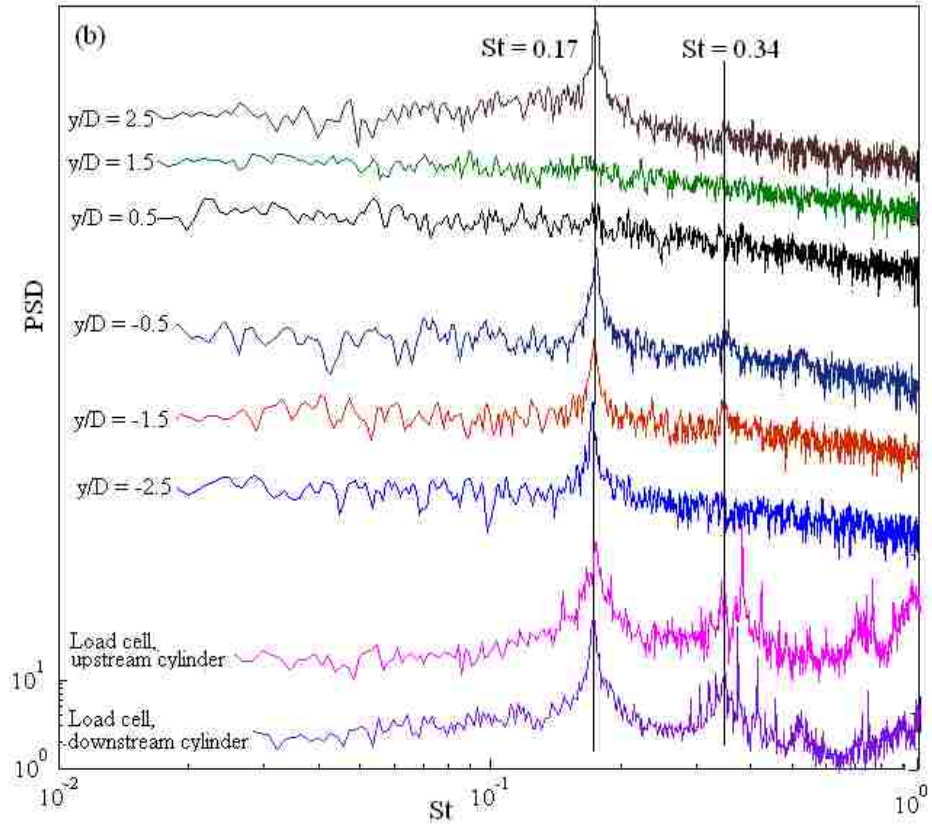


Fig. 42 Flow pattern and turbulence intensity profile for two cylinders in turbulence flow, “S” signifies the separation point, and “P” denotes the stagnation point.





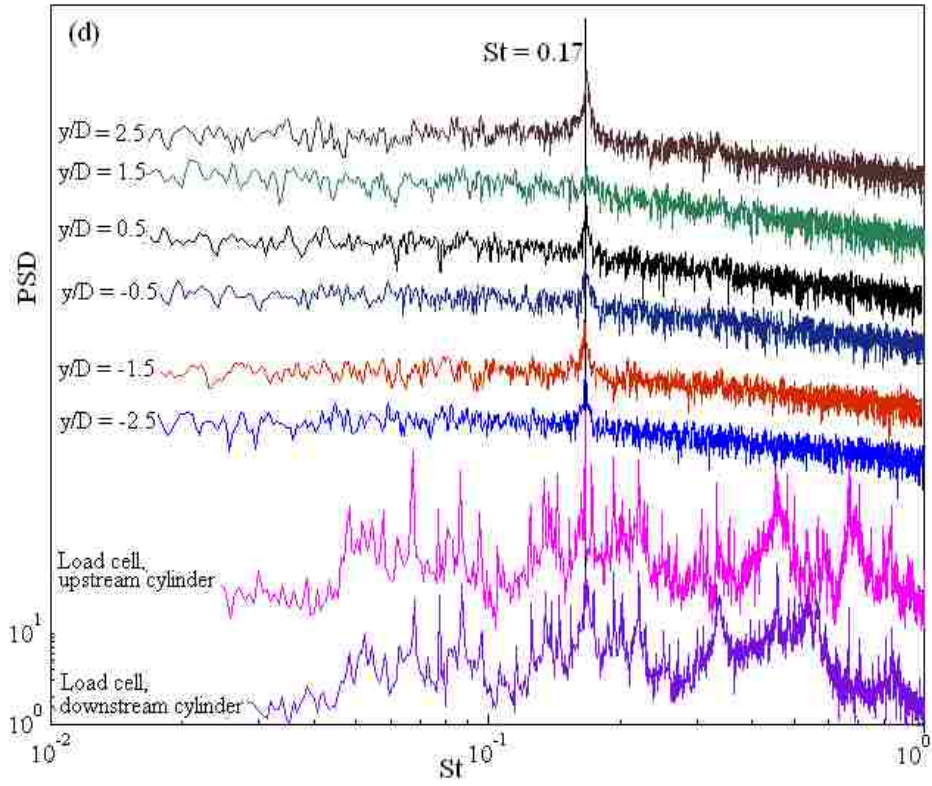


Fig. 43 PSD at different vertical locations across the wake th $Re = 6700$, and $\Lambda/D = 0.56$
 (a) smooth flow, (b) $Tu = 4\%$, (c) $Tu = 7\%$, (d) $Tu = 10\%$, the vertical scale is arbitrary, but
 the same scale is used for all spectra.

5.3. Effect of integral length on two staggered cylinder

This section will discuss the effect of integral length scale ($0.56 \lesssim \Lambda/D \lesssim 1.28$) on the drag and lift coefficients of the upstream and downstream cylinders when $6.7 \times 10^3 \lesssim Re \lesssim 1.2 \times 10^4$ at three different turbulence intensities ($Tu = 4\%$, 7% , and 10%). Since the uncertainty in dynamic force measurement (0.25, the maximum uncertainty in the drag and lift coefficients associated with the minimum free-stream velocity, $U_o = 3.0$ m/s, in this study) is higher than the uncertainty in pressure measurement (0.03), the drag and lift coefficients obtained by pressure measurement are considered more reliable. Thus, in this section, the results are to be mainly based on the pressure measurement method. Appendix E includes the dynamic force measurement results, which are in an agreement with the pressure measurement results. The integral length scale effects on the upstream and downstream can be inspected from the pressure measurement results, which can be found in Fig. 44 and Fig. 45.

Figure 44(a) shows that for the upstream cylinder at $Tu = 4\%$, the drag coefficient value increases when the value of Λ/D increases from 0.56 to 1.28 for $6.7 \times 10^3 \lesssim Re \lesssim 1.2 \times 10^4$. This behaviour of the upstream cylinder at $Tu = 4\%$ is in agreement with a trend of increasing drag coefficient while increasing Λ/D for a single cylinder, when $Re \cong 4 \times 10^4$ and $0.36 \lesssim \Lambda/D \lesssim 9.8$ [15]. As shown in Fig. 44(b) and 44(c) at $Tu = 7\%$ and $Tu = 10\%$, respectively, the drag coefficient value is almost constant when the value of Λ/D increases from 0.56 to 1.28.

Figure 44(a) presents that for the upstream cylinder, at $Tu = 4\%$ with increasing Λ/D from 0.56 to 1.28, the lift coefficient value is constant (at the value of the lift coefficient on the upstream cylinder in smooth flow) in $6.7 \times 10^3 \lesssim Re \lesssim 1.2 \times 10^4$. When

$Tu = 7\%$ and $\Lambda/D = 0.56$ and 0.96 ($\Lambda/D \lesssim 1$), increasing Λ/D appears to have negligible effect on the lift coefficient and it remains constant at the lift coefficient value of the upstream cylinder in smooth flow. However, when $\Lambda/D = 1.28$ increasing Λ/D causes decreasing in lift coefficient value; see Figure 44(b). When $Tu = 10\%$, the lift coefficient value attains more negative value when the value of Λ/D increases from 0.56 to 1.28 for $6.7 \times 10^3 \lesssim Re \lesssim 1.2 \times 10^4$, see Fig. 44(c).

For the downstream cylinder, when $Tu = 4\%$ increasing the Λ/D leads to an increase in the drag coefficient, see Fig. 45(a). However when $Tu = 7\%$ and $Tu = 10\%$, increasing Λ/D from 0.56 to 0.96 ($\Lambda/D \lesssim 1$) causes the drag coefficient to remain constant. Any further increase in Λ/D from 0.96 to 1.28 ($\Lambda/D > 1$) causes a slight decrease in the drag coefficient value, as shown in Fig. 45(b, c). It is worth pointing out that the largest Λ/D effect on the drag coefficient of the upstream and downstream cylinders is when $Tu = 4\%$ in the range of $6.7 \times 10^3 \lesssim Re \lesssim 1.2 \times 10^4$.

As shown in Fig. 45, increasing Λ/D from 0.56 to 0.96 ($\Lambda/D \lesssim 1$), causes the lift coefficient to increase. When $Tu = 4\%$ and $\Lambda/D = 1.28$, the lift coefficient decreases slightly with increasing Λ/D , as shown in Figure 45(a). However, when $Tu = 7\%$ and $Tu = 10\%$, by increasing Λ/D from 0.96 to 1.28 ($\Lambda/D > 1$) the lift coefficient also increases.

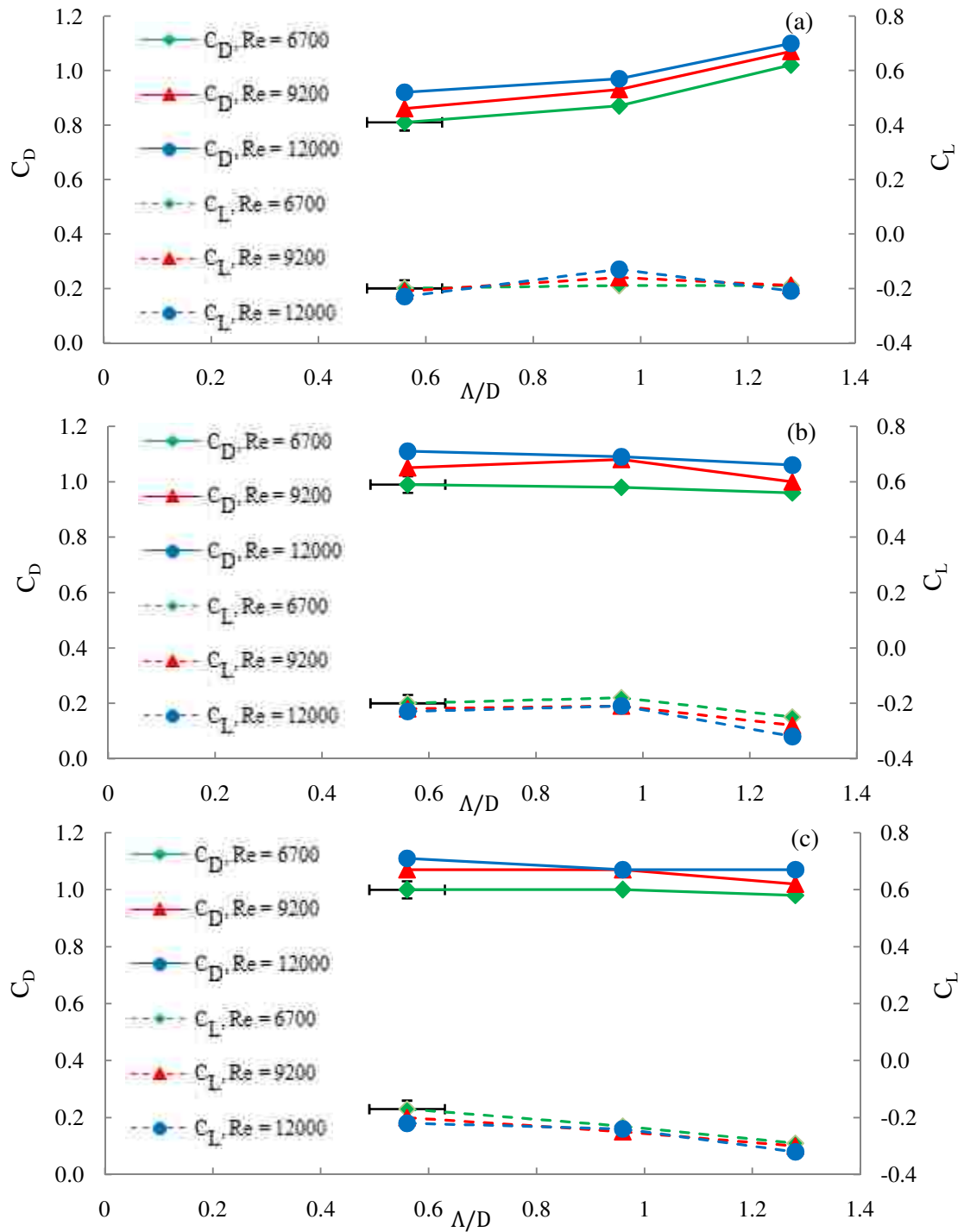


Fig. 44 Λ/D effects on the upstream cylinder (a) $Tu = 4\%$, (b) $Tu = 7\%$, and (c) $Tu = 10\%$, pressure measurement technique.

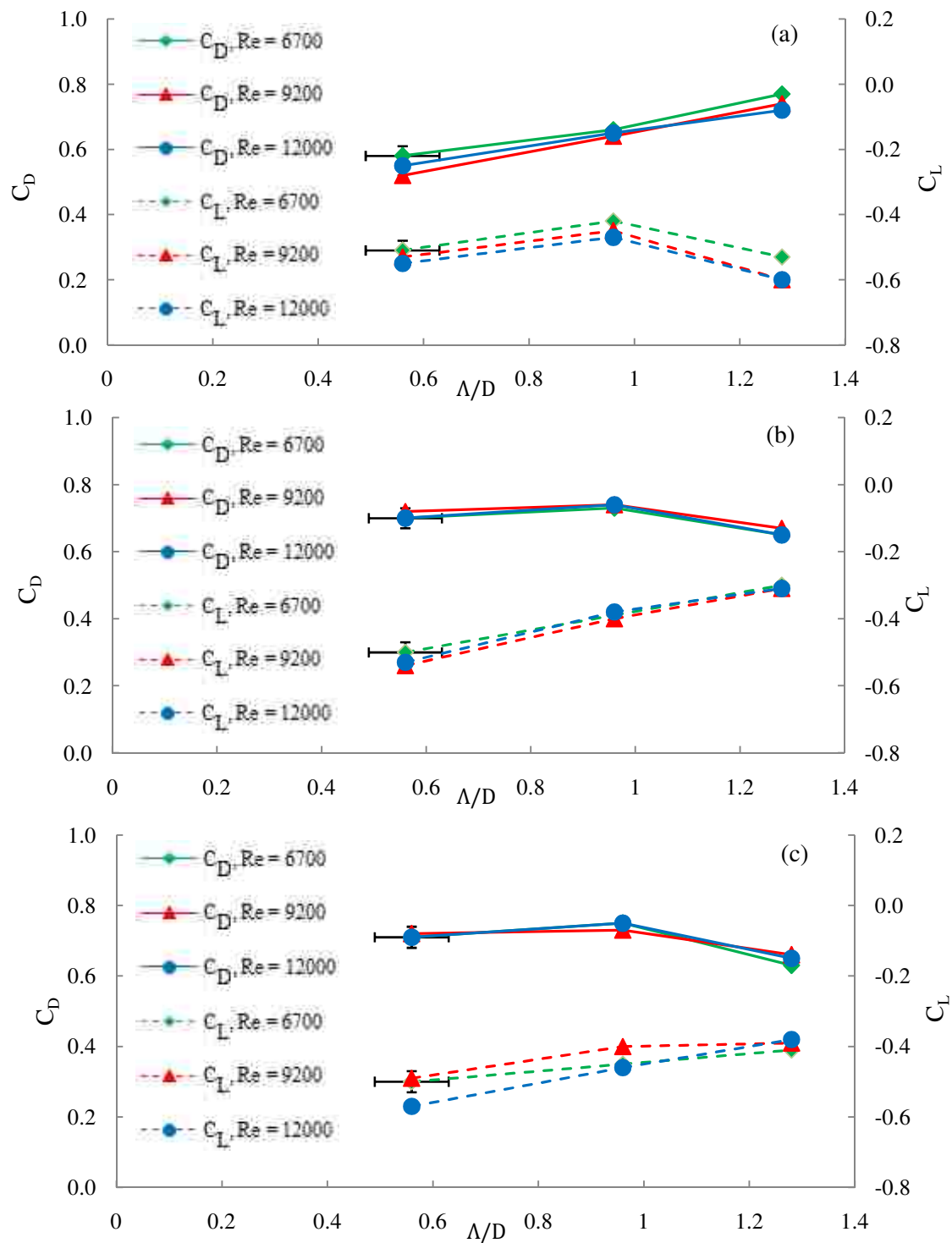
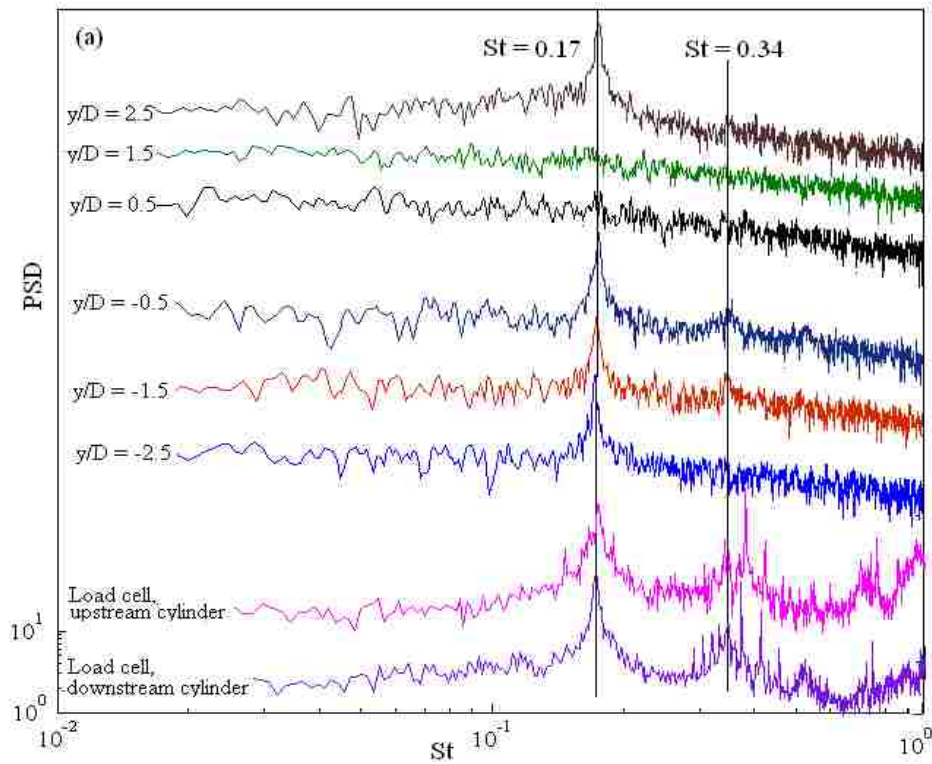


Fig. 45 Λ/D effects on the downstream cylinder (a) $Tu = 4\%$, (b) $Tu = 7\%$, and (c) $Tu = 10\%$, pressure measurement technique.

5.4. Comments on the effect of Re on PSD

The PSD are plotted at $Tu = 4\%$ and $\Lambda/D = 0.56$ for three different Reynolds numbers in Figure 46. It reveals that the Strouhal number is fixed at $St = 0.17$ for $6.7 \times 10^3 \lesssim Re \lesssim 1.2 \times 10^4$ in turbulence flow. The value of Strouhal number in turbulence flow is less than the value of the Strouhal number for two cylinders in smooth flow ($St = 0.19$). Zdravkovich [22] explained that for flow past two circular cylinders in smooth flow, a linear rise in the free-stream velocity results in a linear increase in the eddy shedding frequency, so the St remains constant throughout the TrSL (transition in shear layer flow region). Figure 46 presents that this feature of St for two circular cylinders in smooth flow will be reiterated for two circular cylinders in turbulence flow.



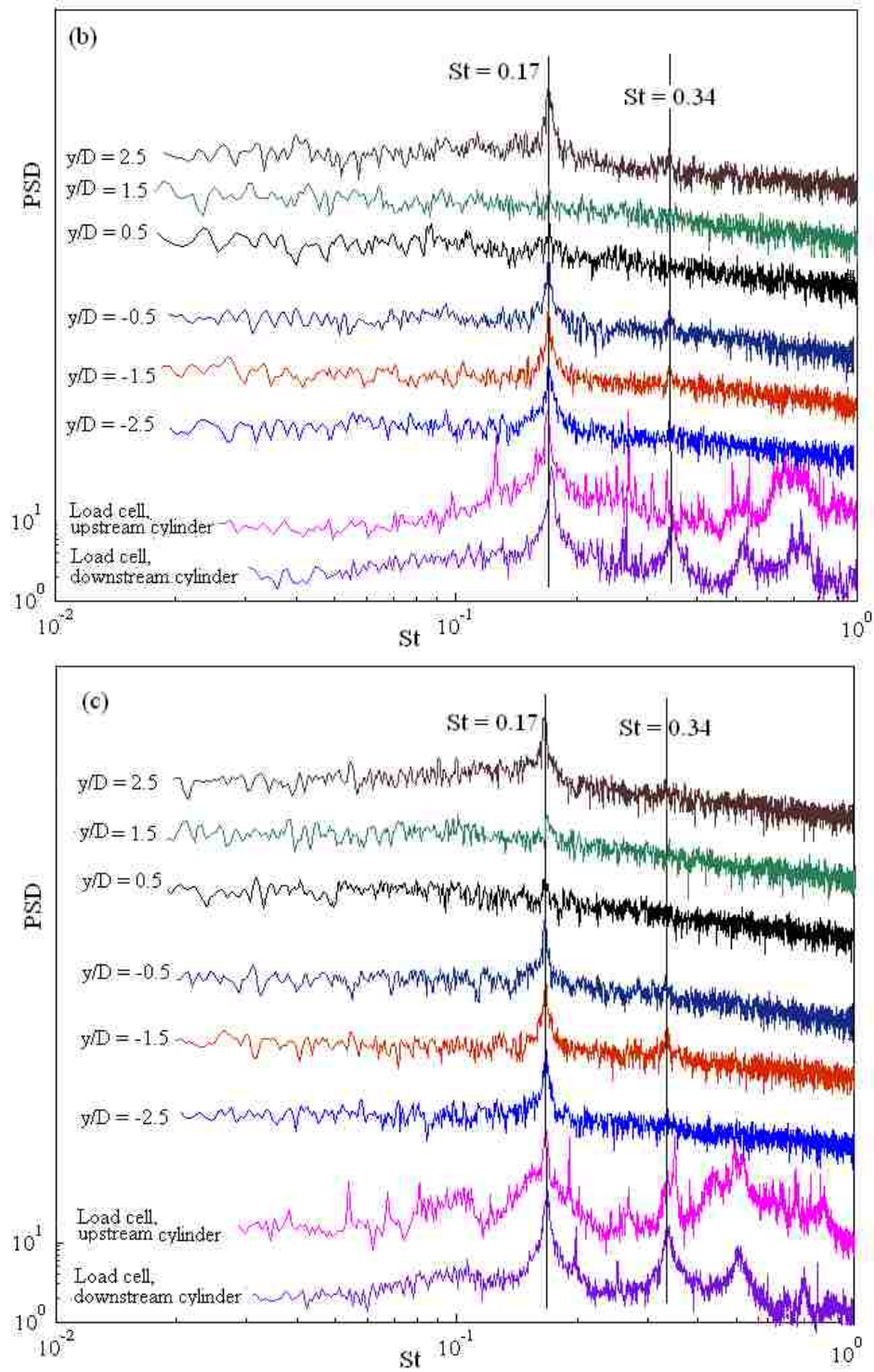


Fig. 46 PSD at different vertical locations across the wake at $Tu = 4\%$ and $\Lambda/D = 0.56$: (a) $Re = 6700$, (b) $Re = 9200$, and (c) $Re = 12000$. The vertical scale is arbitrary, but the same scale is used for all spectra.

5.5. Practical implications

A pair of circular cylinders can be found in engineering applications such as pipe rack structures in petrochemical facilities, shell and tube heat exchangers, and compressed air energy storage cylindrical bags at the bottom of a river or lake, and VIVACE (Vortex Induced Vibrations Aquatic Clean Energy) converter. The periodic vortex shedding from these structures can lead to vibrations. When the vibration frequency approaches the natural frequency of the cylinder and its supporting system, resonance may occur. The energy from vibrations can be destructive and are engineered out of designs. In many engineering cases, the calculation of the fluid loads on the structures is not specifically addressed in the current design codes. For example, in ASCE 7, the U.S. national wind loading standard (ASCE, 2002), only a case for a single cylinder is given for designing the pipe rack structures. This situation has forced the practicing engineers to make many assumptions. As a result, these simplifications may over- or under-estimate the wind load on the pipe rack structures, which can lead to a structural failure. The results of this study would be helpful for determining wind loads on pipe racks.

In the other hand, the vortex induced vibration can be useful to generate power from fluid flow (ocean, river, etc). VIVACE converter is a device can turn potentially destructive vibrations in fluid flows into clean, renewable power. VIVACE is based on the idea of maximizing and exploiting the vortex induced vibration rather than spoiling and suppressing it. This device uses vortices in the wake of the cylinders in the flow. The cylinders are vibrated up and down on springs creating energy harnessed to generate

electrical power. The results of the current study would be useful for designing VIVACE cylinders orientations.

CHAPTER VI

CONCLUSIONS AND RECOMMENDATIONS

The effects of turbulence intensity (Tu), normalized integral length scale (Λ/D), and Reynolds number on the force coefficients of two staggered circular cylinder ($L/D = 4$, and $T/D = 1$) were investigated in cross flow. The investigation was conducted in a closed-loop wind tunnel when $6.7 \times 10^3 \lesssim Re \lesssim 1.2 \times 10^4$. The turbulence intensity was varied from 0.5% to 10%, while, the normalized integral length scale was varied from 0.56 to 1.28.

6.1. Conclusions

Drag and lift coefficients were reported for a single and two staggered cylinders ($L/D = 4$, and $T/D = 1$), as well as the drag and lift coefficients for two staggered cylinders in both smooth and turbulence flows. Results from a single and two cylinders in smooth flow were compared to values reported in the literature for validation. Good agreements for all of these comparisons confirmed the proper performance of the experimental set-up. The following conclusions were achieved based on these experiments.

1. The current results have shown that the downstream cylinder is in the wake of the upstream cylinder either in smooth or turbulence flow. The drag coefficient for the downstream cylinder remains lower than the drag coefficient value for the corresponding upstream cylinder.
2. It seems that Λ/D have a larger effect on the drag coefficient of both upstream and downstream cylinders, when $Tu = 4\%$. In the other word, when $Tu = 4\%$, increasing Λ/D dramatically changes the drag coefficients of both upstream and

downstream cylinders. Also, it appears that Λ/D does not have a significant effect on the lift coefficients of the upstream and downstream cylinders.

3. When $\Lambda/D = 0.56$ and 0.96 ($\Lambda/D \lesssim 1$), with increasing turbulence intensity from $Tu = 4\%$ to $Tu = 7\%$, the mean drag coefficient of the cylinders increases and remains constant with any further rise in turbulence intensity ($Tu = 7\%$ to 10%). However, when $\Lambda/D = 1.28$, with increasing turbulence intensity from $Tu = 4\%$ to $Tu = 7\%$, the mean drag coefficient of the cylinders decreases and remains constant with any further rise in turbulence intensity ($Tu = 7\%$ to 10%). The lift coefficient of the cylinders attains the negative value all the time. It is clear that $\Lambda/D = 0.56$ is least changed with Tu as far as C_L is concerned. When $\Lambda/D > 1$, the lift coefficient of the downstream cylinder experiences its less negative value at $Tu \gtrsim 7\%$.
4. When $6.7 \times 10^3 \lesssim Re \lesssim 1.2 \times 10^4$, the mean aerodynamic force coefficients are roughly constant and Re effect is negligible.
5. The C_D for the upstream cylinder was found to be less affected by the downstream cylinder. It behaved much like a single cylinder. The C_p distribution around the downstream cylinder shows that the stagnation point is shifted away from the upstream wake. Also, a significant $C_{p_{min}}$ is developed at $50^\circ \lesssim \theta \lesssim 90^\circ$ (along the gap side of the downstream cylinder) either in smooth or turbulence flow. This causes a lift force directed towards the upstream cylinder wake.
6. With increasing turbulence intensity from $Tu = 0.5\%$ to $Tu = 10\%$ the laminar boundary layer remains very stable when $6.7 \times 10^3 \lesssim Re \lesssim 1.2 \times 10^4$.

7. The value of Strouhal number in turbulence flow is constant ($St = 0.17$) and is less than the value of the Strouhal number for two cylinders in smooth flow ($St = 0.19$). The Strouhal number was identical for the two cylinders which indicate that there is a single vortex street process.

6.2. Recommendations

- I. Tests at higher Reynolds numbers.

In the critical region of Re , Re has a significant effect on the aerodynamic forces of two cylinders. In this study, Re appears to have negligible effect on the drag and lift coefficients due to the narrow range of Re ($6.7 \times 10^3 \lesssim Re \lesssim 1.2 \times 10^4$) in subcritical range. To observe the effect of Re on two cylinders in turbulence flow, it would be helpful to conduct the tests at critical range of Re .

- II. Tests with different spacing and orientation (in different interference regimes), and/or in wider range of Tu than the current range of turbulence intensity ($4\% \lesssim Re \lesssim 10\%$).

To find the appropriate design for two circular cylinders for practical applications, it is necessary to examine different spacing and orientation of two cylinders. The results show that at $Tu = 4\%$, turbulence intensity has a largest effect. To uncover the underlying reason, it would be practical if we had results at lower turbulence intensities than $Tu = 4\%$.

- III. Tests with one or both oscillated cylinders.

To uncover the proper design of two cylinders in practical applications it is useful to let one or both cylinders free to vibrate.

- IV. The upstream cylinder wake measurement by using hot-wire probe.

To better understand the flow field around two cylinders, interaction between shear layers, and the wake of the downstream cylinder, it would be very useful if we had some information about the wake of the upstream cylinder.

REFERENCES

- [1] Ting, D. S.-K., D. J. Wang, S. J. Price, M. P. Paidoussis, (1998). “An experimental study on the fluid elastic forces for two staggered circular cylinders in cross flow” *Journal of Fluids and Structures*, 12: 259–294.
- [2] Zdravkovich, M. M. (1997). Flow around circular cylinders Oxford University Press.
- [3] Blevins, R. D. (1990). Flow induced vibration New York: Van Nostrand Reinhold Co.
- [4] Coutanceau, M., R. Bouard, (1977). “Experimental determination of the main features of the viscous flow in the wake of a circular cylinder in uniform translation” *Journal of Fluid Mechanics*, 79(2): 231-256.
- [5] Gerrard, J. H. (1978). “The wakes of cylindrical bluff bodies at low Reynolds number” *Phil. Trans. Roy. Soc. (London) Ser. A*, 288(1354): 351-382.
- [6] Huerre, P., P. A. Monkewitz, (1990). “Local and global instabilities in spatially developing flow” *Annual Review of Fluid Mechanics*, 21.
- [7] Bloor, S. (1964). “The transition to turbulence in the wake of a circular cylinder” *Journal of Fluid Mechanics*, 19(2): 290-304.
- [8] Roshko, A. (1954). “On the development of turbulent wakes from vortex streets” *NACA Rep.*, 1191.
- [9] Karniadakis, G. M., G. S. Triantafyllou, (1992). “Three-dimensional dynamics and transition to turbulence in the wake of bluff objects” *Journal of Fluid Mechanics*, 238: 1-30.
- [10] Bearman, P. W. (1969). “On vortex shedding from a circular cylinder in the critical Reynolds number regime” *Journal of Fluid Mechanics*, 37(3): 577-585.

- [11] Roshko, A. (1961). "Experiments on the flow past a circular cylinder at very high Reynolds number" *Journal of Fluid Mechanics*, 10: 345-356.
- [12] Younis, N. (2009). "The role of turbulent integral length scale on the drag of a circular cylinder in cross flow" M.S. Thesis, University of Windsor, Windsor, Ontario, Canada.
- [13] Sanitjai, S., R. J. Goldstein, (2001). "Effect of free-stream turbulence on local mass transfer from a circular cylinder" *International Journal of Heat and Fluid Flow*, 44: 2863-2875.
- [14] Norberg, C., B. Sunden, (1987). "Turbulence and Reynolds number effects on the flow and fluid forces on a single cylinder in cross flow" *Journal of Fluids and Structures*, 1: 337-357.
- [15] Surry, D. (1972). "Some effects of intense turbulence on the aerodynamics of a circular cylinder at subcritical Reynolds number" *Journal of Fluid Mechanics*, 52: 543-563.
- [16] Blackburn, H. M., W. H. Melbourne, (1996). "The effect of free-stream turbulence on sectional lift forces on a circular cylinder" *Journal of Fluid Mechanics*, 306: 267-292.
- [17] Cheung, J. C. K., W. H. Melbourne, (1983). "Turbulence effects on some aerodynamic Parameters of a circular cylinder at supercritical Reynolds numbers" *Journal of Wind Engineering and Industrial Aerodynamics*, 14(1-3): 399-410.
- [18] Sumner, D. (2010). "Two circular cylinders in cross flow: A review" *Journal of Fluids and Structures*, 26(6): 849-899.
- [19] Hori, E. (1959). "Experiments on flow around a pair of parallel circular cylinders" *Proc. 9th Japan National Congress for Applied Mech.*, Tokyo, 231-234.

- [20] Zdravkovich, M. M. (1987). "The effect of interference between circular cylinders in cross flow" *Journal of Fluid and Structures*, 1: 239-262.
- [21] Gu, Z., T. Sun, (1999). "On interference between two circular cylinders in staggered arrangement at high subcritical Reynolds numbers" *Journal of Wind Eng. Ind. Aerodyn*, 80: 287-309.
- [22] Sumner, D., S. J. Price, M. P. Paidoussis, (2000). "Flow pattern identification for two staggered circular cylinders in cross flow" *Journal of Fluids and Structures*, 411: 263-303.
- [23] Sumner, D., O. O. Akosile, (2004). "Behaviour of a closely spaced pair of circular cylinders in cross-flow" CSME. University of Saskatchewan, Saskatoon, Saskatchewan, Canada.
- [24] Sumner, D., M. Richards, O. O. Akosile, (2005). "Two staggered circular cylinders of equal diameter in cross flow" *Journal of Fluids and Structures*, 20(2): 255-276.
- [25] Liu, X., M. Levitan, D. Nikitopoulos, (2008). "Wind tunnel tests for mean drag and lift coefficients on multiple circular cylinders arranged in-line" *Journal of Wind Engineering and Industrial Aerodynamics*, 96(6-7): 831-839.
- [26] Ljungkrona, L., C. Norberg, B. Sunden, (1991), "Free-stream turbulence and tube spacing effects on surface pressure fluctuations for two tubes in an in-line arrangement" *Journal of Fluids and Structures*, 5: 701-727.
- [27] Liu, X., (2003). "Wind load on multiple cylinders arranged in tandem with effects of turbulence and surface roughness" M.S. Thesis. Louisiana State University. Baton Rouge, Louisiana.

- [28] Zdarvkovich, M. M., (1977). "Review of flow interference between two circular cylinders in various arrangements" *Journal of Fluid Mechanics*, 618-633.
- [29] Price, S. J., (1976). "The origin and nature of the lift force on the leeward of two bluff bodies" *The Aeronautical Quarterly*, 27: 154-168.
- [30] Gu, Z. F., T. F. Sun, D. X. He, L. L. Zhang, (1993). "Two circular cylinders in high-turbulence flow at supercritical Reynolds number" *Journal of Wind Engineering and Industrial Aerodynamics*, 49: 379-388.
- [31] De Silva, I., H. Fernando, (1994). "Oscillating grids as a source of nearly isotropic turbulence" *Physics of Fluids*, 6: 2455-2464.
- [32] Liu, R., D. S-K. Ting, (2007). "Turbulent flow downstream of a perforated plate: sharp-edged orifice versus finite-thickness holes" *Journal of Fluids Engineering*, 129: 1164-1171.
- [33] Belmabrouk, H., M. Michard, (1998). "Taylor length scale measurement by laser Doppler velocimetry" *Experiments in Fluids*, 25: 69-76.
- [34] Lee, S-J., H-C. Lim, M. Han, S-S. Lee, (2005). "Flow control of circular cylinder with a V-grooved micro-riblet film" *Fluid Dynamics Research*, 37(4): 246-266.
- [35] Schlichting, H., (1979). Boundary-layer theory New York: McGraw-Hill.
- [36] Yeboah, E. N., H. R. Rahai, J. C. La Rue, (1997). "The effects of external turbulence on mean pressure distribution, drag coefficient, and wake characteristics of smooth cylinders" *ASME Fluids Engineering Division Summer Meeting, FEDSM'97*, June 22 – 26.
- [37] Lim, H-C., S-J. Lee, (2004). "Flow control of a circular cylinder with O-rings" *Fluid Dynamics Research*, 35: 107-122.

[38] Suzuki, N., H. Sato, M. Iuchi, S. Yamamoto, (1971), "Aerodynamic forces acting on circular cylinders arranged in longitudinal row" Proceedings International Symposium, Wind Effects on Buildings and Structures, Tokyo, 377-386.

APPENDIX A: Surface roughness measurement

The model circular cylinders were aluminum tubes and subjected to the same level of surface roughness. All the cylinders were sanded, polished, and painted in dark green. The cylinder's surfaces were buffered by using NOVUS plastic polishes No. 2 and No. 1 to improve their smoothness. The surface roughness was tested in the laboratory of the University of Windsor and average roughness was 5.81×10^{-7} m. Fig. 47(a, b) illustrated the surface roughness at two different random locations of the surface at the model circular cylinder. Westerman and Sharcos [A1] showed that mechanically the smooth model should have roughness less than 1×10^{-6} m. Thus, the model is both mechanically and hydraulically is smooth.

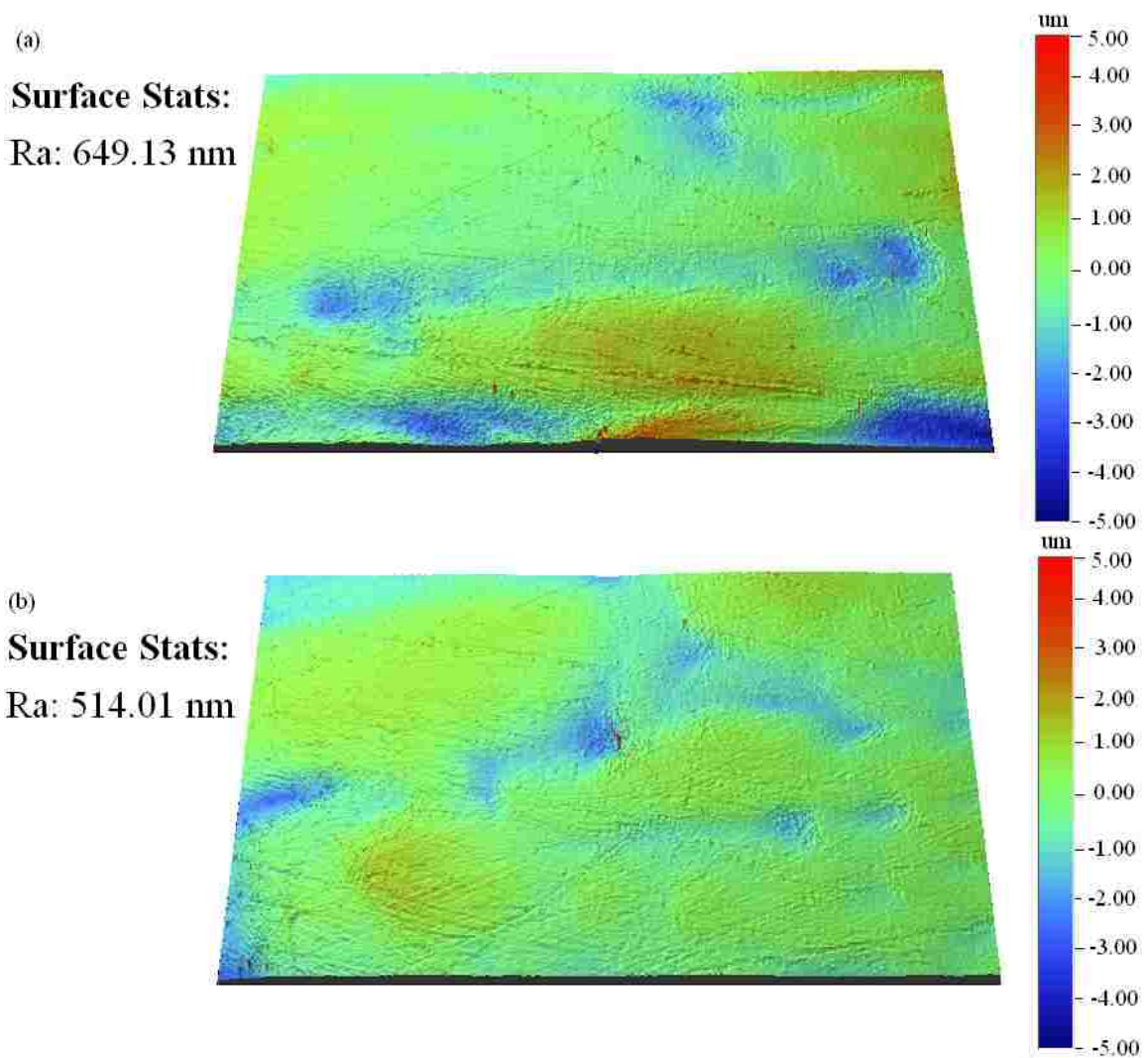


Fig. 47 The roughness of the cylinder: (a) first location, and (b) second location

REFERENCES

[A1] Westerman, J., E. Sharcos, (1966). “DIN 140 Standard (classified surface quality grade)”

No. 1304 standard: 160-200.

APPENDIX B: Selecting sample size and sample rate in the load cell

In this study, it was found that the accuracy of the results from the load cells can be affected by the sample size and sample rate. Thus, finding the minimum required sample size and sample rate was very important.

The minimum required sample size and sample rate were determined by investigating the convergence of the drag and lift forces and coefficients as a function of the sample size and sample rate respectively. The minimum sample size and sample rate were identified as the one beyond which the forces and coefficients remain unchanged with variation of the sample size and rate.

Figure 48 (a) to (d) show the variations of the drag force, lift force, drag coefficient and lift coefficient versus the sample rate, respectively, for the 25.4 mm cylinder at $U_o = 10.1$ m/s in smooth flow. It can be observed that all the graphs at sample rate of 2 kHz or higher are nearly stable. Therefore, the sample rate was set at 2 kHz for the load cells in this study.

Figure 49 (a) to (d) present the variations of the drag force, lift force, drag coefficient and lift coefficient versus the sample size for the load cells respectively, at 2 kHz. It can be inferred from figures that all the signals are nearly stable once the sample size is larger than 1.5×10^5 . Thus, the sample size of 1.5×10^5 was used for the load cells in this study.

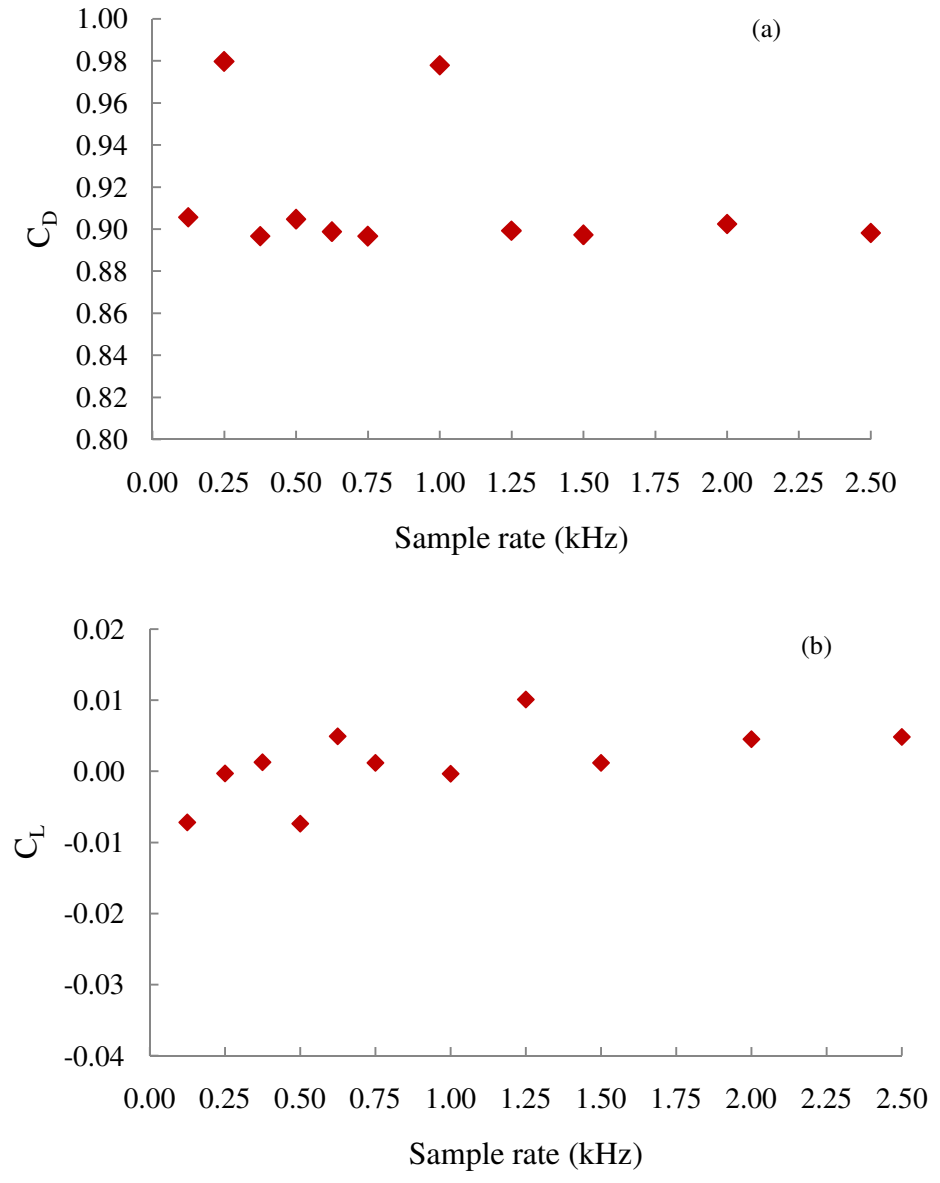


Fig. 48 Sample rate check for the load cells reading (a) C_D , and (b) C_L versus the sample rate, 25.4 mm cylinder, $Tu = 4\%$, $U_o = 4.5$ m/s.

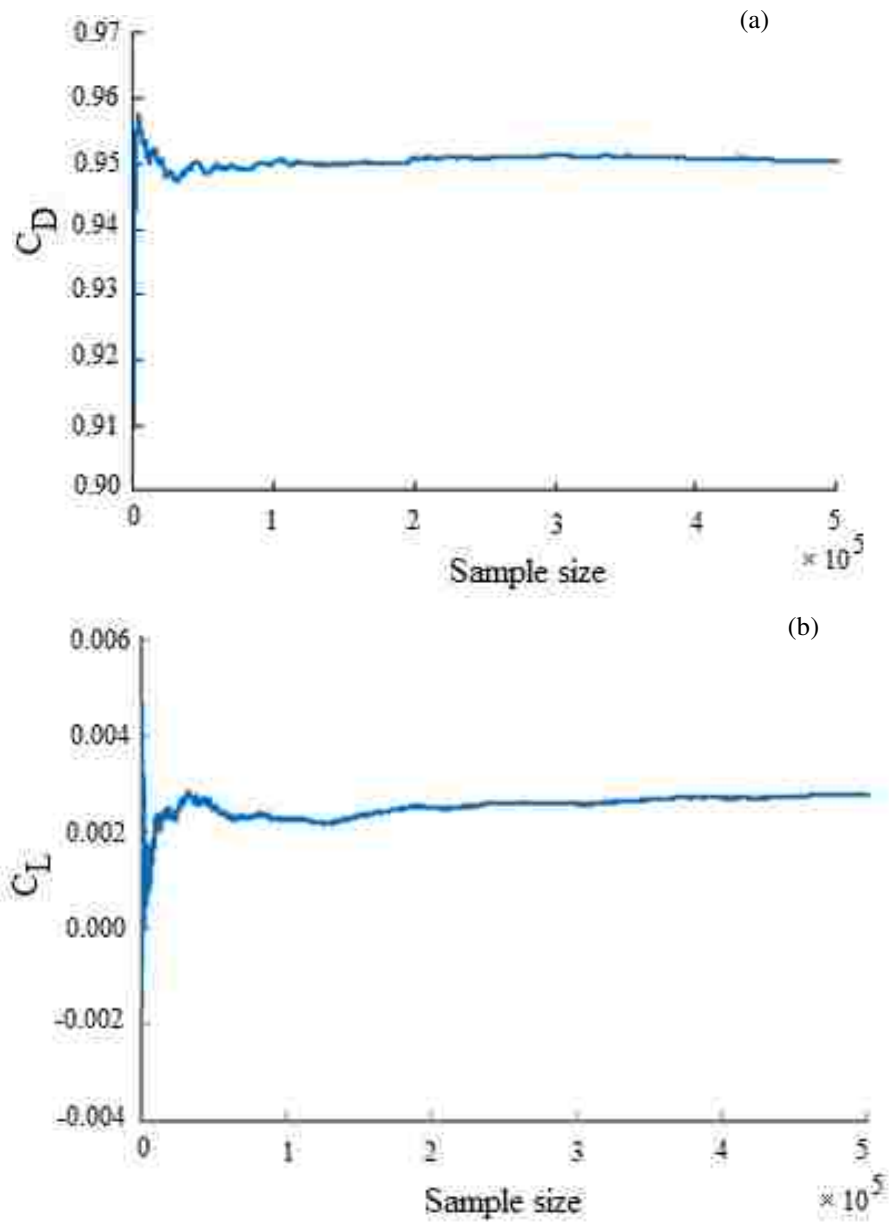


Fig. 49 Sample size check for load cell reading: (a) C_D , and (b) C_L versus sample size at sample rate 2 kHz, 25.4 mm cylinder, $Tu = 7\%$, $U_o = 6.2$ m/s.

APPENDIX C: Selecting sample size and sample rate in the hot-wire

Selecting the sample size value in the hot-wire anemometer measurement is very important. Figure 50(a) to (d) show the variations of the mean velocity, root mean square of value, turbulence intensity, and integral length scale, versus sample size, respectively, for d38.1 plate located at $10x/d$. It can be observed that all the graphs are nearly stable after sample size 2×10^6 . Therefore, the sample size was set at 2×10^6 for hot-wire in this study. Also, the sample frequency was set at 80 kHz for hot-wire in this study, which is more than twice the Nyquist frequency to avoid aliasing problems.

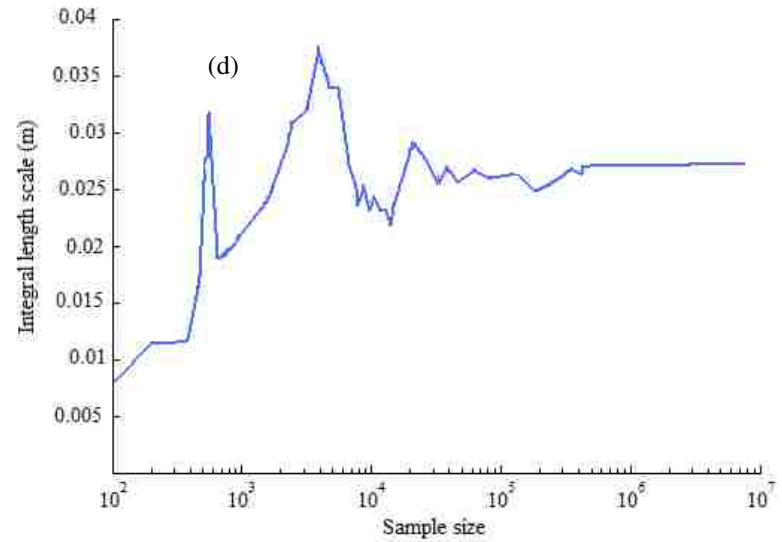
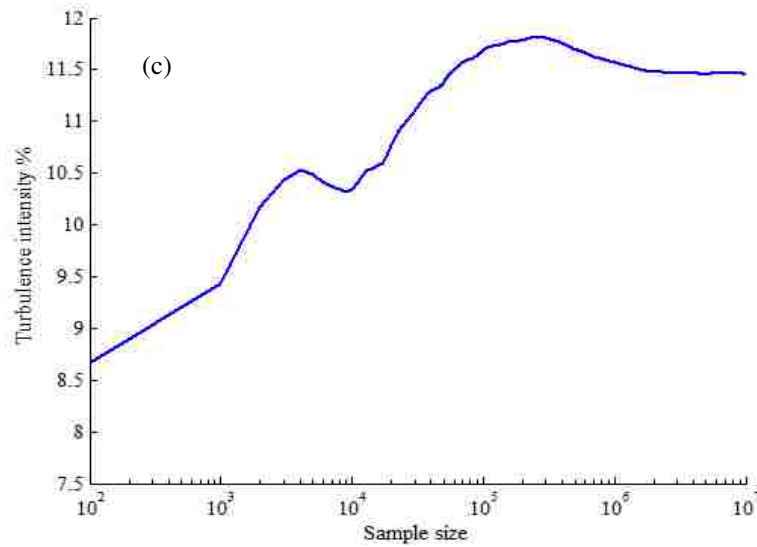
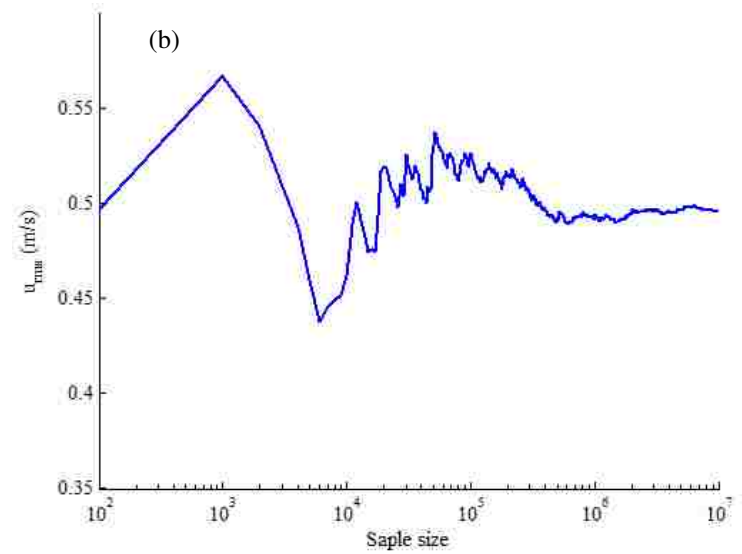
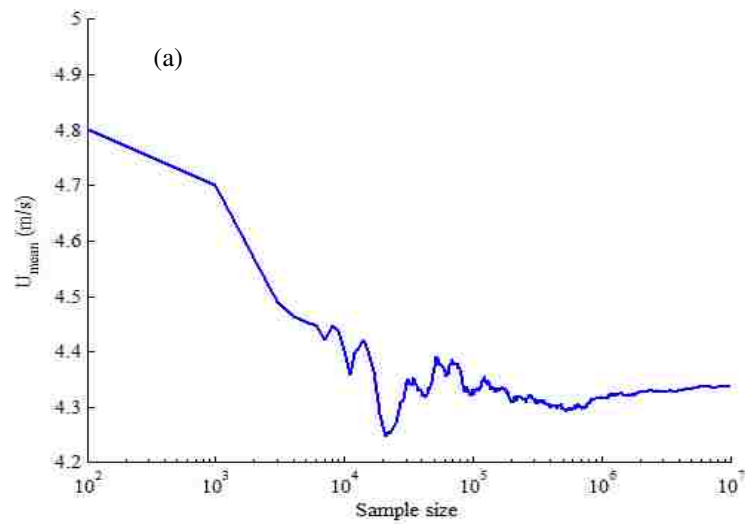


Fig. 50 Sample size check for d38.1 plate located at $10 x/d$ and $U_o = 4.3$ m/s (a) U_{mean} , (b) U_{rms} , (c) Tu%, and (d) integral length

APPENDIX D: Uncertainty analysis

D.1 Uncertainty in Reynolds number

The Reynolds number is:

$$\text{Re} = \frac{\rho \times U_o \times D}{\mu} \quad (\text{D.1})$$

the absolute uncertainty in Reynolds number is:

$$W_{\text{Re}} = \sqrt{\left(\frac{\partial \text{Re}}{\partial \rho} W_{\rho}\right)^2 + \left(\frac{\partial \text{Re}}{\partial U_o} W_{U_o}\right)^2 + \left(\frac{\partial \text{Re}}{\partial D} W_D\right)^2} \quad (\text{D.2})$$

Thus,

$$W_{\text{Re}} = \sqrt{\left(\frac{U_o \times D}{\mu} W_{\rho}\right)^2 + \left(\frac{\rho \times D}{\mu} W_{U_o}\right)^2 + \left(\frac{\rho \times U_o}{\mu} W_D\right)^2} \quad (\text{D.3})$$

the absolute uncertainty in temperature is:

$$(W_T)_{\text{Instrument error}} = \sqrt{(W_T)_{\text{Resolution}}^2 + (W_T)_{\text{Accuracy}}^2} \quad (\text{D.4})$$

By using Kestrel 4500 weather meter, the atmospheric temperature, and pressure of the lab are measured every time before any experiment. The Kestrel temperature resolution is 1°C, and the accuracy is $\pm 1^\circ\text{C}$.

$$W_T = \sqrt{\left(\frac{0.1}{2}\right)^2 + (1)^2} \cong 1^\circ\text{C} \quad (\text{D.5})$$

The Kestrel pressure resolution is 0.01 inHg, and the accuracy is ± 0.05 inHg. Thus, the absolute uncertainty in pressure is:

$$W_P = \sqrt{\left(\frac{0.1}{2}\right)^2 + (0.05)^2} \cong 0.05 \text{ inHg} \cong 170.33 \text{ Pa} \quad (\text{D.6})$$

The ideal gas equation is:

$$P = \rho \times R \times T \quad (D.7)$$

After neglecting the uncertainty of the gas constant, R, the absolute uncertainty in air density is:

$$W_{\rho} = \sqrt{\left(\frac{\partial \rho}{\partial P} W_P\right)^2 + \left(\frac{\partial \rho}{\partial T} W_T\right)^2} \quad (D.8)$$

Thus,

$$W_{\rho} = \sqrt{\left(\frac{W_P}{RT}\right)^2 + \left(-\frac{P \times W_T}{R \times T^2}\right)^2} \quad (D.9)$$

The gas constant is:

$$R = 287.05 \frac{\text{J}}{\text{kg} \times \text{K}} \quad (D.10)$$

The normal pressure and temperature in the lab are 99200 Pa and 294 K. Thus:

$$W_{\rho} = \sqrt{\left(\frac{170.33}{287.05 \times 294}\right)^2 + \left(-\frac{99200 \times 1}{287.05 \times (294)^2}\right)^2} = 0.00448 \frac{\text{kg}}{\text{m}^3} \quad (D.11)$$

The mean velocity is calculated by:

$$U_o = \sqrt{\frac{2 \times \Delta P}{\rho_{\text{air}}}} \quad (D.12)$$

The absolute uncertainty in free-stream velocity is:

$$W_{U_o} = \sqrt{\left(\frac{\partial U_o}{\partial \Delta P} W_{\Delta P}\right)^2 + \left(\frac{\partial U_o}{\partial \rho} W_{\rho}\right)^2} \quad (D.13)$$

$$W_{U_o} = \sqrt{\left(\sqrt{\frac{\rho}{2 \times \Delta P}} \times \frac{W_{\Delta P}}{\rho}\right)^2 + \left(\sqrt{\frac{\rho}{2 \times \Delta P}} \times \left(-\frac{\Delta P \times W_{\Delta P}}{\rho^2}\right)\right)^2} \quad (D.14)$$

The manometer hysteresis is $\pm 0.1\%$ of the full scale, and the accuracy is $\pm 0.5\%$ of the full scale. Thus, the absolute uncertainty in dynamic pressure is:

$$(W_{\Delta P})_{\text{Instrument error}} = \sqrt{(W_{\Delta P})_{\text{Resolution}}^2 + (W_{\Delta P})_{\text{Hysteresis}}^2} \quad (\text{D.15})$$

$$(W_{\Delta P})_{\text{Instrument error}} = \sqrt{(0.005 \times 0.294)^2 + (0.001 \times 0.294)^2} = 0.00127 \text{ kPa} \quad (\text{D.16})$$

$$W_{\Delta P} = \sqrt{(W_{\Delta P})_{\text{Instrument errors}}^2 + (W_{\Delta P})_{\text{Precision errors}}^2} \quad (\text{D.17})$$

$$W_{\Delta P} = \sqrt{(W_{\Delta P})_{\text{Instrument errors}}^2 + 0} = 0.00127 \text{ kPa} \quad (\text{D.18})$$

In this study, the smallest manometer reading is $\Delta P = 0.0052 \text{ kPa}$ for $U_o = 3 \frac{\text{m}}{\text{s}}$.

$$W_{U_o} = \sqrt{\left(\sqrt{\frac{1.17}{2 \times 5.2}} \times \frac{1.27}{1.17}\right)^2 + \left(\sqrt{\frac{\rho 1.17}{2 \times 5.2}} \times \left(-\frac{5.2 \times 0.00448}{1.17^2}\right)\right)^2} = 0.33 \frac{\text{m}}{\text{s}} \quad (\text{D.19})$$

In this study, the largest manometer reading is $\Delta P = 0.0500 \text{ kPa}$ for $U_o = 9.2 \frac{\text{m}}{\text{s}}$.

$$W_{U_o} = \sqrt{\left(\sqrt{\frac{1.17}{2 \times 50}} \times \frac{1.27}{1.17}\right)^2 + \left(\sqrt{\frac{\rho 1.17}{2 \times 50}} \times \left(-\frac{50 \times 0.00448}{1.17^2}\right)\right)^2} = 0.12 \frac{\text{m}}{\text{s}} \quad (\text{D.20})$$

The digital calliper (Mitutoyo 500-171) resolution is 0.01 mm and the accuracy is $\pm 0.025 \text{ mm}$. The absolute uncertainty in diameter is:

$$(W_D)_{\text{Instrument error}} = \sqrt{(W_D)_{\text{Resolution}}^2 + (W_D)_{\text{Accuracy}}^2} \quad (\text{D.21})$$

$$(W_D)_{\text{Instrument error}} = \sqrt{\left(\frac{0.01}{2}\right)^2 + (0.025)^2} = 0.0255 \text{ mm} \quad (\text{D.22})$$

$$W_D = 0.0255 \text{ mm} \quad (\text{D.23})$$

For Re = 6700,

$$W_{Re} = \sqrt{\left(\frac{3 \times 0.0381}{1.82 \times 10^{-5}} \times 0.00448\right)^2 + \left(\frac{1.17 \times 0.0381}{1.82 \times 10^{-5}} \times 0.33\right)^2 + \left(\frac{1.17 \times 3}{1.82 \times 10^{-5}} \times 0.0000255\right)^2} \quad (D.24)$$

$$W_{Re} = \sqrt{(28.13)^2 + (808.26)^2 + (4.91)^2} = 808 \quad (D.25)$$

For Re = 12000,

$$W_{Re} = \sqrt{\left(\frac{9.2 \times 0.022}{1.82 \times 10^{-5}} \times 0.00448\right)^2 + \left(\frac{1.17 \times 0.022}{1.82 \times 10^{-5}} \times 0.12\right)^2 + \left(\frac{1.17 \times 9.2}{1.82 \times 10^{-5}} \times 0.0000255\right)^2} \quad (D.26)$$

$$W_{Re} = \sqrt{(49.82)^2 + (169.7)^2 + (15.8)^2} = 177 \quad (D.27)$$

D.2 Uncertainty in drag and lift coefficients (dynamic force measurement technique)

The drag and lift coefficients, C_D and C_L are calculated by:

$$C_D = \frac{F_D}{\frac{1}{2} \rho \times U_o^2 \times D \times l} \quad (D.28)$$

$$C_L = \frac{F_L}{\frac{1}{2} \rho \times U_o^2 \times D \times l} \quad (D.29)$$

the absolute uncertainty in drag and list coefficients are:

$$W_{C_D} = \sqrt{\left(\frac{\partial C_D}{\partial F_D} W_{F_D}\right)^2 + \left(\frac{\partial C_D}{\partial \rho} W_{\rho}\right)^2 + \left(\frac{\partial C_D}{\partial U_o} W_{U_o}\right)^2 + \left(\frac{\partial C_D}{\partial D} \times W_D\right)^2 + \left(\frac{\partial C_D}{\partial l} \times W_L\right)^2} \quad (D.30)$$

$$W_{C_D} =$$

$$\sqrt{\left(\frac{2}{\rho \times U_0^2 \times D \times l} W_F\right)^2 + \left(-\frac{2 \times F_D}{\rho^2 \times U_0^2 \times D \times l} W_\rho\right)^2 + \left(-\frac{4 \times F_D}{\rho \times U_0^3 \times D \times l} W_{U_0}\right)^2 + \left(\frac{2 \times F_D}{\rho \times U_0^2 \times D^2 \times l} \times W_D\right)^2 + \left(\frac{2 \times F_D}{\rho \times U_0^2 \times D \times l} \times W_l\right)^2}$$

(D.31)

$$W_{C_L} = \sqrt{\left(\frac{\partial C_L}{\partial F_L} W_F\right)^2 + \left(\frac{\partial C_L}{\partial \rho} W_\rho\right)^2 + \left(\frac{\partial C_L}{\partial U_0} W_{U_0}\right)^2 + \left(\frac{\partial C_L}{\partial D} \times W_D\right)^2 + \left(\frac{\partial C_L}{\partial L} \times W_L\right)^2}$$

(D.32)

$$W_{C_L} =$$

$$\sqrt{\left(\frac{2}{\rho \times U_0^2 \times D \times l} W_F\right)^2 + \left(-\frac{2 \times F_L}{\rho^2 \times U_0^2 \times D \times l} W_\rho\right)^2 + \left(-\frac{4 \times F_L}{\rho \times U_0^3 \times D \times l} W_{U_0}\right)^2 + \left(\frac{2 \times F_L}{\rho \times U_0^2 \times D^2 \times l} \times W_D\right)^2 + \left(\frac{2 \times L}{\rho \times U_0^2 \times D \times l} \times W_l\right)^2}$$

(D.33)

The first load cell (Gamma SI 32-2.5) accuracy is 0.04 % of the full scale (± 32 N) and the resolution is 1/160 N. The other load cell (Gamma SI 65-5) accuracy is 0.04% of the full scale (± 65 N) and the resolution is 1/80 N.

$$(W_{F(\text{Gamma SI } 32-2.5)})_{\text{Instrument}} = \sqrt{(W_{F(\text{Gamma SI } 32-2.5)})_{\text{Resolution}}^2 + (W_{F(\text{Gamma SI } 32-2.5)})_{\text{Accuracy}}^2}$$

(D.34)

$$(W_{F(\text{Gamma SI } 32-2.5)})_{\text{Instrument}} = \sqrt{\left(\frac{1}{320}\right)^2 + (.0004 \times 32)^2} = 0.0131 \text{ N}$$

(D.35)

$$(W_{F(\text{Gamma SI } 65-5)})_{\text{Instrument}} = \sqrt{(W_{F(\text{Gamma SI } 65-5)}^{\text{Resolution}})^2 + (W_{F(\text{Gamma SI } 65-5)}^{\text{Accuracy}})^2} \quad (\text{D.36})$$

$$(W_{F(\text{Gamma SI } 65-5)})_{\text{Instrument}} = \sqrt{\left(\frac{1}{160}\right)^2 + (.0004 \times 65)^2} = 0.0267 \text{ N} \quad (\text{D.37})$$

$$(W_{F(\text{Gamma SI } 32-2.5)}) = 0.0131 \text{ N} \quad (\text{D.38})$$

$$(W_{F(\text{Gamma SI } 65-5)}) = 0.0267 \text{ N} \quad (\text{D.39})$$

$$(W_F) = 0.02 \text{ N} \quad (\text{D.40})$$

After neglecting the uncertainty of the cylinder length, for $U_o = 3.0 \frac{m}{s}$, $D = 0.0381 \text{ m}$, $L = 0.657$, $Re = 6700$, $F_D = 0.12 \text{ N}$, $F_L = 0.045 \text{ N}$, the absolute uncertainty is:

$$W_{C_D} = \sqrt{\left(\frac{2}{1.17 \times 3^2 \times 0.0381 \times 0.657} \times 0.02\right)^2 + \left(-\frac{2 \times 0.12}{1.17^2 \times 3^2 \times 0.0381 \times 0.657} \times 0.00448\right)^2 + \left(-\frac{4 \times 0.12}{1.17 \times 3^3 \times 0.0381 \times 0.657} \times 0.33\right)^2} \quad (\text{D.41})$$

$$W_{C_D} = 0.25 \quad (\text{D.42})$$

$$W_{C_L} = \sqrt{\left(\frac{2}{1.17 \times 3^2 \times 0.0381 \times 0.657} \times 0.02\right)^2 + \left(-\frac{2 \times 0.045}{1.17^2 \times 3^2 \times 0.0381 \times 0.657} \times 0.00448\right)^2 + \left(-\frac{4 \times 0.045}{1.17 \times 3^3 \times 0.0381 \times 0.657} \times 0.33\right)^2}$$

(D.43)

$$W_{C_L} = 0.17$$

(D.44)

After neglecting the uncertainty of the cylinder length, for $U_o = 9.2 \frac{m}{s}$, $D = 0.0220$ m, $L = 0.657$, $Re = 12000$, $F_D = 0.96$ N, $F_L = 0.21$ N the absolute uncertainty is:

$$W_{C_D} = \sqrt{\left(\frac{2}{1.17 \times 9.2^2 \times 0.022 \times 0.657} \times 0.02\right)^2 + \left(-\frac{2 \times 0.96}{1.17^2 \times 9.2^2 \times 0.022 \times 0.657} \times 0.00448\right)^2 + \left(-\frac{4 \times 0.96}{1.17 \times 9.2^3 \times 0.022 \times 0.657} \times 0.12\right)^2}$$

(D.45)

$$W_{C_D} = 0.004$$

(D.46)

W_{C_L}

$$= \sqrt{\left(\frac{2}{1.17 \times 9.2^2 \times 0.022 \times 0.657} \times 0.02\right)^2 + \left(-\frac{2 \times 0.21}{1.17^2 \times 9.2^2 \times 0.022 \times 0.657} \times 0.00448\right)^2 + \left(-\frac{4 \times 0.21}{1.17 \times 9.2^3 \times 0.022 \times 0.657} \times 0.12\right)^2}$$

(D.47)

$$W_{C_L} = 0.023$$

(D.48)

D.3 Uncertainty in drag and lift coefficient (pressure measurement technique)

The drag and lift coefficients, C_D and C_L are calculated by:

$$C_D = -\frac{\pi}{n} \sum_{i=1}^n (C_{P_i} \cos \theta_i) \quad (D.49)$$

$$C_L = -\frac{\pi}{n} \sum_{i=1}^n (C_{P_i} \sin \theta_i) \quad (D.50)$$

where n is the number of pressure readings around the cylinder.

The absolute uncertainty in drag coefficient is:

$$W_{C_D} = \sum_{i=1}^n \sqrt{\left(\frac{\partial C_{D_i}}{\partial C_{P_i}} W_{C_{P_i}}\right)^2 + \left(\frac{\partial C_{D_i}}{\partial C_{\theta_i}} W_{\theta_i}\right)^2} \quad (D.51)$$

where,

$$\frac{\partial C_{D_i}}{\partial C_{P_i}} = -\frac{\pi}{n} \cos \theta_i \quad (D.52)$$

$$\frac{\partial C_{D_i}}{\partial C_{\theta_i}} = -\frac{\pi}{n} \times C_{P_i} \times -\sin \theta_i \quad (D.53)$$

Substituting Equations (C.52) and (C.53) into Equation (C.51),

$$W_{C_D} = \sum_{i=1}^n \sqrt{\left(-\frac{\pi}{n} \times \cos \theta_i \times W_{C_{P_i}}\right)^2 + \left(-\frac{\pi}{n} \times C_{P_i} \times -\sin \theta_i \times W_{\theta_i}\right)^2} \quad (D.54)$$

The absolute uncertainty in lift coefficient is:

$$W_{C_L} = \sum_{i=1}^n \sqrt{\left(\frac{\partial C_{L_i}}{\partial C_{P_i}} W_{C_{P_i}}\right)^2 + \left(\frac{\partial C_{L_i}}{\partial C_{\theta_i}} W_{\theta_i}\right)^2} \quad (D.55)$$

where,

$$\frac{\partial C_{L_i}}{\partial C_{P_i}} = -\frac{\pi}{n} \sin \theta_i \quad (D.56)$$

$$\frac{\partial C_{L_i}}{\partial C_{\theta_i}} = -\frac{\pi}{n} \times C_{P_i} \times \cos \theta_i \quad (D.57)$$

Substituting Equations (D.56) and (D.57) into Equation (D.55),

$$W_{C_L} = \sum_{i=1}^N \sqrt{\left(-\frac{\pi}{n} \times \sin\theta_i \times W_{C_{P_i}}\right)^2 + \left(-\frac{\pi}{n} \times C_{P_i} \times \cos\theta_i \times W_{\theta_i}\right)^2} \quad (D.58)$$

The mean pressure coefficient, $C_P(\theta)$, is defined as:

$$C_P = \frac{\Delta P}{\frac{1}{2} \times \rho \times U_o^2} \quad (D.59)$$

The absolute uncertainty in pressure coefficient:

$$W_{C_{P_i}} = \sqrt{\left(\frac{\partial C_{P_i}}{\partial \Delta P_i} W_{\Delta P_i}\right)^2 + \left(\frac{\partial C_{P_i}}{\partial U_o} W_{U_o}\right)^2 + \left(\frac{\partial C_{P_i}}{\partial \rho} W_{\rho}\right)^2} \quad (D.60)$$

where,

$$\frac{\partial C_{P_i}}{\partial \Delta P_i} = \frac{2}{\rho \times U_o^2} \quad (D.61)$$

$$\frac{\partial C_{P_i}}{\partial U_o} = \frac{-4 \times C_{P_i}}{\rho \times U_o^3} \quad (D.62)$$

$$\frac{\partial C_{P_i}}{\partial \rho} = \frac{2 \times \Delta P_i}{\rho^2 \times U_o^2} \quad (D.63)$$

Substituting Equations (D.61) and (D.62), and (D.63) into Equation (D.60), for $U_o = 3.0$

$\frac{m}{s}$:

$$W_{C_{P_i}} = \sqrt{\left(\frac{2}{1.17 \times 3^2} \times 1.27\right)^2 + \left(\frac{-4 \times C_{P_i}}{1.17 \times 3^3} \times 0.33\right)^2 + \left(\frac{2 \times \Delta P_i}{1.17^2 \times 3^2} \times 0.00448\right)^2} \quad (D.64)$$

$$W_{C_P} = \sum_{i=1}^N W_{C_{P_i}} = 0.25 \quad (D.65)$$

Substituting Equations (D.61), (D.62), and (D.63) into Equation (D.60), for $U_o = 9.2 \frac{m}{s}$:

$$W_{C_{P_i}} = \sqrt{\left(\frac{2}{1.17 \times 9.2^2} \times 1.27\right)^2 + \left(\frac{-4 \times C_{P_i}}{1.17 \times 9.2^3} \times 0.12\right)^2 + \left(\frac{2 \times \Delta P_i}{1.17^2 \times 9.2^2} \times 0.00448\right)^2} \quad (D.66)$$

$$W_{C_P} = \sum_{i=1}^N W_{C_{P_i}} = 0.025 \quad (D.67)$$

The azimuth angle is measured by protractor. The protractor has a resolution of $\pm 2^\circ$ and an accuracy of $\pm 2^\circ$. The absolute uncertainty in azimuth angle,

$$(W_{\theta_i})_{\text{Instrument error}} = \sqrt{(W_{\theta_i})_{\text{Resolution}}^2 + (W_{\theta_i})_{\text{Accuracy}}^2} \quad (D.68)$$

$$(W_{\theta_i})_{\text{Instrument error}} = \sqrt{\left(\frac{2}{360}\right)^2 + \left(\frac{2}{360}\right)^2} \quad (D.69)$$

$$(W_{\theta_i})_{\text{Instrument error}} = 0.008 \quad (D.70)$$

Substituting Equations (D.55) and (D.70) into Equation (D.54), and (C.58), for $U_o = 3.0 \frac{m}{s}$,

$$W_{C_D} = 0.03 \quad (D.71)$$

$$W_{C_L} = 0.03 \quad (D.72)$$

Substituting Equations (D.55) and (D.70) into Equation (D.54), and (D.58) for $U_o = 9.2 \frac{m}{s}$,

$$W_{C_D} = 0.003 \quad (D.73)$$

$$W_{C_L} = 0.003 \quad (D.74)$$

D.4 Uncertainty in turbulence intensity

The turbulence intensity, Tu, is obtained from:

$$\text{Tu}\% = \frac{u_{\text{rms}}}{\bar{U}} \times 100 \quad (\text{D.75})$$

The absolute uncertainty in turbulence intensity:

$$W_{\text{Tu}} = \sqrt{\left(\frac{\partial \text{Tu}}{\partial u_{\text{rms}}} W_{u_{\text{rms}}}\right)^2 + \left(\frac{\partial \text{Tu}}{\partial \bar{U}} W_{\bar{U}}\right)^2} \quad (\text{D.76})$$

Where,

$$\frac{\partial \text{Tu}}{\partial u_{\text{rms}}} = \frac{100}{\bar{U}} \quad (\text{D.77})$$

$$\frac{\partial \text{Tu}}{\partial \bar{U}} = -\frac{u_{\text{rms}}}{(\bar{U})^2} \times 100 \quad (\text{D.78})$$

Substituting Equations (D.77) and (D.78) into Equation (D.76),

$$W_{\text{Tu}} = \sqrt{\left(\frac{100}{\bar{U}} \times W_{u_{\text{rms}}}\right)^2 + \left(-\frac{u_{\text{rms}}}{(\bar{U})^2} \times 100 \times W_{\bar{U}}\right)^2} \quad (\text{D.79})$$

The time-average velocity, \bar{U} , is calculated:

$$\bar{U} = \frac{1}{N} \sum_{i=1}^N U_i \quad (\text{D.80})$$

The uncertainty in time-average velocity is estimated:

$$W_{\bar{U}} = \frac{1}{N} \sqrt{\sum_{i=1}^N (W_{U_i})^2} \quad (\text{D.81})$$

The root mean square of velocity value is calculated as:

$$u_{\text{rms}} = \sqrt{\frac{1}{N} \sum_{i=1}^N (U_i - \bar{U})^2} \quad (\text{D.82})$$

The uncertainty in root mean square of velocity value is estimated:

$$W_{u_{rms}} = \sqrt{\left(\frac{\partial u_{rms}}{\partial U_i} W_{U_i}\right)^2 + \left(\frac{\partial u_{rms}}{\partial \bar{U}} W_{\bar{U}}\right)^2} \quad (D.83)$$

where,

$$\frac{\partial u_{rms}}{\partial U_i} = \frac{\sum_{i=1}^N (U_i - \bar{U})^2}{N \times \sqrt{\frac{1}{N} \sum_{i=1}^N (U_i - \bar{U})^2}} \quad (D.84)$$

$$\frac{\partial u_{rms}}{\partial \bar{U}} = - \frac{\sum_{i=1}^N (U_i - \bar{U})^2}{N \times \sqrt{\frac{1}{N} \sum_{i=1}^N (U_i - \bar{U})^2}} \quad (D.85)$$

Substituting Equations (D.84) and (D.85) into Equation (D.83),

$$W_{u_{rms}} = \sqrt{\left(\frac{\sum_{i=1}^N (U_i - \bar{U})^2}{N \times \sqrt{\frac{1}{N} \sum_{i=1}^N (U_i - \bar{U})^2}}\right)^2 \times ((W_{U_i})^2 + (W_{\bar{U}})^2)} \quad (D.86)$$

The uncertainty in time-average velocity and root mean square of value depends on the uncertainty in instantaneous velocity, U_i . Thus the uncertainty of this parameter should be found.

The absolute uncertainty in instantaneous velocity is:

$$W_{U_i} = W_{U_{eff}} = \sqrt{(W_{U_{eff}})_{\text{Calibration}} + (W_{U_{eff}})_{\text{Data aquisition}}} \quad (D.87)$$

From the Dantec manual, the uncertainty in the calibration is 1%. The uncertainty in the data acquisition depends on the digitization uncertainty from digitizing, and the uncertainty from the probe positioning. The uncertainty from the Dantec manual the uncertainty in probe position is equal to 0.000087 m/s which is very small and could be neglected. The uncertainty in the digitized hot-wire anemometer output voltage is ± 0.5 of the least significant bit for the 12 bits A/D with an input range set as 0 to 10V, [D1]:

$$w_E = \frac{0.5 \times 10}{2^{12}} = 0.0012V \quad (D.88)$$

The digitizing uncertainty in the effective velocity is:

$$(W_{U_{\text{eff}}})_{\text{Digitalizer}} = \frac{W_E}{U_{\text{eff}}} \times \frac{dU_{\text{eff}}}{dE_i} \quad (\text{D.89})$$

where,

$$U_{\text{eff}} = C_0 + C_1 E_i^1 + C_2 E_i^2 + C_3 E_i^3 + C_4 E_i^4 \quad (\text{D.90})$$

$$\frac{dU_{\text{eff}}}{dE_i} = C_1 + C_2 \times E_i + C_3 \times E_i^2 + C_4 \times E_i^3 \quad (\text{D.91})$$

Thus,

$$(W_{U_{\text{eff}}})_{\text{Data aquisition}} = \sqrt{(W_{U_{\text{eff}}})_{\text{Digitalizer}}^2} \quad (\text{D.92})$$

Substituting Equations (D.88) and (D.90) and (D.91) into Equation (D.87),

$$W_{U_i} = W_{U_{\text{eff}}} = \sqrt{(0.01)^2 + \left(\frac{0.0012}{U_{\text{eff}}} \times (C_1 + C_2 \times E_i + C_3 \times E_i^2 + C_4 \times E_i^3)\right)^2} \quad (\text{C.93})$$

In this study, the maximum uncertainty in turbulence intensity is estimated by using a MatLab program and the absolute value is $\pm 0.5\%$ (absolute). Also, the maximum uncertainty in integral length scale is calculated using a MatLab program and it is found to be 12%.

REFERENCES

[D1] “Streamline_streamware installation and users guide,” Dantec dynamics, Denmark, 2000.

APPENDIX E: Force measurement results

This Appendix includes the dynamic force measurement results, which are in the good agreement with the pressure measurement results. The effect of turbulence intensity ($0.5 \lesssim Tu \lesssim 10\%$) on the drag and lift coefficients of the upstream and downstream cylinders when $0.56 \lesssim \Lambda/D \lesssim 1.28$ in three different Re values (Re = 6700, 9200, and 12000) using the dynamic force measurement techniques, are shown in Fig. 51 and Fig. 52. Also, the effect of integral length scale ($0.56 \lesssim \Lambda/D \lesssim 1.28$) on the drag and lift coefficients of the upstream and downstream cylinders when $6.7 \times 10^3 \lesssim Re \lesssim 1.2 \times 10^4$ at three different turbulence intensities (Tu = 4%, 7%, and 10%), can be inspected from the dynamic force measurement results, which can be found in Fig. 53 and Fig. 54. Since the uncertainty in dynamic force measurement (0.25) is higher than the uncertainty in pressure measurement (0.03), the drag and lift coefficients obtained by the dynamic force measurement are less reliable.

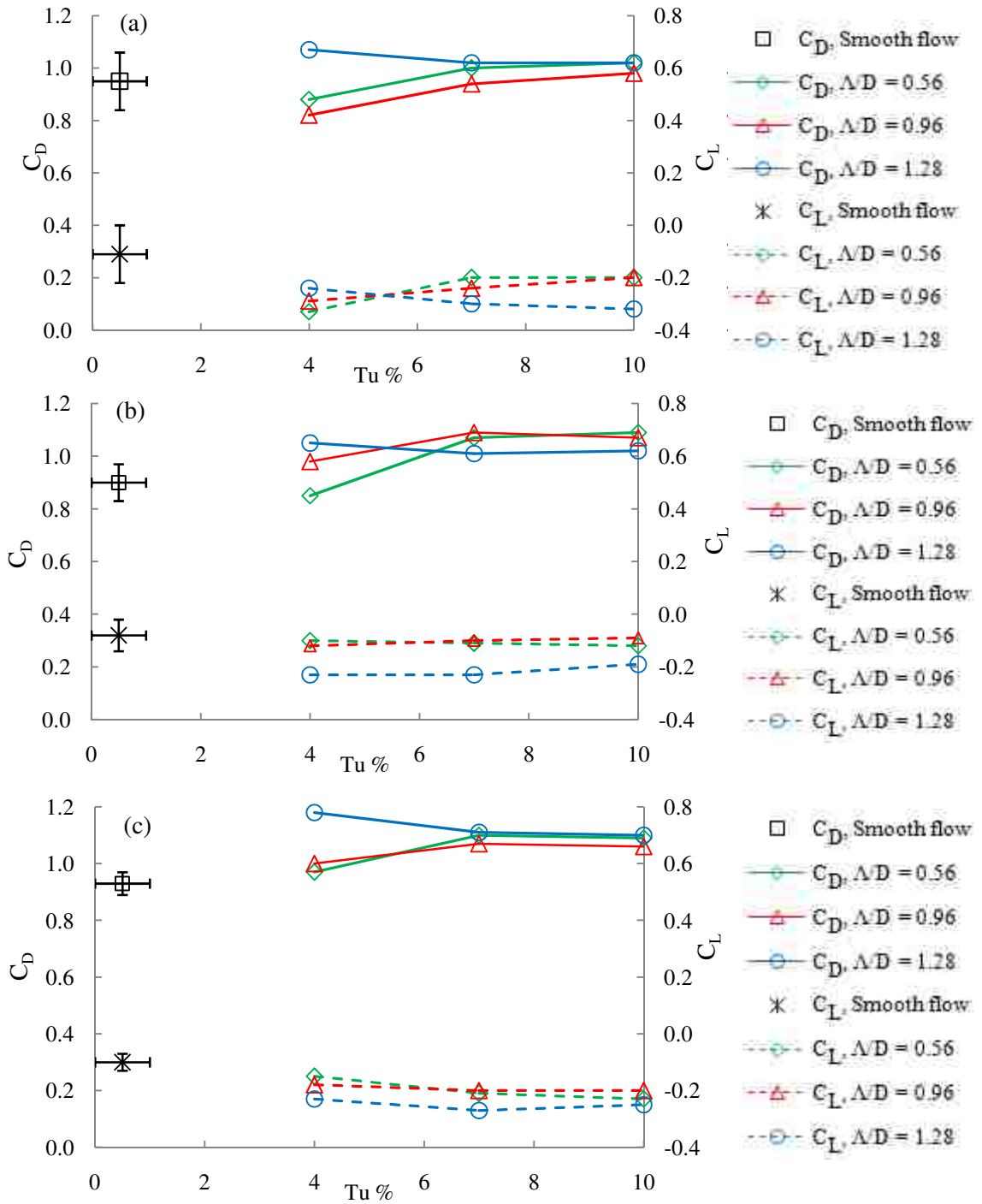


Fig. 51 Tu effects on the upstream cylinder (a) $Re = 6700$, (b) $Re = 9200$, and (c) $Re = 12000$, force measurement technique.

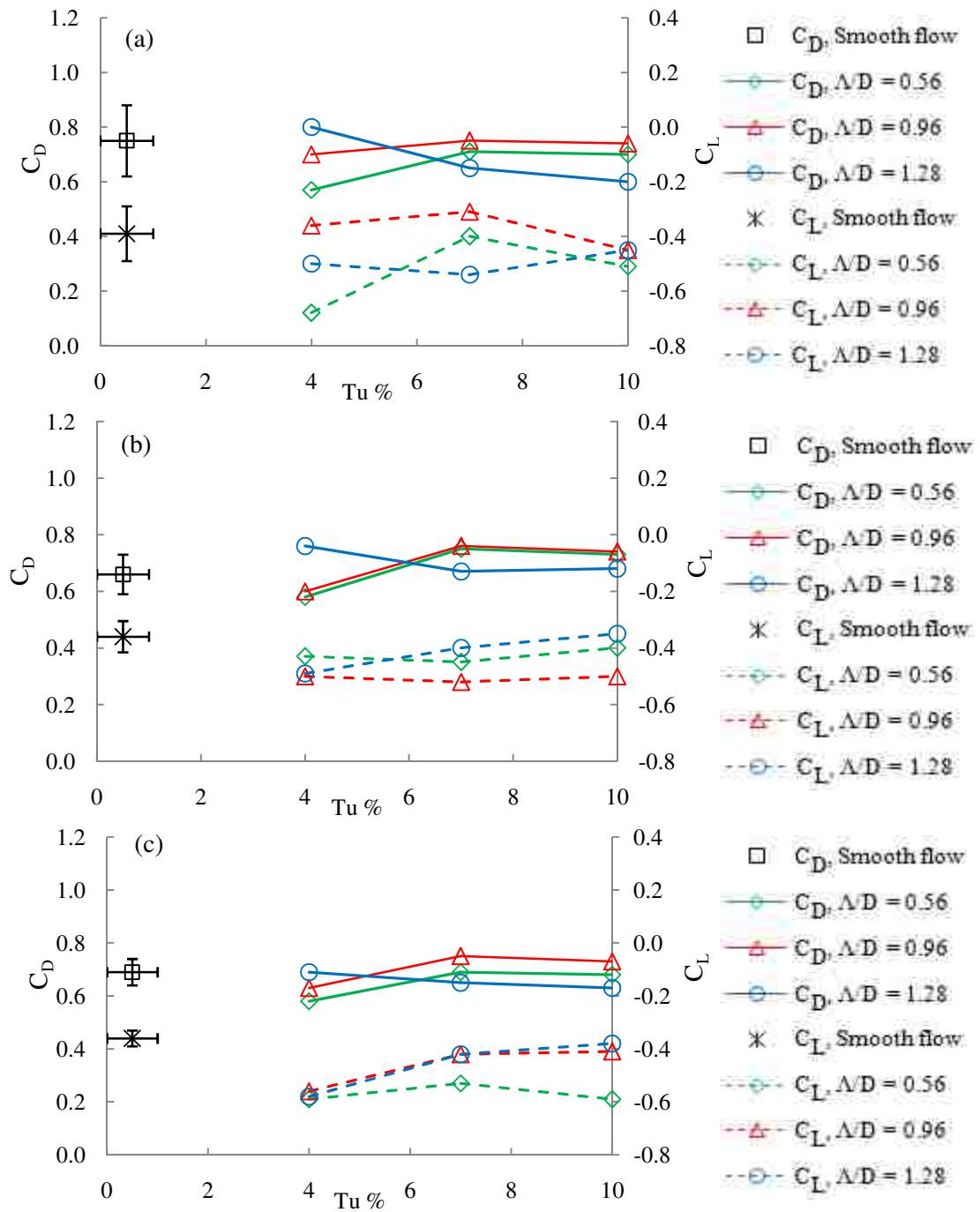


Fig. 52 Tu effects on the downstream cylinder (a) $Re = 6700$, (b) $Re = 9200$, and (c) $Re = 12000$, force measurement technique.

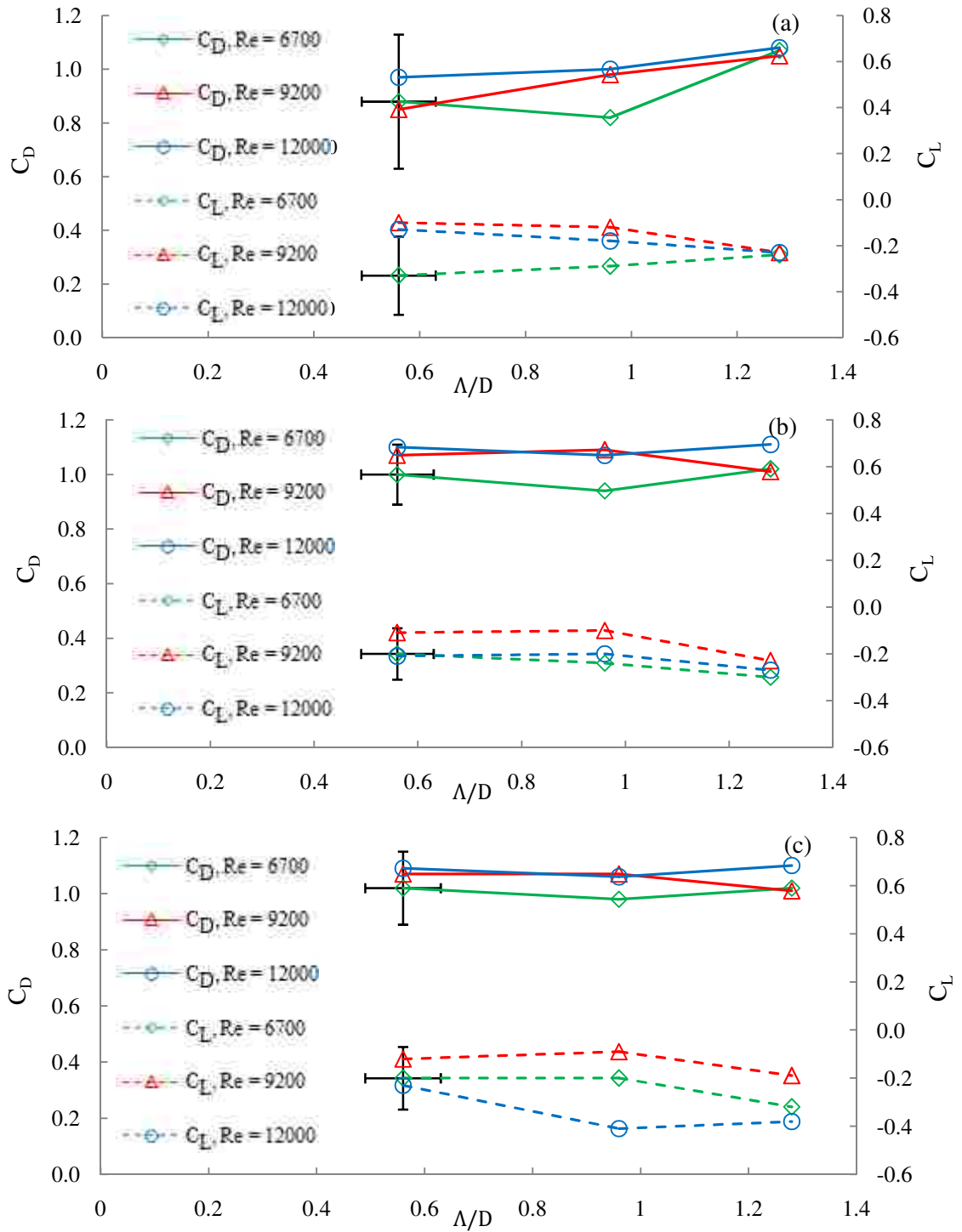


Fig. 53 Λ/D effects on the upstream cylinder (a) $Tu = 4\%$, (b) $Tu = 7\%$, and (c) $Tu = 10\%$, force measurement technique.

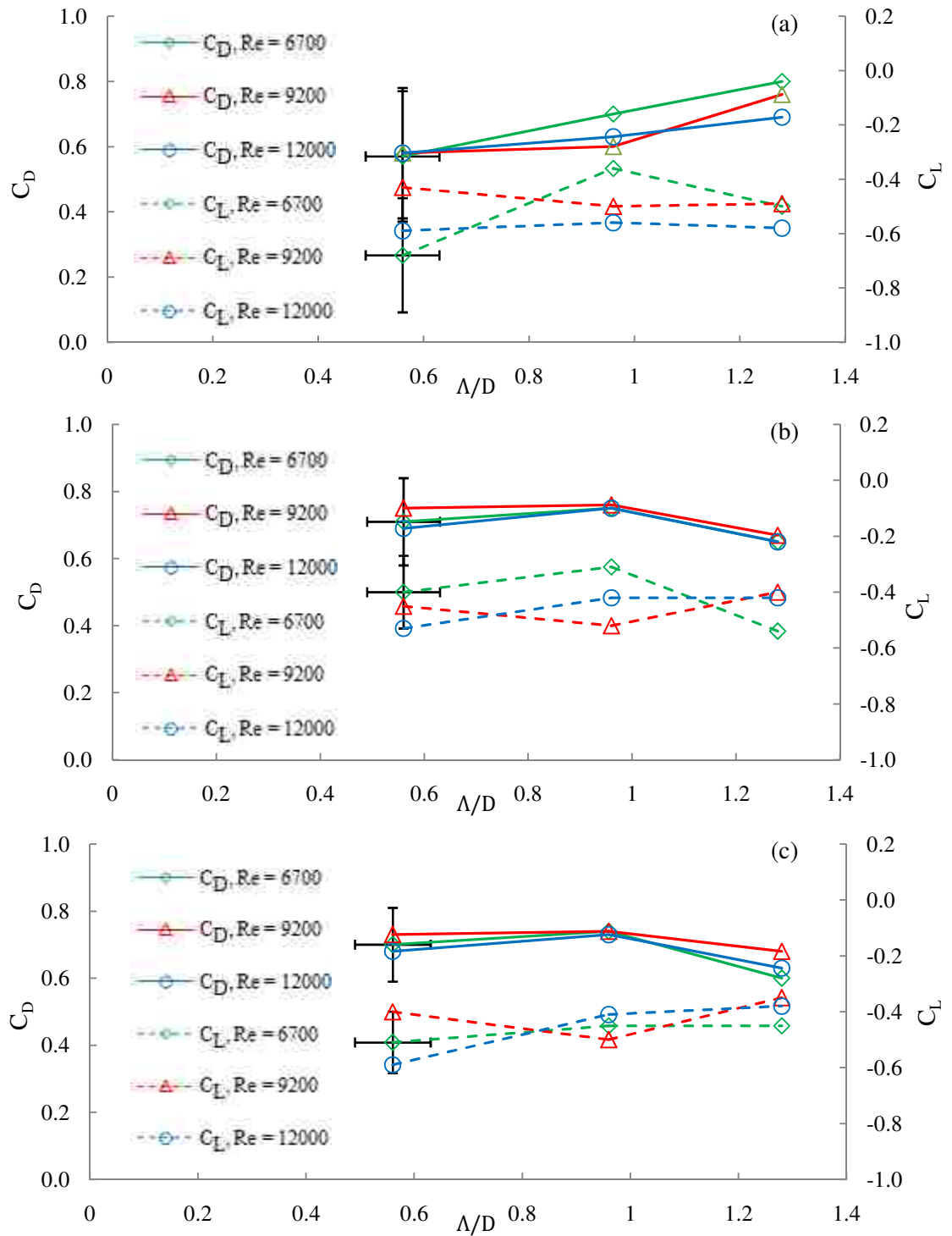


Fig. 54 Λ/D effects on the upstream cylinder (a) $Tu = 4\%$, (b) $Tu = 7\%$, and (c) $Tu = 10\%$, force measurement technique.

APPENDIX F: Effect of turbulence on velocity, turbulence intensity, and root mean square of velocity profiles

Figure 55 to 63 show the profiles of the normalized stream-wise mean velocity, the turbulence intensity, and root mean square of velocity profiles in term of y/D . The measurements occurred across the wake at $X/D = 2$ for $Tu = 0.5\%$, 4% , 7% , and 10% and $\Lambda/D = 0.56, 0.96,$ and 1.28 in $6.7 \times 10^3 \lesssim Re \lesssim 1.2 \times 10^4$.

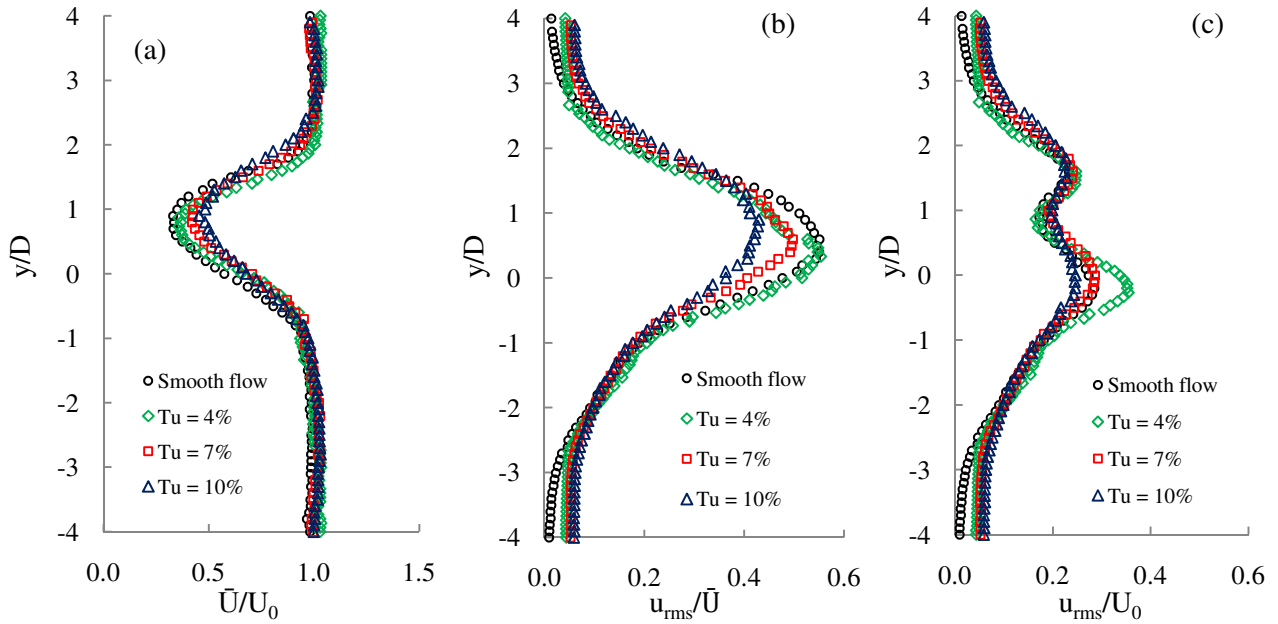


Fig. 55 Stream-wise mean velocity, turbulent intensity, and root mean square of velocity profiles at $Re = 6700$ and $\Lambda/D = 0.56$ (a) mean velocity, (b) turbulence intensity, and (c) root mean square of velocity.

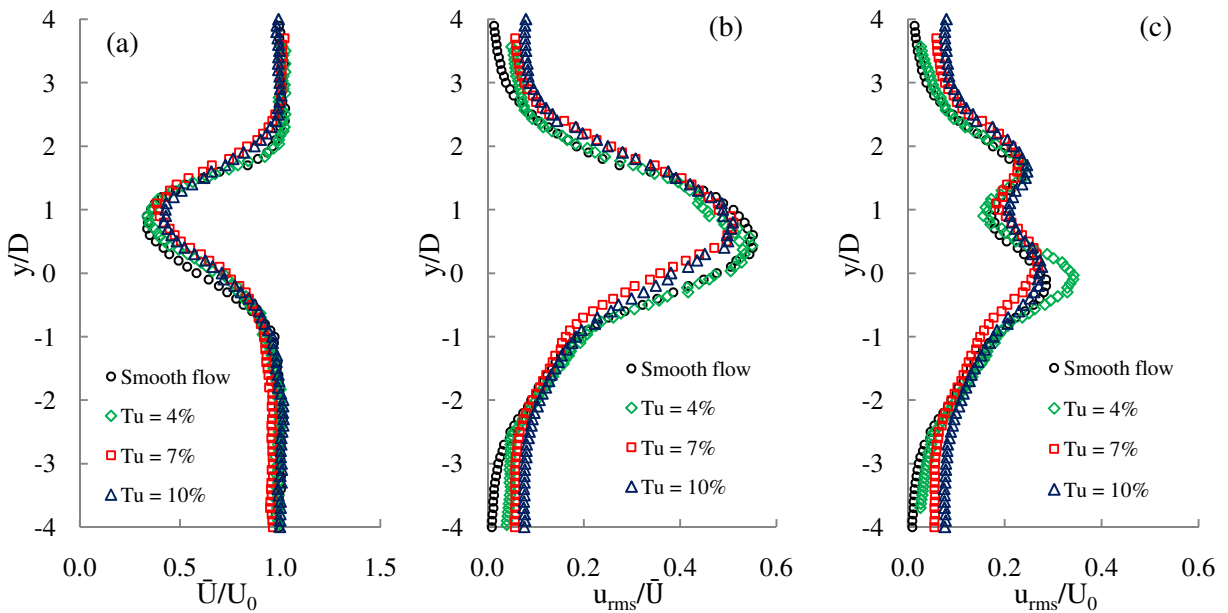


Fig. 56 Stream-wise mean velocity, turbulence intensity, and root mean square of velocity profiles at $Re = 6700$ and $\Lambda/D = 0.96$ (a) mean velocity, (b) turbulence intensity, and (c)

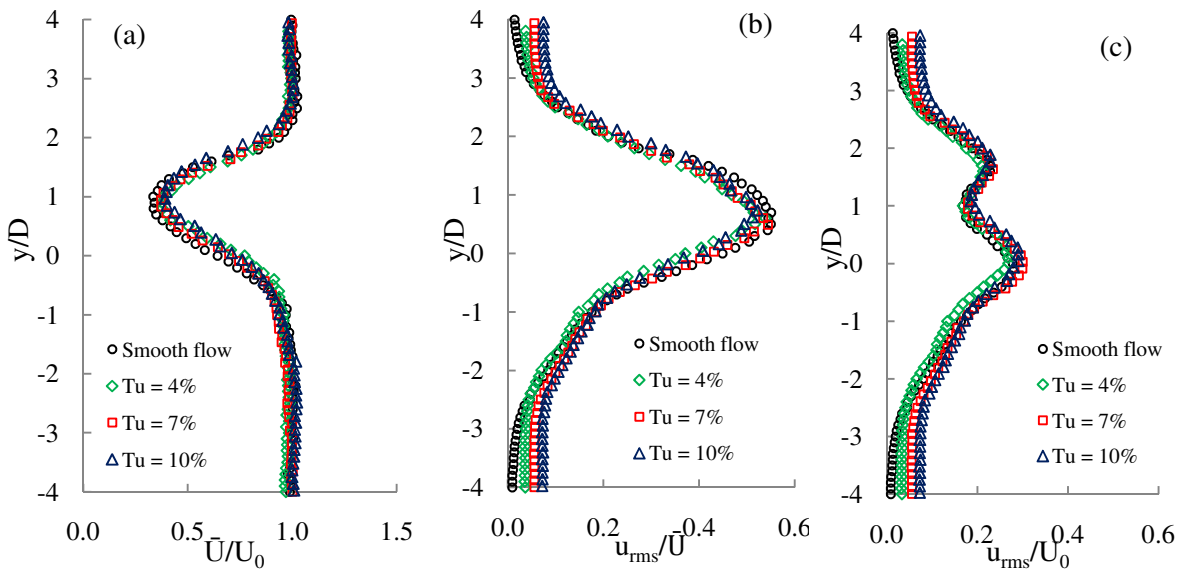


Fig. 57 Stream-wise mean velocity, turbulence intensity, and root mean square of velocity profiles at $Re = 6700$ and $\Lambda/D = 1.28$ (a) mean velocity, (b) turbulence intensity, and (c) root mean square of velocity.

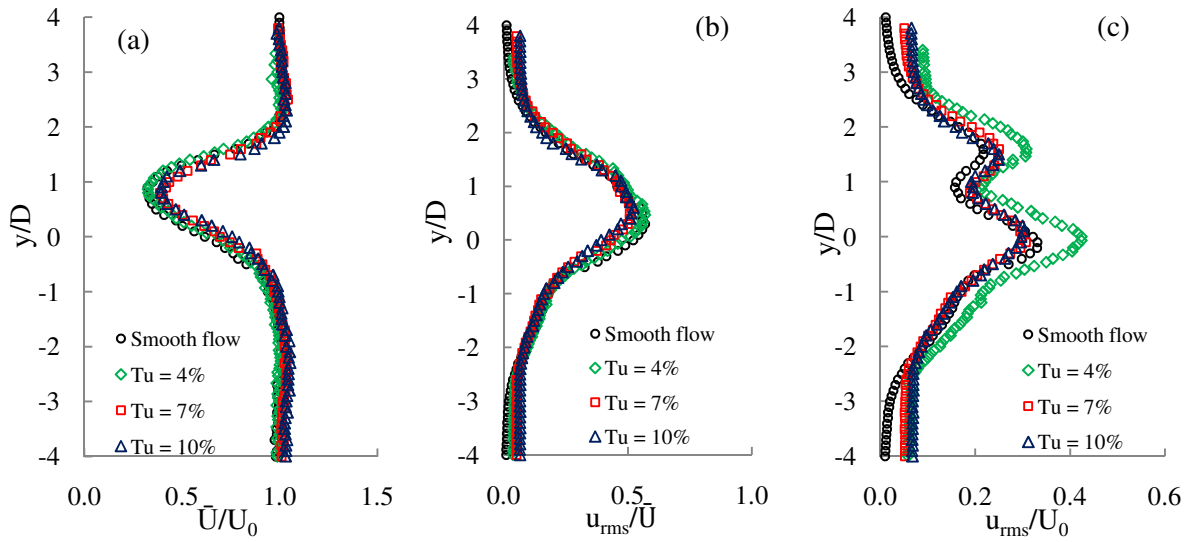


Fig. 58 Stream-wise mean velocity, turbulent intensity, and root mean square of velocity profiles at $Re = 9200$ and $\Lambda/D = 0.56$ (a) mean velocity, (b) turbulence intensity, and (c)

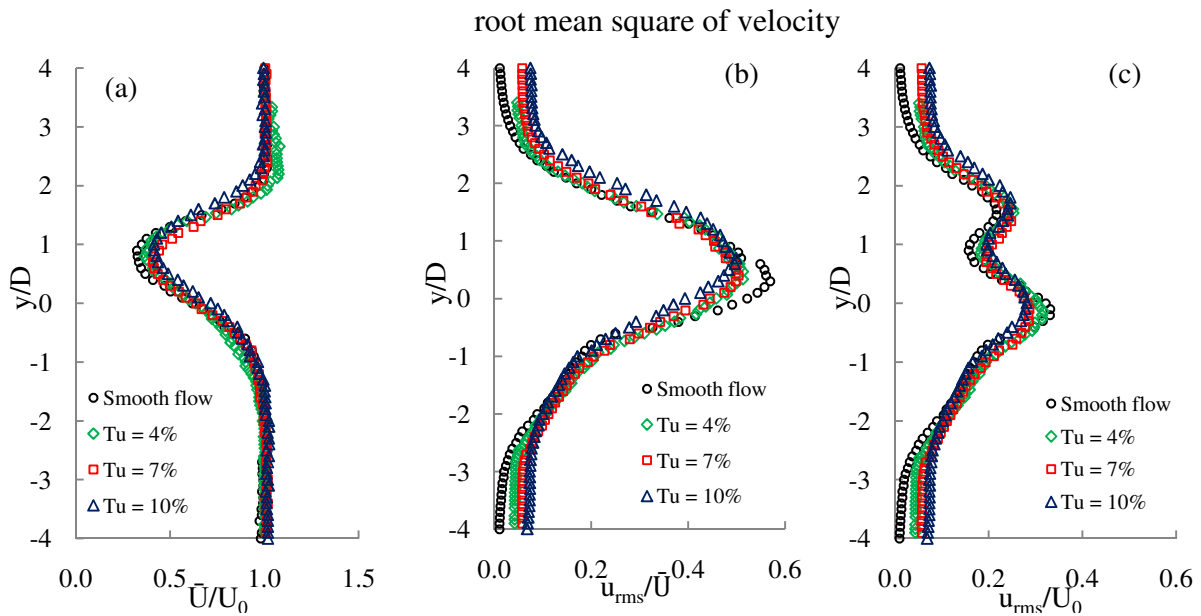


Fig. 59 Stream-wise mean velocity, turbulent intensity, and root mean square of velocity profiles at $Re = 9200$ and $\Lambda/D = 0.96$ (a) mean velocity, (b) turbulence intensity, and (c)

root mean square of velocity.

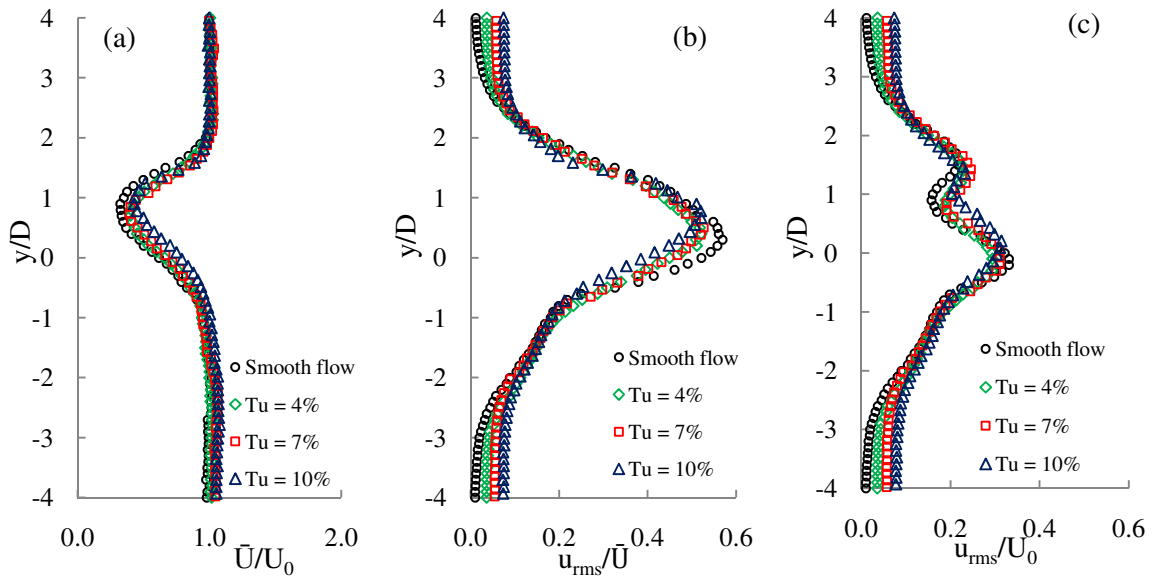


Fig. 60 Stream-wise mean velocity, turbulence intensity, and root mean square of velocity profiles at $Re = 9200$ and $\Lambda/D = 1.28$ (a) mean velocity, (b) turbulence intensity, and (c)

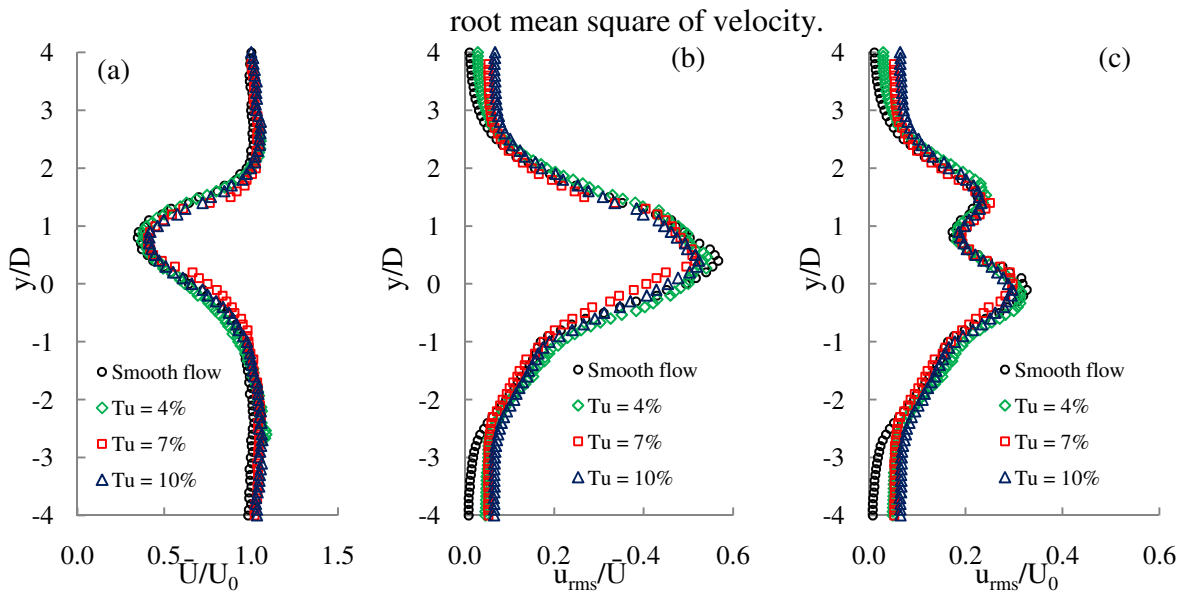


Fig. 61 Stream-wise mean velocity, turbulence intensity, and root mean square of velocity profiles at $Re = 12000$ and $\Lambda/D = 0.56$ (a) mean velocity, (b) turbulence intensity, and (c) root mean square of velocity.

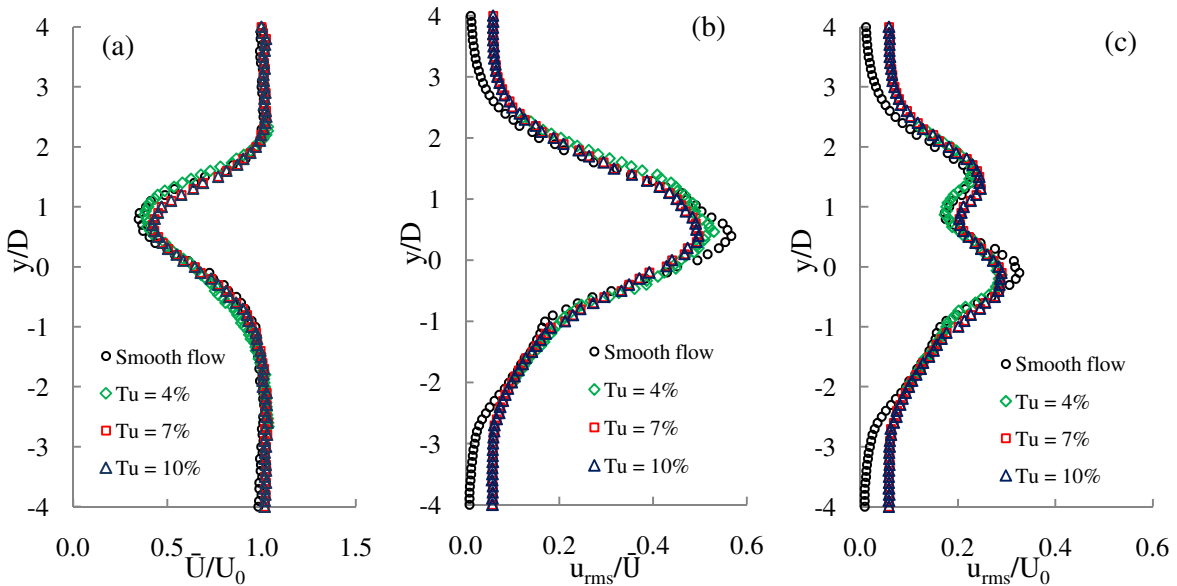


Fig. 62 Stream-wise mean velocity, turbulence intensity, and root mean square of velocity profiles at $Re = 12000$ and $\Lambda/D = 0.96$ (a) mean velocity, (b) turbulence intensity, and (c) root mean square of velocity.

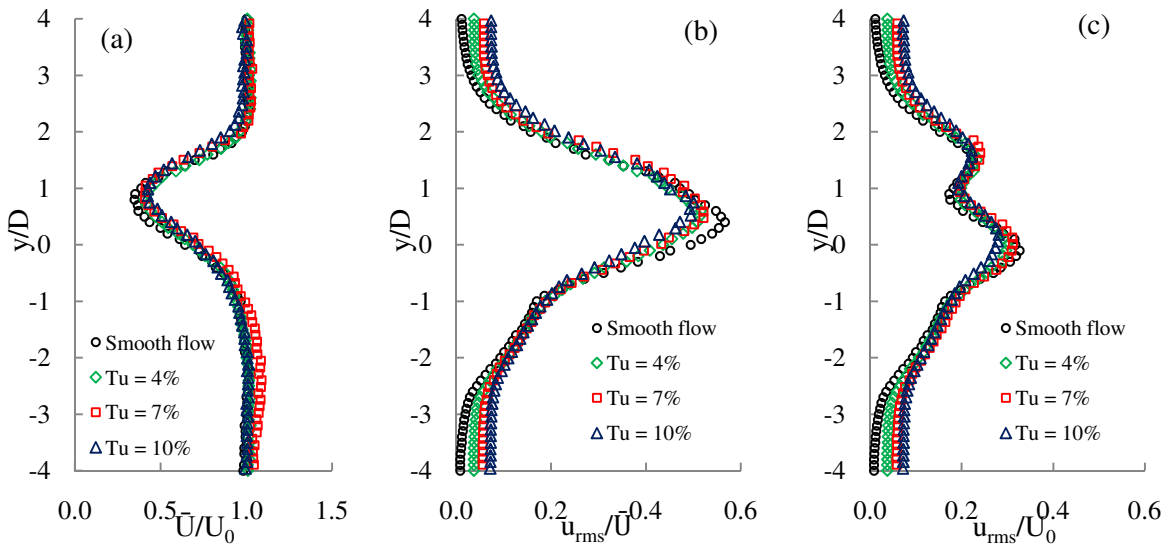


Fig. 63 Stream-wise mean velocity, turbulence intensity, and root mean square of velocity profiles at $Re = 12000$ and $\Lambda/D = 1.28$ (a) mean velocity, (b) turbulence intensity, and (c) root mean square of velocity.

APPENDIX G: Effect of Reynolds number on the pressure distributions around the upstream and downstream cylinders

Figure 64 to 72 show the pressure distribution around the upstream and downstream cylinders for $Tu = 0.5\%$, 4% , 7% , and 10% and $\Lambda/D = 0.56$, 0.96 , and 1.28 in $6.7 \times 10^3 \lesssim Re \lesssim 1.2 \times 10^4$.

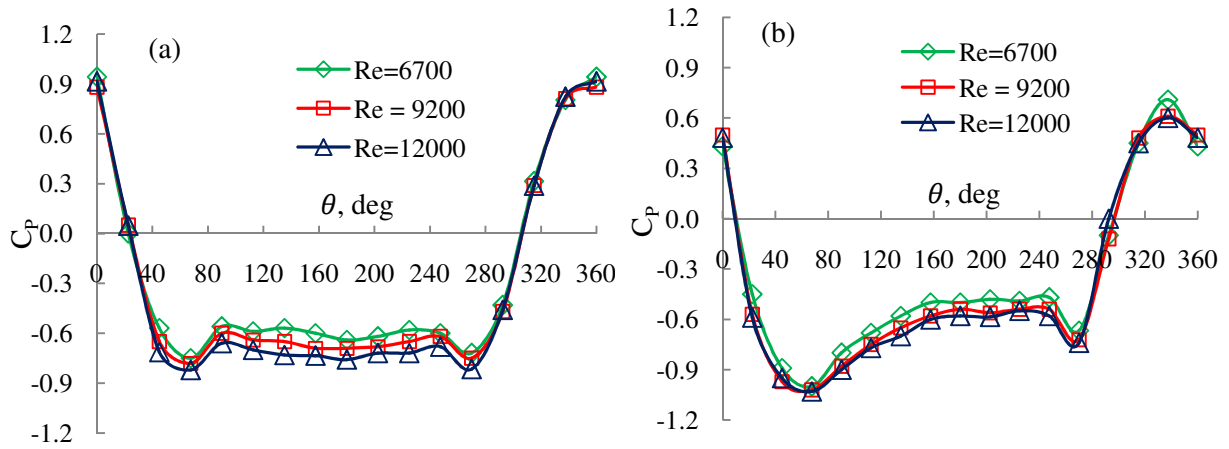


Fig. 64 Pressure distribution at $Tu = 4\%$, and $\Lambda/D = 0.56$ around (a) upstream cylinder, and (b) downstream cylinder.

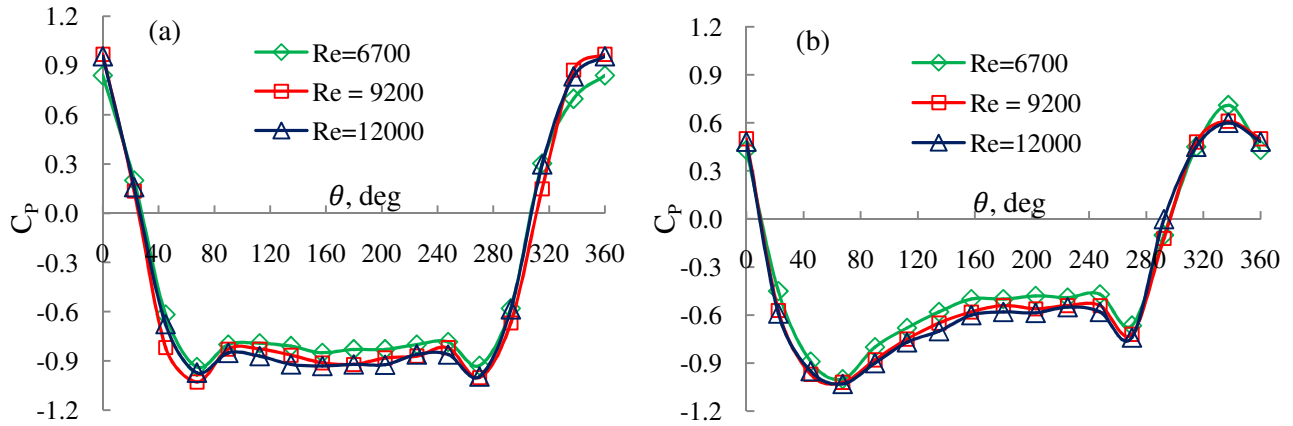


Fig. 65 Pressure distribution at $Tu = 7\%$, and $\Lambda/D = 0.56$ around (a) upstream cylinder, and (b) downstream cylinder.

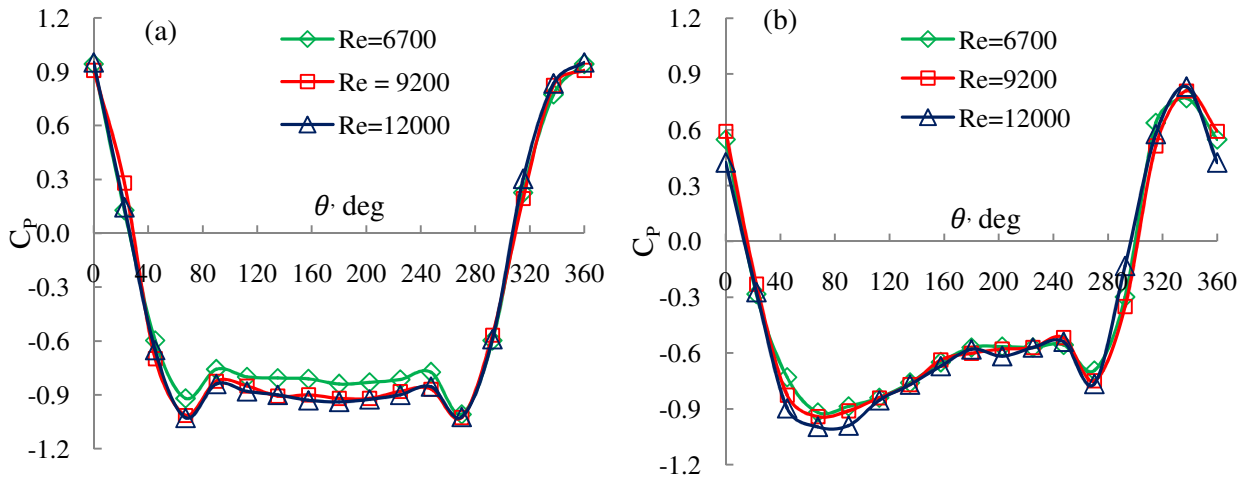


Fig. 66 Pressure distribution at $Tu = 10\%$, and $\Lambda/D = 0.56$ around (a) upstream cylinder, and (b) downstream cylinder.

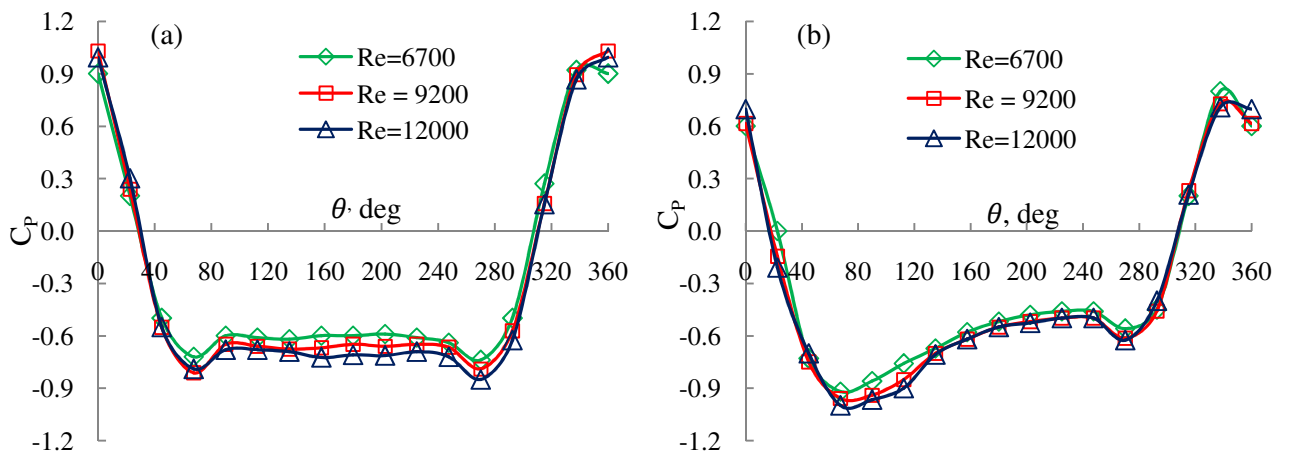


Fig. 67 Pressure distribution at $Tu = 4\%$, and $\Lambda/D = 0.96$ around: (a) upstream cylinder, and (b) downstream cylinder.

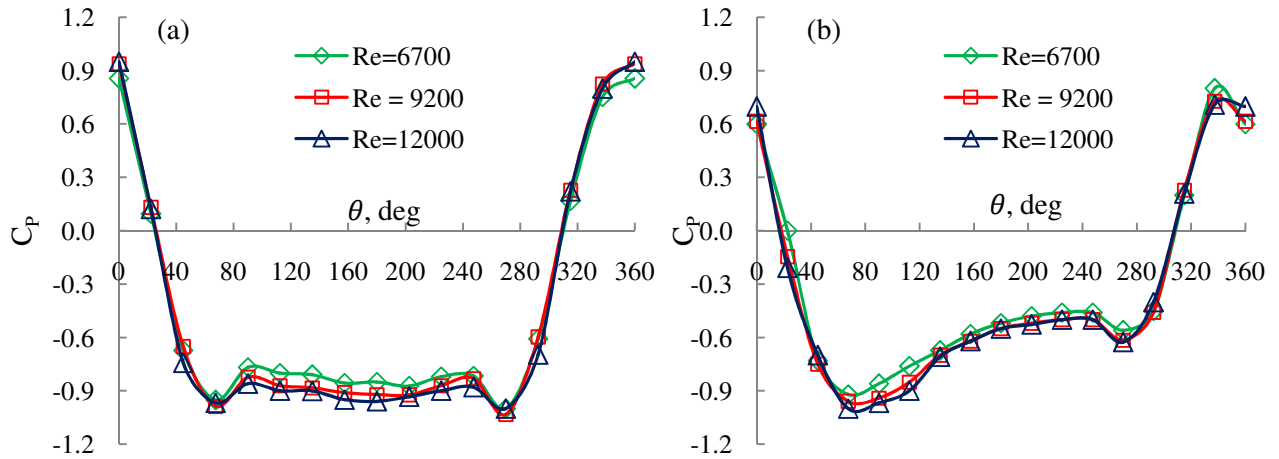


Fig. 68 Pressure distribution at $Tu = 7\%$, and $\Lambda/D = 0.96$ around (a) upstream cylinder, and (b) downstream cylinder.

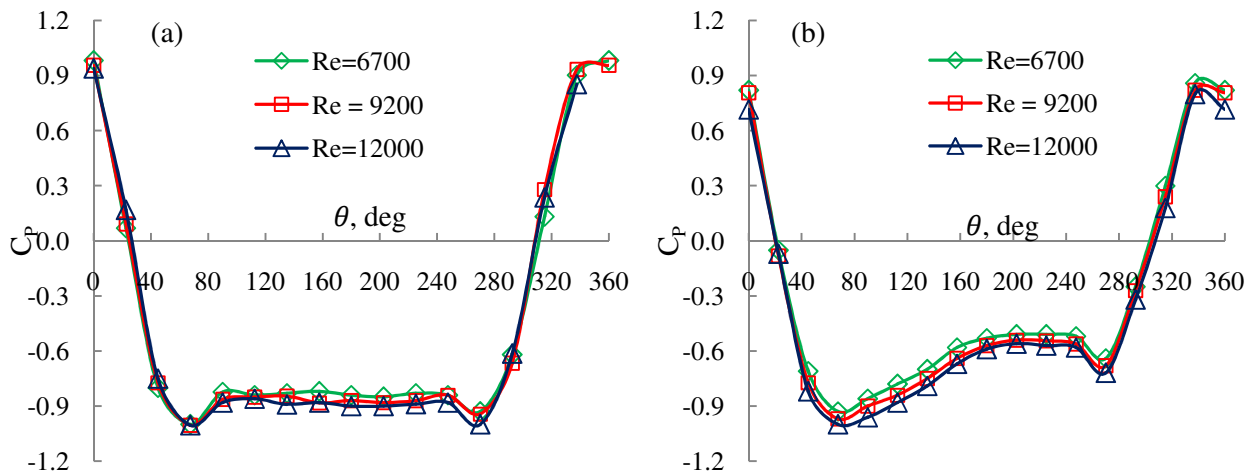


Fig. 69 Pressure distribution at $Tu = 10\%$, and $\Lambda/D = 0.96$ around (a) upstream cylinder, and (b) downstream cylinder.

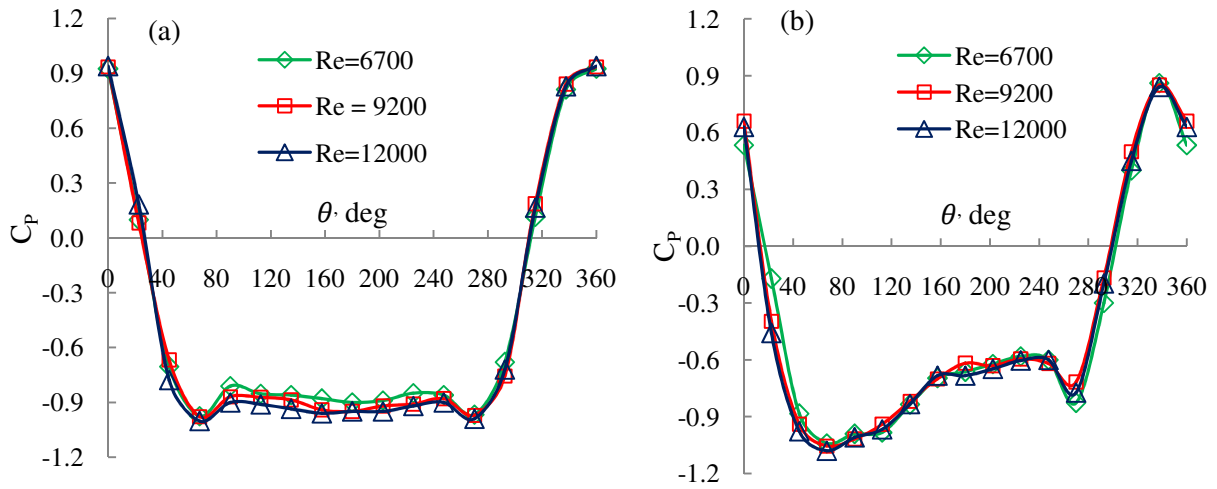


Fig. 70 Pressure distribution at $Tu = 4\%$, and $\Lambda/D = 1.28$ around (a) upstream cylinder, and (b) downstream cylinder.

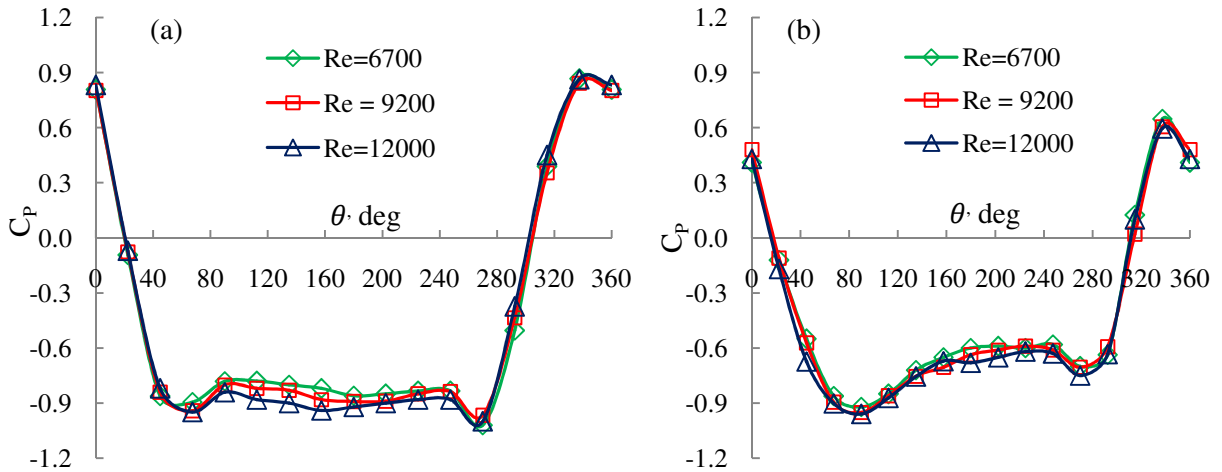


Fig. 71 Pressure distribution at $Tu = 7\%$, and $\Lambda/D = 1.28$ around (a) upstream cylinder, and (b) downstream cylinder.

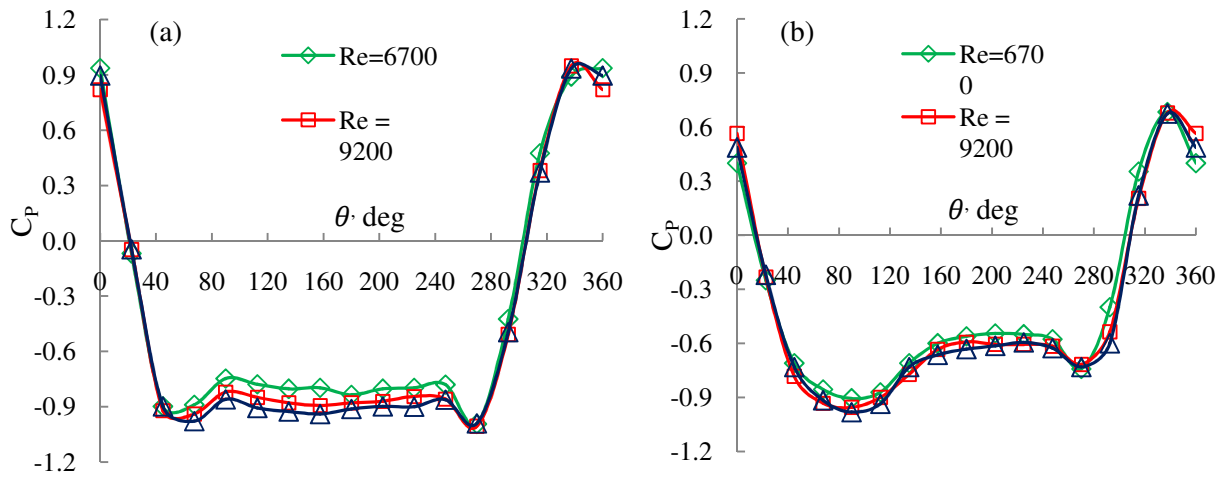


Fig.72 Pressure distribution at $Tu = 10\%$, and $\Lambda/D = 1.28$ around (a) upstream cylinder, and (b) downstream cylinder.

VITA AUCTORIS

NAME: Bita Motameni

PLACE OF BIRTH: Tehran, Iran

YEAR OF BIRTH: 1983

EDUCATION Adib Farzaneh High School, Tehran, Iran
1997-2001

Science and Research University, Tehran,
Iran
2001-2006 B.Sc.

University of Windsor, Windsor, Ontario,
Canada
2009-2011 M.Sc